

**The Role of Thermally Excited Vibrations in Gas-Surface  
Reactions: Methane on Ni(111) and Ir(111)**

A dissertation

submitted by

Deno F. Del Sesto

In partial fulfillment of the requirements  
for the degree of

Doctor of Philosophy

in

Chemistry

**TUFTS UNIVERSITY**

May 2011

The role of thermally excited vibrations in gas-surface  
reactions: Methane on Ni(111) and Ir(111)

By

Deno F. Del Sesto

Submitted to the Department of Chemistry on 18 April 2011 in partial fulfillment  
of the requirements for the degree of Doctor of Philosophy in Chemistry

*Abstract*

Eigenstate-resolved molecular beam experiments have been very effective at probing the dynamics of gas-surface reactions. This is especially true for methane reactions on nickel surfaces due to their importance in the field of heterogeneous catalysis, and their ability to be modeled theoretically. These experiments shed light on the process of breaking the C-H bond, and reveal how the partitioning of internal energy within the reactant gas can affect the overall probability of reaction. These results can then be used to predict reactivity of an ensemble of states, which is more applicable to industrial conditions.

In this thesis, we utilize this information to create a simple model to predict the relative contributions of each individual vibrational state present in a

thermal reactant gas. In a steam-reforming reactor, the methane is heated to high temperatures above a nickel catalyst. This heating creates reactants that are vibrationally hot, yet have little translational energy along the reaction coordinate. The simple model predicts that for a hot methane gas with little translational energy, vibrationally excited molecules dominate reactivity, while ground state molecules contribute little. As translational energy increases, vibrationally excited states become less important and the  $v=0$  vibrational ground state dominates reactivity simply because of its higher population.

An incident molecule can react during a single collision with the surface (a direct reaction), or it can first physically adsorb on the surface prior to reaction (a precursor-mediated reaction). The second part of this thesis addresses the role of vibrationally excited molecules on the precursor-mediated pathway. This pathway is studied on an Ir(111) surface. The lower activation barrier to reactivity, along with a high methane trapping probability at low translational energy allows for a measurable number of molecules to react via this pathway on this surface. Preliminary results indicate that thermally excited vibrations of methane gas can enhance reactivity of the trapping-mediated pathway, and they point to the potential importance of vibrationally hot precursors to the reactivity of thermal ensembles of reagents.

The described experiments were performed on a new molecular beam/UHV gas-surface scattering chamber constructed specifically for this study. The design, construction, and characterization of this apparatus can be found in Chapter 2 of this thesis.

## *Acknowledgements*

It is a difficult task to recount all the people who have helped you along the way when you spend 11 years of your life working towards a single goal. But the first one is easy. Since my second year here at Tufts, there has been one person who has been by my side and on my side without fail. She has been supportive of my journey, but more importantly she has endured hearing the phrase, "...just one more year..." over and over again. She stuck with me even though I know there were many times I didn't deserve it. She has provided me with a sense of completeness, and helped me build an amazing family that is the absolute center of my universe. So, thank you, Kimmie, for still being here at the end of what was easily the most difficult period of my life. I hope to make things better for us from here on out.

I need to thank the two people who were pretty much the only reason I even considered pursuing my Ph.D. in the first place: my parents, Madeleine and Joseph Del Sesto. I have doubted myself many times in my life, but my parents never doubted me, not even for a second. It was my father's unwavering belief that I was capable of handling anything life could throw at me that gave me the confidence to even try. It was my mother's examples of humility and modesty that prevented me from becoming arrogant or overconfident. My parents pushed my three brothers and me hard, and expected nothing but the best, but only because they knew we were capable of it. My parents never, ever, chastised us for failure, only for not doing everything in our power to succeed. Because of their love and dedication, and their willingness to go out of their way

and sacrifice to give us what we needed, they have created four confident, yet humble grown men. My only wish was that they could be here today to see me graduate, not just to see what I did, but to see what they did. As of the moment I complete my degree, all four of their sons will have received terminal degrees in their field: two Ph.D.'s, an M.B.A., and an M.F.A. A single paragraph could never express the gratitude and love you deserve, but thanks, Mom and Dad.

I also need to thank my three brothers, Gino, Rico, and Julio. I was very lucky to grow up with three brothers. However, our close quarters when we were younger meant that as we got older we tended to drift apart. Thankfully, we all seem to have noticed this and have made efforts to be bigger parts of each other's lives. I have always admired my brothers. Gino and Rico are extremely smart and driven, and have become incredibly successful because of it. Julio is very creative and talented, and I have always been jealous of his ability to see beauty in everything, and to express himself with such honesty. He has worked through a lot to get where he is now, and I'm happy that he was able to find a way to use his talents. The four of us have been through a rough time lately in losing our parents, but it just made us realize even more that we appreciate what our parents did for us, and for the people we have become.

There were many times in my career at Tufts when I was convinced it was time to throw in the towel and move on to something else. However, my adviser, Art Utz, always seemed to be able to convince me to stay. It means a lot to have someone of his skill and intelligence stand behind me time after time, and make me believe that I can contribute to this field. I am perpetually in awe of his intelligence and ability to teach. If I am able to go on and teach when I am

done here, I hope to be even a fraction as good as him. I made a lot of bad choices in grad school, but joining his research group was not one of them.

I would also like to thank my committee members, Profs. Jonathan Kenny and Elena Rybak-Akimova, along with my outside member Prof. Ricardo Metz, for taking the time serve as advisers and mentors in my time here at Tufts.

In my time here in the Utz group I have overlapped with many great students. First I must thank Ludo Juurlink for spending time explaining his poster to me at the departmental open house. His enthusiasm for the science and respect for his adviser convinced me that this was the group I wanted to join. I joined the group at the same time as another extraordinary student, Dan Killelea. We made a lot of memories in our first few years, whether it be commiserating over a recent Quantum Mechanics exam at PJ Ryan's, or determining how much Heineken and tartar sauce we could consume at the Burren. He was also my preferred companion for watching the Red Sox and Patriots, as his arrival in the Boston area precipitated unprecedented success for Boston sports. Except for the Bruins, of course. I am happy to hear of his new position at Loyola University, as he more than deserves it. I know he will be very successful, and will make important contributions to the field of physical chemistry.

I need to thank Rich Smith, who taught me most of what I know about this field. His ability to explain complicated material effortlessly is one of the reasons I was able to succeed in this group. Also, I would like to thank Irene Li and Christopher DiCesare, who also started at Tufts with me. Christopher and Irene are great friends and helped make the stress of graduate school tolerable. I can't imagine having to go through what we did without friend them like to help along the way.

There have been many members of the Utz Group who have helped over the years. Victoria Campbell has been a wonderful colleague for the past 8 years. She constantly amazes me as she sets her goals extremely high, and has the drive and intelligence to reach them over and over again. If I had a quarter of the motivation that she does, I would probably have managed to finish years ago. She has also been a great friend, and we have had lots of fun times over the years.

Chris Thomas joined the lab a few years ago, and had an immediate impact on getting the chamber ready for experiments. His ability to learn made him an important part of the project. I would like to thank the undergrads who have helped out on my chamber: Dan Cook, and Wallace Derricotte. Dan helped set up the chamber to do IR reflectivity experiments, and Wallace was integral in much of the data acquisition last summer. Eric Peterson and Eric Dombrowski will be taking over my machine once I graduate. I can think of no two people I would rather have succeed me. They both had the desire and dedication to quickly learn how to run experiments, and have been essential in taking the data I present in this thesis. I was lucky to have them arrive when they did, as I probably wouldn't be graduating today without them.

Lastly, I would like to thank those outside of my group who made grad school tolerable, I would mention you all by name, but this is already too long as it is. Please forgive me.

## Table of Contents

<i>Abstract</i> .....	<i>i</i>
<i>Acknowledgements</i> .....	<i>iii</i>
<i>Table of Contents</i> .....	<i>vii</i>
<i>List of Figures</i> .....	<i>ix</i>
<b>Chapter 1 Introduction</b> .....	<b>1</b>
<b>1.1 References</b> .....	<b>11</b>
<b>Chapter 2 Experimental Methods</b> .....	<b>14</b>
<b>2.1 Overview</b> .....	<b>14</b>
<b>2.2 Molecular Beam and Ultra-high Vacuum Chambers</b> .....	<b>15</b>
2.2.1 Differential Chambers.....	17
2.2.2 Nozzle Assembly, Beam Apertures.....	23
2.2.3 Ultra-high Vacuum (UHV) Chamber.....	27
<b>2.3 Chamber Procedures</b> .....	<b>32</b>
2.3.1 Interlock System.....	32
2.3.2 Sample Heating – PID.....	35
2.3.3 Cleaning Procedures.....	36
2.3.4 Beam Characterization.....	38
<b>2.4 Data Acquisition and Analysis</b> .....	<b>46</b>
2.4.1 King & Wells (K&W) Sticking Measurements.....	47
2.4.2 Auger Electron Spectroscopy (AES) Measurements.....	50
<b>2.5 References</b> .....	<b>52</b>
<b>Chapter 3 Contributions of Vibrationally Excited States to the Thermally Averaged Reactivity</b> .....	<b>55</b>
<b>3.1 Introduction</b> .....	<b>55</b>
3.1.1 Steam Reformers and Thermal Excitation.....	55

3.1.2	Eigenstate-resolved Measurements .....	56
<b>3.2</b>	<b>Molecular Beams – Methane on Nickel .....</b>	<b>59</b>
3.2.1	Functional Form of Sticking Curves .....	59
3.2.2	Reaction Curve as a Sum of States .....	61
3.2.3	Rotational and Vibrational Cooling in a Supersonic Expansion .....	66
<b>3.3</b>	<b>Obtaining an Estimate of <math>S_0^{v=0}</math> .....</b>	<b>68</b>
3.3.1	Methodology and Results .....	68
<b>3.4</b>	<b>Thermal Averaging over Vibrational States .....</b>	<b>71</b>
3.4.1	Methodology .....	71
3.4.2	Results and Discussion .....	74
<b>3.5</b>	<b>Conclusions and Future Applications of the Model .....</b>	<b>79</b>
<b>3.6</b>	<b>References .....</b>	<b>81</b>
<i>Chapter 4 Vibrational Enhancement of Reactivity in Precursor-Mediated</i>		
<i>Surface Reactions – Methane on Ir(111).....</i>		
		<b>85</b>
<b>4.1</b>	<b>Introduction.....</b>	<b>85</b>
<b>4.2</b>	<b>Reaction Mechanisms and Past Experiments.....</b>	<b>88</b>
4.2.1	Direct vs. Trapping-Mediated Mechanisms .....	88
4.2.2	Evidence for the Trapping-Mediated Reaction Pathway .....	91
4.2.3	Relevant Lifetimes .....	92
<b>4.3</b>	<b>Experimental Details .....</b>	<b>93</b>
<b>4.4</b>	<b>Results and Discussion .....</b>	<b>94</b>
<b>4.5</b>	<b>Conclusions and Future Goals.....</b>	<b>98</b>
<b>4.6</b>	<b>References .....</b>	<b>100</b>

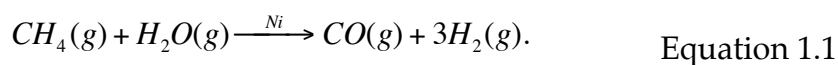
## *List of Figures*

Figure 1.1 – 1-D potential energy curve.....	3
Figure 1.2 - Reaction pathways for direct mechanism and precursor-mediated mechanism. ....	5
Figure 1.3 – 2-D potential energy surface.....	8
Figure 2.1 – Diagram of the gas-handling manifold.....	16
Figure 2.2 – Schematic diagram of the molecular beam and UHV chambers.....	18
Figure 2.3- Schematic of source flange ports.....	19
Figure 2.4 – Schematic showing aperture sizes on sliding beam valve. ....	22
Figure 2.5 - Technical drawing for the molecular beam nozzle. ....	24
Figure 2.6 – Nozzle assembly. ....	25
Figure 2.7 – Arrangement of UHV chamber instrumentation and components. .	28
Figure 2.8 – Schematic of the crystal mount.....	30
Figure 2.9 - Block diagram of computer controlled interlock.....	33
Figure 2.10 - Chopper wheel design.....	40
Figure 2.11 - Chopper gating function for TOF analysis.....	42
Figure 2.12 – Example of a pumping speed measurement.....	45
Figure 2.13 – Example of a King & Wells sticking probability measurement.....	48
Figure 2.14 – Example of an AES scan after a carbon dose.....	51
Figure 3.1 - Sticking curves for CH <sub>4</sub> on Ni(111), state-resolved and laser off. ....	60
Figure 3.2 - Effect of vibrational energy on position of the $v>0$ sticking curve. .	63
Figure 3.3 – <b>A</b> - individual s-curves for $v=0, 1,$ and $2$ of H <sub>2</sub> ; <b>B</b> - population weighted curves and sum over all states.....	65

Figure 3.4 – Relative vibrational state populations in methane as a function of nozzle temperature. ....	67
Figure 3.5 – Experimental data for $T_n < 450$ K and $T_n = 1050$ K on Ni(111).....	69
Figure 3.6 – Normalized vibrational energy populations for a 1050K nozzle .....	72
Figure 3.7 – Plots of the 1050 K curves for the three different version of the model, along with experimental 1050 K data. ....	75
Figure 3.8 – Model sticking probabilities for the ground state and first four polyads as a function of kinetic energy for the second model. ....	77
Figure 3.9 – Overlay of the 1-D kinetic energy distribution of methane at $T_n = 1050$ K and sticking curves. ....	78
Figure 4.1 – Vibrational and 1-D translational energy distributions of methane at a gas temperature of 1050 K. ....	86
Figure 4.2 – Reaction pathways for direct and trapping-mediated mechanism...	89
Figure 4.3 – Reaction probability of methane on Ir(111). ....	95
Figure 4.4 – Reaction probabilities for room temperature and 750K nozzle experiments. $T_s = 1000$ K. ....	97

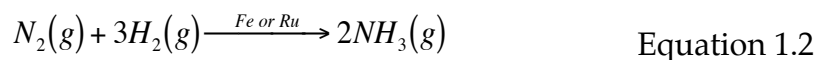
## Chapter 1 Introduction

The dynamics of methane dissociation on single crystal transition metal surfaces is worth investigating for its industrial importance, and because it is also a model system for studying heterogeneous catalysis. Methane is the major component of natural gas (~95%), and is used as a reactant in the steam reforming reaction,



However this reaction is highly activated, with the rate limiting step being the cleavage of the C-H bond. The barrier to reaction is about 100 kJ/mol [1-4], so very few of the molecules that strike the surface will react. Temperatures in excess of 1000 K are used to give the incident methane molecules more energy to react, and pressures above 20 atm increase the collision rate and maximize the number of reactions.

The hydrogen gas produced can then be used as fuel for modern fuel cells. However it is primarily used as a reactant in the Haber process (also known as the Haber-Bosch process), in which hydrogen gas reacts with nitrogen to produce ammonia.



This is an efficient pathway for production of ammonia, which is used in fertilizers. Before this process was discovered, synthesis of ammonia was very difficult due to the inherent stability of the nitrogen gas.

The dissociative chemisorption of methane, in which  $\text{CH}_4$  dissociates to form surface bound  $\text{CH}_3$  and H products, is the prototypical system for studying catalytic C-H bond activation [5]. Methane is the simplest hydrocarbon, and lends itself well to theory. The reagent's internal energy can also be strictly controlled within the confines of molecular beam experiments. The translational energy of methane can be tuned by changing the gas temperature, and the vibration and rotational energy can be controlled using laser excitation. The ability to look at the effect of different amounts and distributions of energy allows for detailed investigation into the dynamics of the gas-surface interaction and the potential energy surfaces associated with it. The importance of methane has led to many molecular beam studies of its interaction with various transition metal surfaces, especially nickel due to its industrial relevance [1, 4, 6-17].

The first step in understanding catalytic C-H bond cleavage is to look at the 1-D potential energy plot, shown in Figure 1.1. As methane approaches a metal surface, it experiences an electronic potential unique to that interaction. There is an activation barrier to reaction along the translational coordinate, along with chemisorption and physisorption wells. If the methane has enough translational energy to surmount this barrier, it will react on its first collision and fall into the chemisorption well, labeled **A**, in a "direct" reaction. Here the C-H bond is broken, leaving a methyl group and a hydrogen bound to the surface. If there is not enough energy to get over the barrier to react, the methane can either fall into a physisorption well, **B**, or simply scatter off of the repulsive potential and return to the gas phase. If the molecule traps in the physisorption well, it is weakly bound to the metal as an intact  $\text{CH}_4$ . From this well, it can either find a

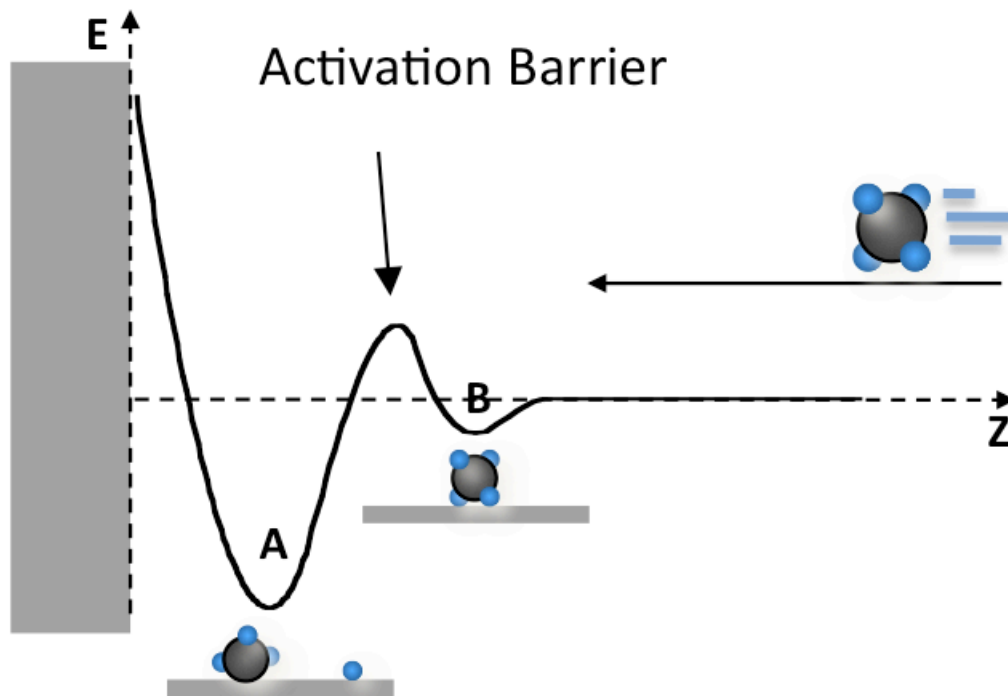


Figure 1.1 – 1-D potential energy curve for a molecule reacting on a metal surface. There are three potential outcomes for the reaction: the molecule chemisorbs on the surface, falling into potential well **A**; the molecule physisorbs, falling into potential well **B**; the molecule scatters from the surface and does not react.

pathway to chemisorption, or desorb from the surface and return to the gas phase without reacting. If the physisorbed molecule goes on to react, this is the precursor-mediated mechanism.

Therefore, there are two different mechanisms that can lead to a chemisorbed methane: direct and trapping, or precursor-mediated. These two mechanisms are depicted in Figure 1.2. In the direct mechanism, the methane will react in a single collision. In the precursor-mediated mechanism, the molecule must first physisorb to the surface before going on to react. The model presented in Chapter 3 involves the reactivity of methane on Ni(111), where the direct pathway dominates reactivity. The contribution to overall sticking of individual vibrational states is qualitatively discussed. One important thing to note in Figure 1.1 is that a 1-D picture does not tell the whole story on the gas-surface interaction. It describes the effect of a single degree of freedom – translation – while ignoring how other degrees of freedom may effect reactivity. When vibration of the C-H bond is included, a 2-D potential energy surface gives a slightly more detailed picture of the reaction.

Figure 1.3 shows two 2-D potential energy surfaces, where the y-axis is the distance of the methane from the surface, and the x-axis is the C-H bond distance. The solid lines are contour lines of equal potential, and the asterisks mark the saddle points. Figure 1.3A is an example of an “early” barrier, where the saddle point occurs in the entrance channel (before the elbow), and Figure 1.3B is an example of a “late” barrier, with the saddle point in the exit channel. Translational energy is more effective at surmounting the saddle point with an early barrier, as seen by the dashed line in panel A. If the saddle point were in the exit channel, the trajectory would approach a steep wall, and would not

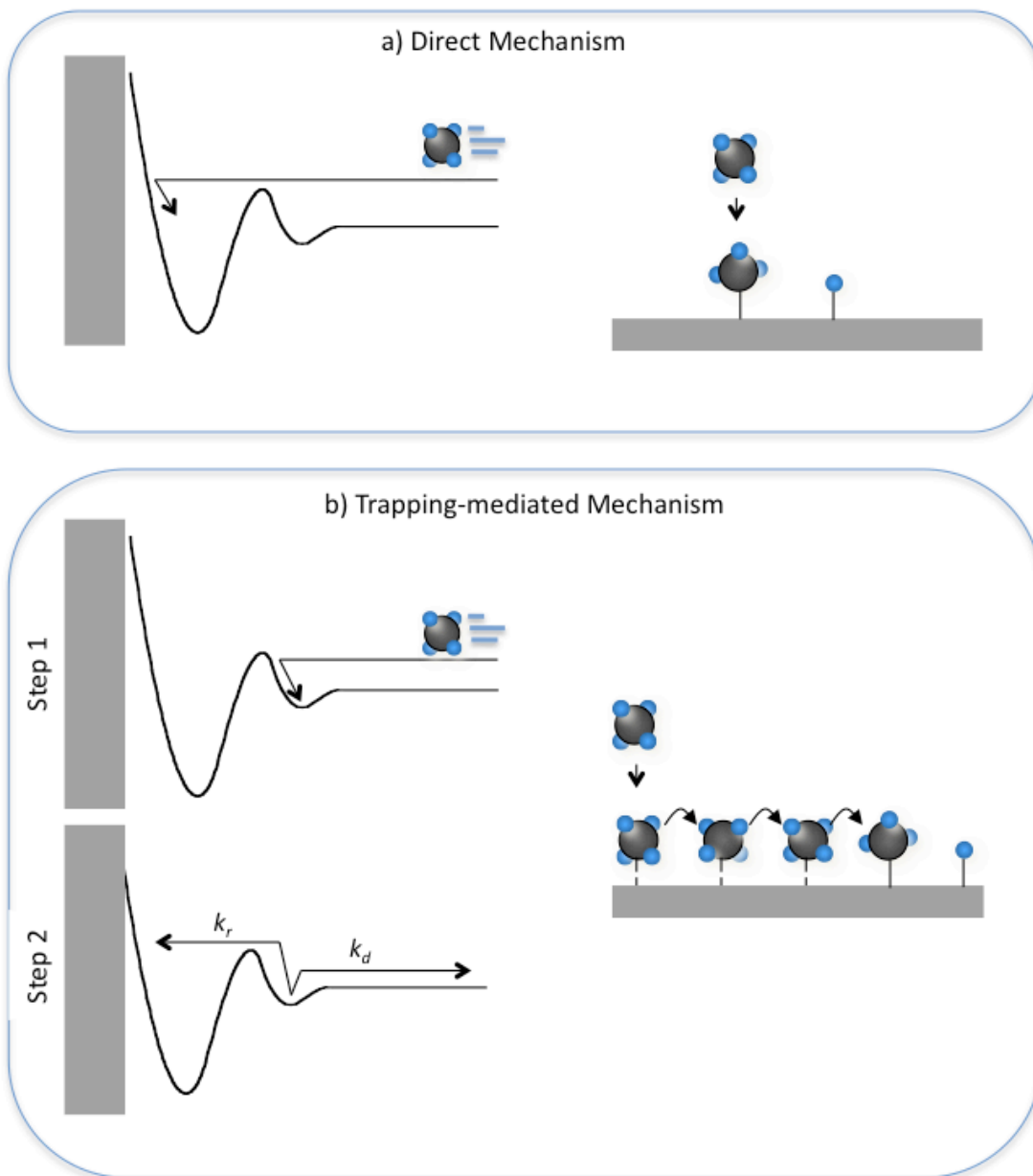


Figure 1.2 - Reaction pathways for a) direct mechanism and b) precursor-mediated mechanism.

couple well into the exit channel. In the trajectory seen in panel B, vibrational energy is more effective in promoting reactivity with a late barrier, since the vibrational motion of the bond couples well into the reaction coordinate. The 2-D picture gives more insight into the dynamics of the reaction and how vibrations may, in fact, be more effective.

Chapter 2 of this thesis describes the design, construction and characterization of a molecular beam apparatus designed to perform gas-surface reactions that probe the potential energy surface described. The experiments performed on this machine allow for the direct comparison of internal energy distributions in the methane-metal system.

In Chapter 3, the reactivity of thermal molecular beams are modeled, taking into account the effects of vibration on the effective barrier to reaction. This model explores the relative contributions of each vibrational state as a function of translational energy. In reactor conditions, the methane is heated to provide energy, but it may not be the translational energy added that speeds up the reaction. Even at 1000 K, a vast majority of the molecules have less than the required 80-100 kJ/mol of translational energy for reaction, but over 40% of the molecules will have one or more quanta of vibrational excitation that may enhance transition state access.

The model described in Chapter 3 suggests that vibrationally excited molecules account for most of the reactivity in a steam-reforming reactor. The internal energy of the vibrationally excited molecules provides energy for activation, and for a more effective route over the activation barrier. The vibrational motion of the methane promotes transition state access. In a thermal gas at high temperature there are a variety of vibrations excited, including bends,

stretches, and various combinations of these modes. The transition state of methane on nickel has been calculated to be significantly distorted from its gas-phase geometry [18-23]. The methane molecule needs to be distorted in a very specific way to approach the transition state geometry. The length of the dissociating C-H bond increases from 1.09 Å to 1.62 Å, and the angle increases from 109° to 138°. In eigenstate-resolved experiments only one mode of vibration is studied.

The experiments in Chapter 4 explore methane reactivity on Ir(111). Previous studies indicate that dissociation occurs via the direct mechanism at high translational energy, and via a precursor mediated mechanism at low translational energies. The reaction probability decreases with increasing translational energy until about 10 kJ/mol, and then begins increasing [24, 25]. The trapping probability of methane on Ir(111) is high at low translational energy even at high surface temperatures [26]. Also, the activation barrier on Ir(111) is much lower than that on nickel – only about 35-40 kJ/mol [25]. This leaves a significant number of molecules trapped on the surface (at low translational energies), that need to get over a relatively low barrier. In the context of Figure 1.2B, when the barrier to reaction is lowered, a larger fraction of molecules can react instead of desorb. It is useful to consider how a precursor-mediated pathway might enhance reactivity. The traditional picture is that when a cold gas impinges on a hot surface, energy exchange between the surface and adsorbate could activate reaction, but there is another way.

In the direct mechanism, a molecule coming in with the correct geometry will experience a lower translational energy threshold for reaction than a molecule that does not map well onto the transition state geometry. Since the

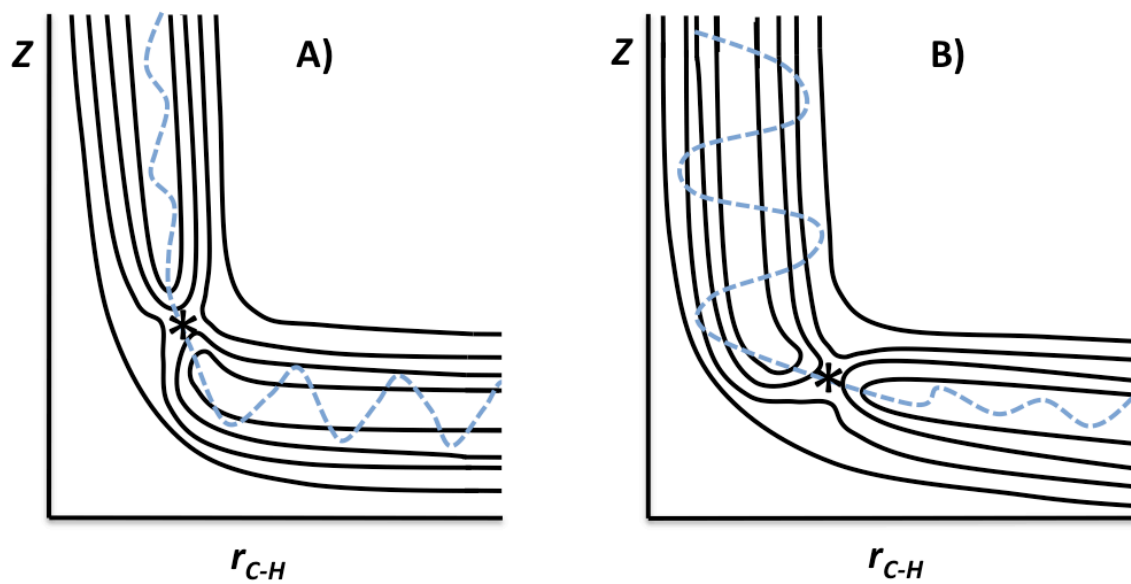


Figure 1.3 – 2-D potential energy surface showing how vibrational energy may promote reactivity. **A** “early barrier” potential; **B** “late barrier” potential.

time-scale of the direct interaction is so short, there is little time for significant reorientation of the methane reagent or diffusion to a more favorable surface site. In the precursor-mediated mechanism, the physisorbed molecule has a much longer interaction time with the surface, and has time to sample different orientations that better mimic the minimum energy transition state geometry and therefore react with higher probability.

One way to increase the number of possible orientations is to supply the molecule with internal energy, such as vibrations, that do not accommodate with the surface immediately upon physisorption, and distort the molecule in ways that may better approach the transition state. The lack of translational energy can now be compensated for by the rotation and vibration of the molecule on the surface. If the vibrational and physisorption lifetimes are long enough, the chance of reaction may increase. The molecule now has time to sample more of the potential, and the additional distortion due to vibrations may lead to a better mapping onto the transition state geometry. The data discussed in Chapter 4 reveal the effects of thermally excited vibrations on the reactivity of methane on Ir(111) in both the direct and precursor-mediated reaction channels. Due to the lower barrier to reaction on Ir(111) relative to Ni(111), high temperature gases have a modest percentage of molecules with enough vibrational energy to surmount the activation barrier and react. The data suggest that vibrational energy in methane incident on Ir(111) appears to enhance reactivity through the precursor mechanism more than it does for the direct pathway. A comparison is made between a room temperature gas and a gas heated to 750 K, where about 32% of the methane molecules are vibrationally excited.

Results from Chapters 3 and 4 show that thermally excited vibrations can play a very important role in methane activation. It is likely that vibrational energy in methane is what drives methane activation in reactor conditions. While there has been no experimental evidence of a trapping-mediated pathway on nickel, it is clear that the vibrationally excited molecules are dominating reactivity in the direct mechanism at low translational energies. The overall reactivity on nickel is orders of magnitude less than that on iridium, so it follows that there may be an uptick in reactivity for highly vibrationally excited molecules at low translational energies.

## 1.1 References

1. Holmblad, P.M., J. Wambach, and I. Chorkendorff, *Molecular-Beam Study of Dissociative Sticking of Methane on Ni(100)*. *Journal of Chemical Physics*, 1995. **102**(20): p. 8255-8263.
2. Lee, M.B., Q.Y. Yang, and S.T. Ceyer, *Dynamics of the Activated Dissociative Chemisorption of CH<sub>4</sub> and Implication for the Pressure Gap in Catalysis - A Molecular-Beam High-Resolution Electron-Energy Loss Study*. *Journal of Chemical Physics*, 1987. **87**(5): p. 2724-2741.
3. Chorkendorff, I. and J.W. Niemantsverdriet, *Concepts of modern catalysis and kinetics*. 2nd ed. 2007, Weinheim: Wiley-VCH.
4. Nielsen, B.O., et al., *Activated Dissociative Chemisorption of Methane on Ni(100) - A Direct Mechanism under Thermal Conditions*. *Catalysis Letters*, 1995. **32**(1-2): p. 15-30.
5. Larsen, J.H. and I. Chorkendorff, *From fundamental studies of reactivity on single crystals to the design of catalysts*. *Surface Science Reports*, 1999. **35**(5-8): p. 165-222.
6. Yates Jr., J.T., et al., *Search for vibrational activation in the chemisorption of methane*. *J. Chem. Phys.*, 1979. **70**(5): p. 2266-2272.
7. Winters, H.F., *The activated, dissociative chemisorption of methane on tungsten*. *J. Chem. Phys.*, 1975. **62**(6): p. 2454-2460.
8. Winters, H.F., *The kinetic isotope effect in the dissociative chemisorption of methane*. *J. Chem. Phys.*, 1976. **64**(9): p. 3495-3501.

9. Campbell, R.A., et al., *Methane activation on clean and oxidized Ni(100)*. Catal. Lett., 1993. **17**: p. 39-46.
10. Hamza, A.V. and R.J. Madix, *The Activation of Alkanes on Ni(100)*. Surface Sci., 1987. **179**: p. 25-46.
11. Hamza, A.V., H.P. Steinruck, and R.J. Madix, *The dynamics of dissociative adsorption of alkanes on Ir(110)*. J. Chem. Phys., 1987. **86**(11): p. 6506-6514.
12. Luntz, A.C. and H.F. Winters, *Dissociation of Methane and Ethane On Pt(110) - Evidence For a Direct Mechanism Under Thermal Conditions*. J. Chem. Phys., 1994. **101**(12): p. 10980-10989.
13. Harris, J., et al., *Thermally Assisted Tunneling: CH<sub>4</sub> Dissociation on Pt(111)*. Phys. Rev. Lett., 1991. **67**(5): p. 652-655.
14. Luntz, A.C. and D.S. Bethune, *Activation of methane dissociation on a Pt(111) surface*. J. Chem. Phys., 1989. **90**(2): p. 1274-1280.
15. Juurlink, L.B.F., D.R. Killelea, and A.L. Utz, *State-resolved probes of methane dissociation dynamics*. Progress in Surface Science, 2009. **84**(3-4): p. 69-134.
16. Utz, A.L., *Mode selective chemistry at surfaces*. Current Opinion in Solid State & Materials Science, 2009. **13**(1-2): p. 4-12.
17. Beck, R.D. and T.R. Rizzo, *Quantum state resolved studies of gas/surface reaction dynamics*. Chimia, 2004. **58**(5): p. 306-310.
18. Nave, S., A.K. Tiwari, and B. Jackson, *Methane dissociation and adsorption on Ni(111), Pt(111), Ni(100), Pt(100), and Pt(110)-(1x2): Energetic study*. Journal of Chemical Physics, 2010. **132**(5): p. 134702.
19. Henkelman, G., A. Arnaldsson, and H. Jonsson, *Theoretical calculations of CH<sub>4</sub> and H<sub>2</sub> associative desorption from Ni(111): Could subsurface hydrogen play an important role?* Journal of Chemical Physics, 2006. **124**(4): p. 044706.

20. Henkelman, G. and H. Jonsson, *Theoretical calculations of dissociative adsorption of CH<sub>4</sub> on an Ir(111) surface*. Physical Review Letters, 2001. **86**(4): p. 664-667.
21. Nave, S. and B. Jackson, *Vibrational mode-selective chemistry: Methane dissociation on Ni(100)*. Physical Review B, 2010. **81**(23): p. 173003.
22. Nave, S. and B. Jackson, *Methane dissociation on Ni(111) and Pt(111): Energetic and dynamical studies*. Journal of Chemical Physics, 2009. **130**(5): p. 054701.
23. Nave, S. and B. Jackson, *Methane dissociation on Ni(111): The effects of lattice motion and relaxation on reactivity*. Journal of Chemical Physics, 2007. **127**(22): p. 173003.
24. Reeves, C.T., D.C. Seets, and C.B. Mullins, *Low translational energy mechanisms in the dissociative chemisorption of methane on iridium and platinum surfaces*. Journal of Molecular Catalysis A: Chemical, 2001. **167**(1-2): p. 207-215.
25. Seets, D.C., et al., *Dissociative chemisorption of methane on Ir(111): Evidence for direct and trapping-mediated mechanisms*. J. Chem. Phys., 1997. **107**(23): p. 10229-10241.
26. Sitz, G.O. and C.B. Mullins, *Molecular dynamics simulations of the influence of surface temperature on the trapping of methane on iridium single-crystalline surfaces*. Journal of Physical Chemistry B, 2002. **106**(33): p. 8349-8353.

## Chapter 2 Experimental Methods

### 2.1 Overview

In order to perform the experiments described in Chapter 1, I designed and built a new molecular beam scattering chamber. This new chamber is the second in the laboratory, and allows for additional systems to be studied. This apparatus was modeled after the existing scattering system, but with several slight differences noted in section 2.2. The experiments described in Chapter 4 were all done on this new molecular beam apparatus.

The goal of the experiments described in Chapter 1 is to react methane molecules containing specific translational, vibrational and rotational energies on a clean, well-characterized single crystal Ir(111) surface. The molecular beam chamber is designed such that this level of control over the experiment can be achieved reproducibly. The methods and machine design for creating stable molecular beams have been well documented [1-10].

In the supersonic expansion, methane molecules thermally equilibrate with the walls of the nozzle before exiting the small orifice into the source chamber. Collisions with other methane molecules upon exiting allow for translational cooling, such that the molecules have a very narrow velocity distribution and small local speed of sound. This velocity is defined by Equation 2.1 [1],

$$V = \sqrt{\frac{2R}{W} \left( \frac{\gamma}{\gamma - 1} \right) T_0} \quad \text{Equation 2.1}$$

where  $W$  is the molar average molecular weight,  $R$  is the ideal gas constant, and  $\gamma = C_p/C_v$ . Therefore, the kinetic energy of the methane is defined by the

temperature of the nozzle, and the gas seeding of the methane (which changes  $W$ ), which can be finely controlled. The velocities can be verified through time-of-flight methods outlined below (section 2.3.4).

The section of the expansion containing these molecules, known as the “zone of silence”, is then selected out via a molecular beam skimmer and then further collimated by an aperture on the wall into the UHV chamber. What remains is a beam of non-interacting methane molecules with a very small kinetic energy distribution which is easily measured. Vibrational and rotational energy content can be controlled by excitation via an infrared laser that crosses the beam after it passes through the skimmer.

These methods allow for precise control over the energy and vibrational quantum state of the methane molecules and permit direct comparison of the reactivity of different normal modes of vibration with the ground vibrational state. These experiments provide key insight into the potential energy surface governing these gas-surface reactions.

## ***2.2 Molecular Beam and Ultra-high Vacuum Chambers***

The molecular beam line consists of three differentially pumped chambers known as the source, the first differential chamber (FDC), and the second differential chamber (SDC). The reactant gas is introduced through an orifice in the nozzle tube that is approximately 0.001” in diameter, and is collimated using a molecular beam skimmer [1]. The gas manifold used to supply the gas to the nozzle is shown in Figure 2.1. The beam is then further collimated and

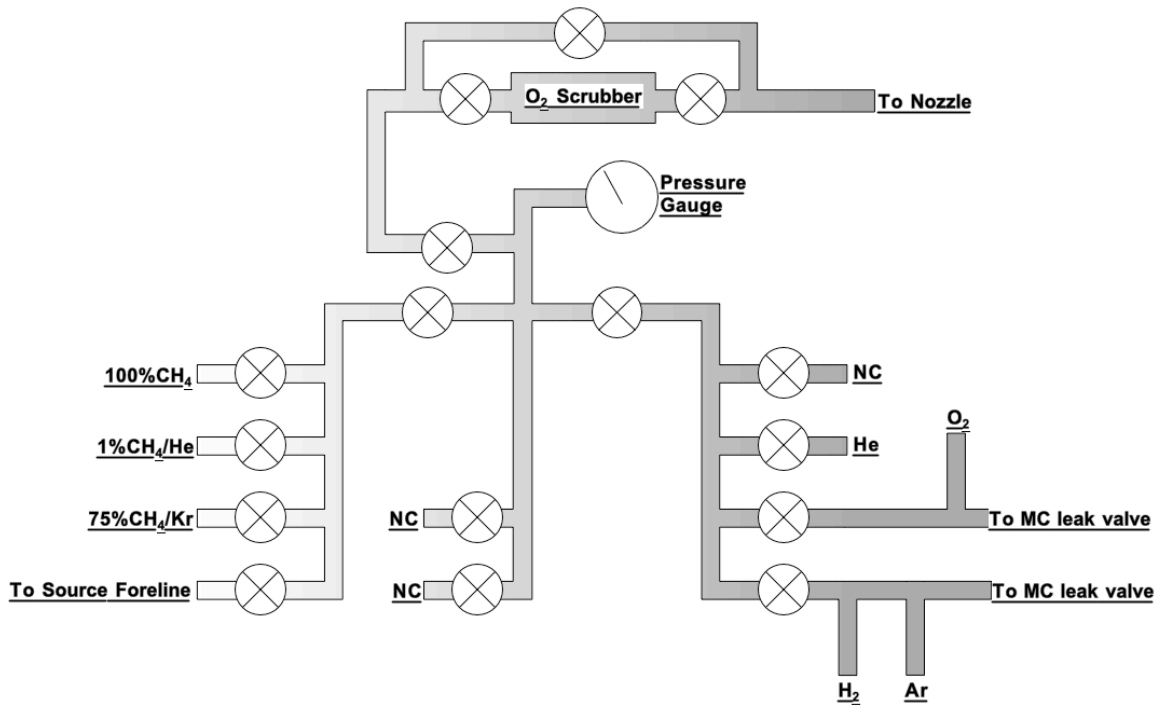


Figure 2.1 – Diagram of the gas-handling manifold located on the source chamber (most recent arrangement of tanks).

characterized as described in section 2.2.1. A schematic of the beam line can be found in Figure 2.2.

The overall design of the chamber is the same as the previous chamber [11-13], with a few key differences. The manipulator has a wider bore, and the main chamber is clear around the crystal so that a liquid helium cryostat may be added in the future to perform low temperature trapping experiments. Also, the source chamber is box shaped as opposed to the traditional cylinder/cone design. This allows for work to be performed on the nozzle assembly and manipulator without having to roll the chambers apart. Also in the source, an additional optical port has been added so laser excitation can be performed directly in front of the nozzle as well as in the first stage. The nozzle to sample distance was also reduced to maximize flux and reduce dose time. Finally, the nozzle design is based on the one used by Rettner and Auerbach [14]. The nozzle has an orifice bored into the side, and is mounted on an XYZ manipulator for external alignment.

### *2.2.1 Differential Chambers*

**Source:** The source chamber contains the main components necessary for creating a molecular beam: the nozzle, where the supersonic expansion takes place, and the skimmer, which is used to select out the desired section of the expansion. The source is pumped by a Varian VHS-10 diffusion pump topped with a water-cooled baffle (Varian F8600310) to prevent oil contamination in the vacuum chamber, and a 10" pneumatic gate valve (VRC). A mechanical pump (Varian CD700) and an in-line mechanical booster pump (Edwards EH250) back the pump. The high-throughput booster pump is turned on while a molecular

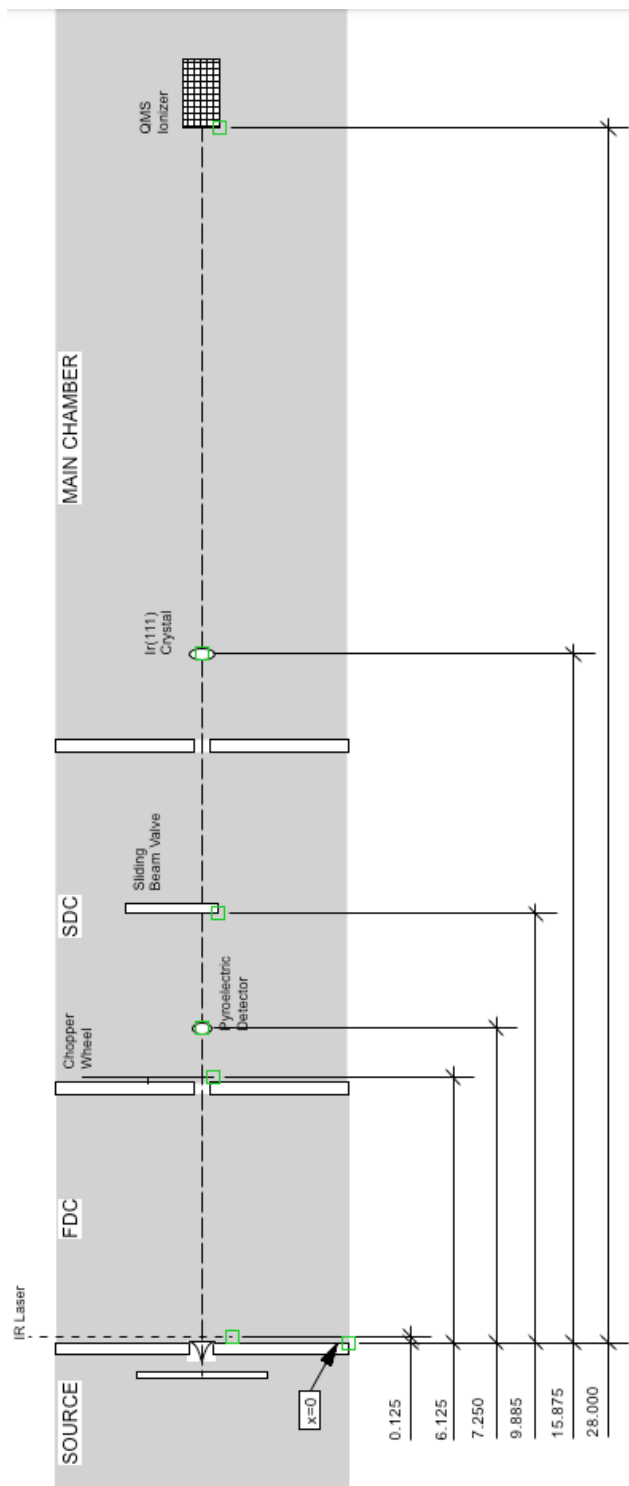


Figure 2.2 – Schematic diagram of the molecular beam and UHV chambers.

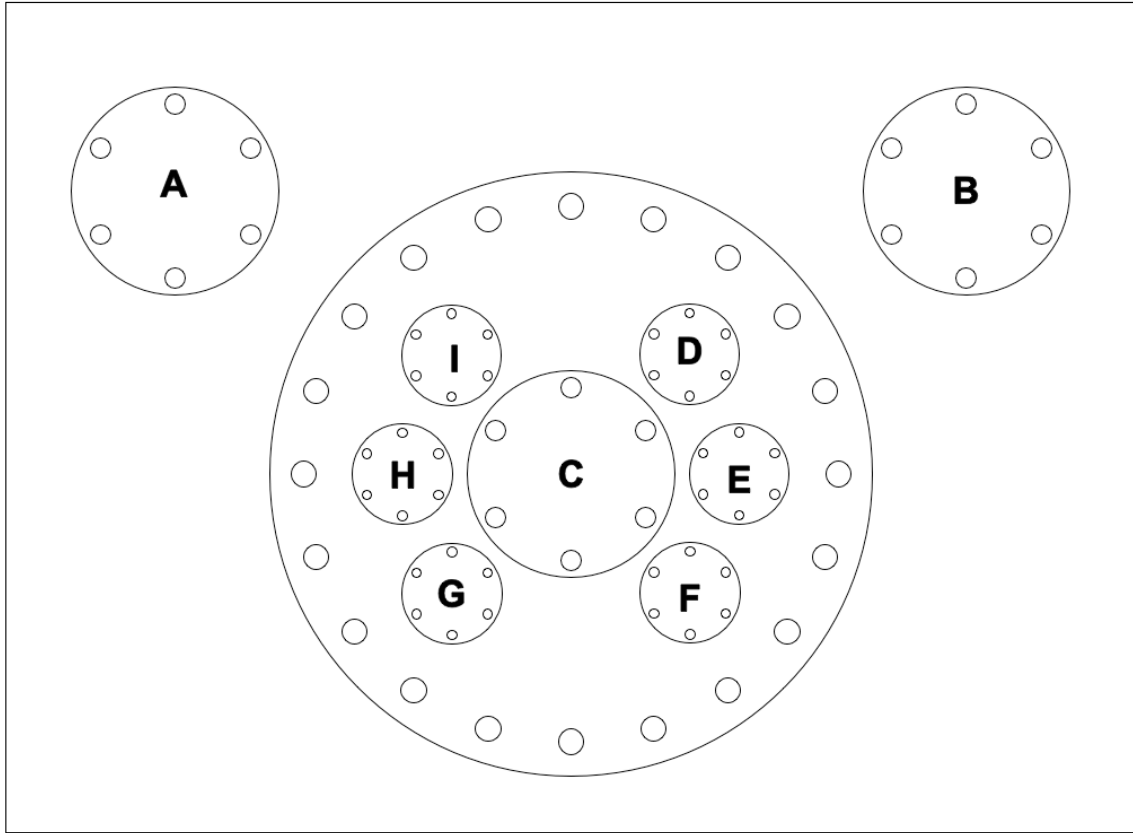


Figure 2.3- Schematic of source flange ports. **A** K-type thermocouple; **B** nozzle cooling lines; **C** pressure burst disk; **D** blank; **E** blank; **F** nozzle manipulator (Z); **G** nozzle manipulator (X-Y); **H** nozzle source line; **I** nozzle manipulator (X-Y).

beam is running in order to keep the foreline pressure of the diffusion pump at an acceptable level. This combination allows a base pressure (beam off) of about  $5 \times 10^{-8}$  torr, with a foreline pressure below 10 mtorr. While the beam is running the pressure is typically between  $5 \times 10^{-5}$  and  $2 \times 10^{-4}$  torr depending on the gases being pumped, with a foreline pressure ranging from 50 to 100 mtorr.

There is a pump down port located on the side of the source chamber with a manual angle valve (NorCal ESV1502). The flanges located on the back of the source chamber contain various feedthroughs necessary to creating the molecular beam. Figure 2.3 shows the various ports, including two 2.75" conflat flanges. The first contains two K-type thermocouple feedthroughs for monitoring the temperature of the nozzle at two different points: next to the orifice and near the o-ring seal. The second contains four feedthroughs for the 1/4" copper refrigeration tubing used to heat and cool the nozzle (see detailed nozzle assembly drawing in section 2.2.2). The 8" conflat flange, shown in Figure 2.3, contains six 1.33" conflat flanges and one 2.75" conflat flange. Four of the 1.33" flanges have 1/4" compression feedthroughs containing the nozzle manipulation controls (two orthogonal X-Y controls and a Z control), and the nozzle gas supply line. The 2.75" conflat on the multiport flange contains a pressure burst disk (MDC 420033) designed to protect other flanges and feedthroughs in the event the source becomes over-pressurized due to failure of the o-ring on the nozzle assembly. A 0.99 mm molecular beam skimmer (Beam Dynamics, Inc.) is mounted on the wall between the source and FDC.

**FDC:** The FDC is pumped by a Varian VHS-4 diffusion pump topped with a liquid nitrogen trap (Varian) and a manual gate valve (CVC 5017), and backed by a mechanical pump (Varian DS120) that it shares with the SDC. The FDC

contains a 0.5" IR sapphire window on a zero-length 2.75" conflat flange (MDC 9712002) that allows the IR laser to intersect the molecular beam at a right angle. A beam block (ThorLabs LB1) located opposite the window on the far side of the beam is used to reduce scattered IR light within the chamber and act as a heat sink. The FDC contains feedthrough flanges to accommodate 1/8" copper refrigeration tubing for cooling of the chopper motor located on the wall between the FDC and SDC, and an electrical feedthrough that supplies the power to the chopper motor. There is also a 2.75" conflat flange with two 1/4" compression feedthroughs that can be used to manipulate mirrors on an optical multipass cell should one be installed in the future.

**SDC:** The SDC is pumped by a Varian V250 turbomolecular pump topped by a 4" pneumatic gate valve, and backed by a mechanical pump shared with the FDC. Beam modulation, laser excitation detection, beam shuttering, and beam sizing all take place within the SDC. A three-phase AC motor (Globe Motors 75A1004-2) is mounted on the wall separating the FDC and SDC. The motor is mounted similar to the method used by Juurlink [12]. The only modification was the inclusion of a 1/8" layer of vibration dampening rubber between the face of the motor and the wall. The 3" chopper wheel (seen in detail in section 2.3.4) is mounted on the motor shaft in the SDC. On the same wall, an LED/photodiode position sensor is cemented at the edge of chopper wheel approximately 1/4 of a turn from the beam line. This chopper wheel and photodiode are used for modulation of the molecular beam for use in time-of-flight (TOF) measurements. A notch in the chopper wheel provides a start signal for the TOF. A gear is located on the face of the chopper wheel, and a linear feedthrough with a rack is

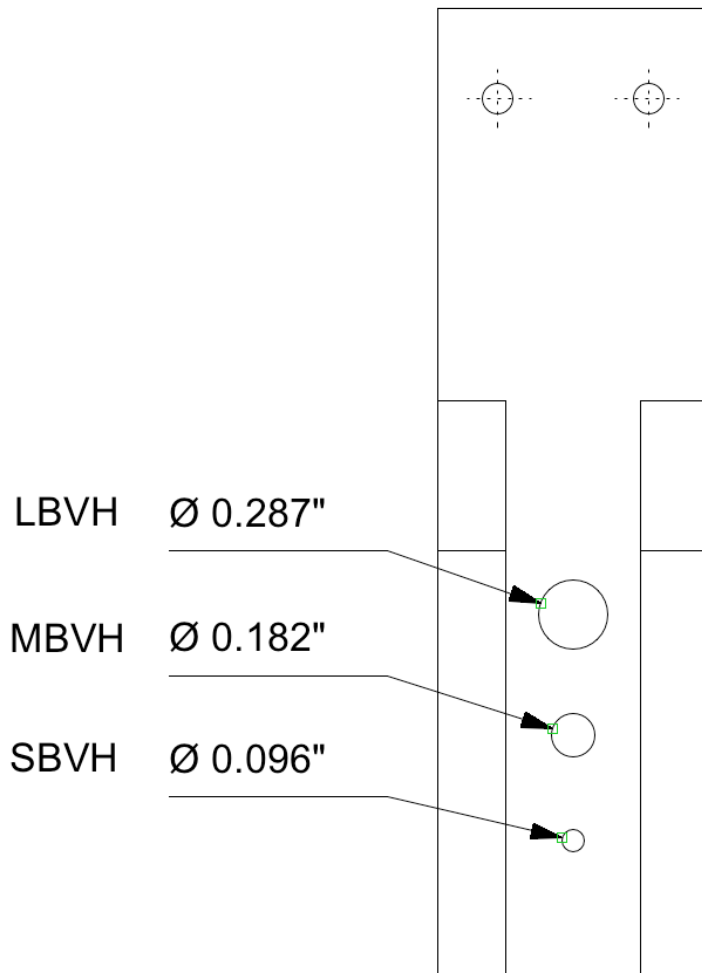


Figure 2.4 – Schematic showing aperture sizes on sliding beam valve. These apertures determine the diameter of the beam impinging on the crystal.

used to engage the gear and position the chopper wheel for CW beam doses, similar to the method employed by Juurlink [12].

Just downstream from the chopper wheel, a single element pyroelectric IR detector (Eltec 406-0) is placed into the beam via a linear motion feedthrough in the SDC. This can be used to detect IR laser absorption by molecules in the beam, and to quantify the fraction of methane molecules that are excited. An aperture-sizing sliding beam valve, shown in Figure 2.4 is located on the wall between the SDC and the main UHV chamber (MC). Translating this valve to the closed position isolates the main chamber from the SDC. Intermediate positions align apertures that define the molecular beam size at the metal surface. A 14 mm beam shutter (Vincent Associates VS14S1T0) is located between the IR detector and the sliding beam valve, and is used to control the length of time the beam enters the UHV chamber. The shutter is remotely controlled and timed for reproducible dose times.

### ***2.2.2 Nozzle Assembly, Beam Apertures***

The design of the nozzle mount was based on that used by Auerbach, et al. [14] The nozzle tube itself is 1/8" inconel stock with a 0.035" wall thickness, as shown in Figure 2.5. The tube has a flat milled on the side where the 0.001" orifice is laser-drilled. Unfortunately, the size of the orifice is difficult to measure, and nozzle size is generally determined by "poking" of the orifice with 0.0005" and 0.001" tungsten wire. The nozzle is also tested by forcing methanol through the orifice to verify a stream. Finally, the nozzle viability is confirmed by monitoring chamber pressures in the system while a molecular beam is running. With a usable nozzle, typical pressure are usually around  $5 \times 10^{-5}$  torr for

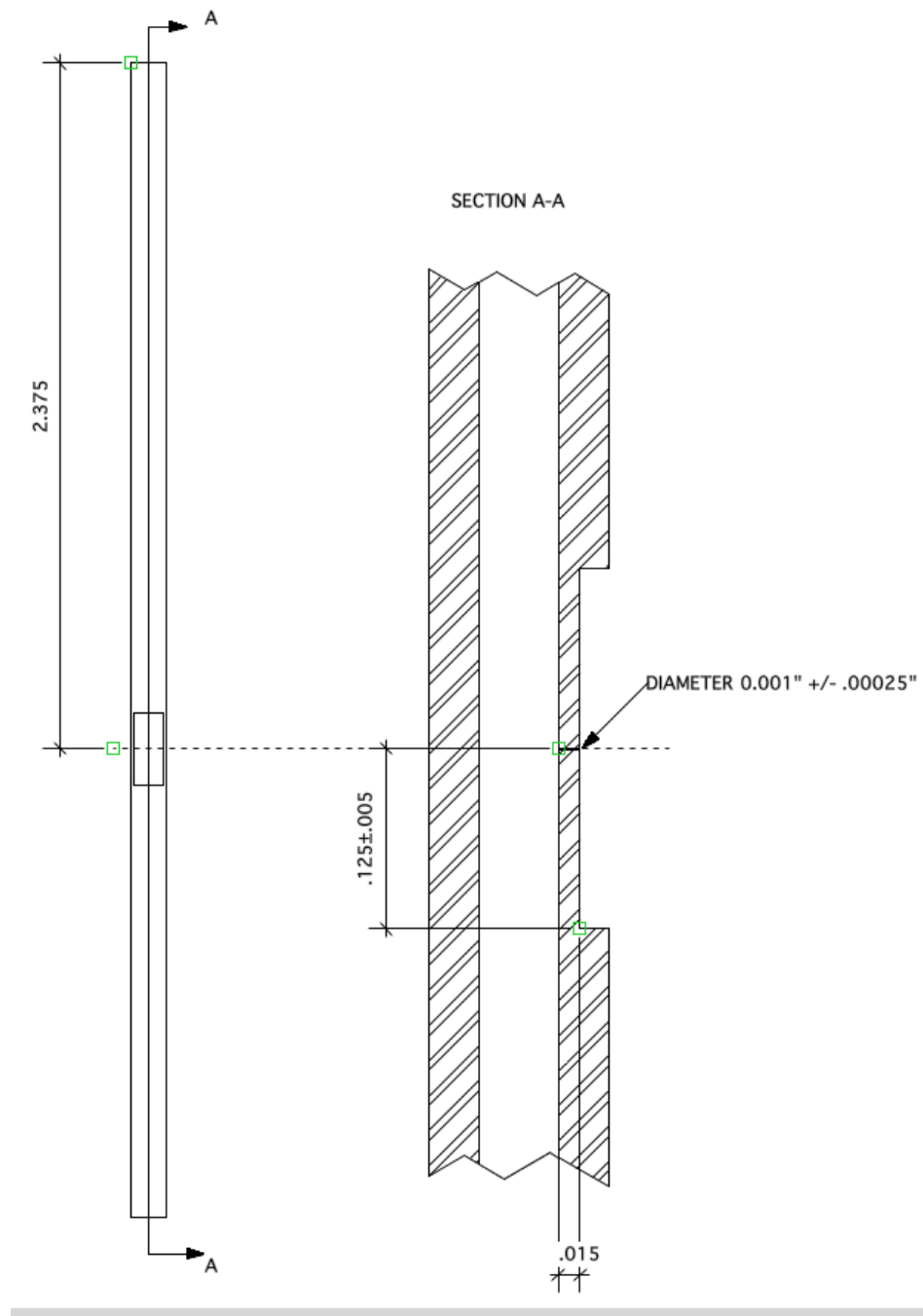


Figure 2.5 - Technical drawing for the fabrication of the inconel molecular beam nozzle.

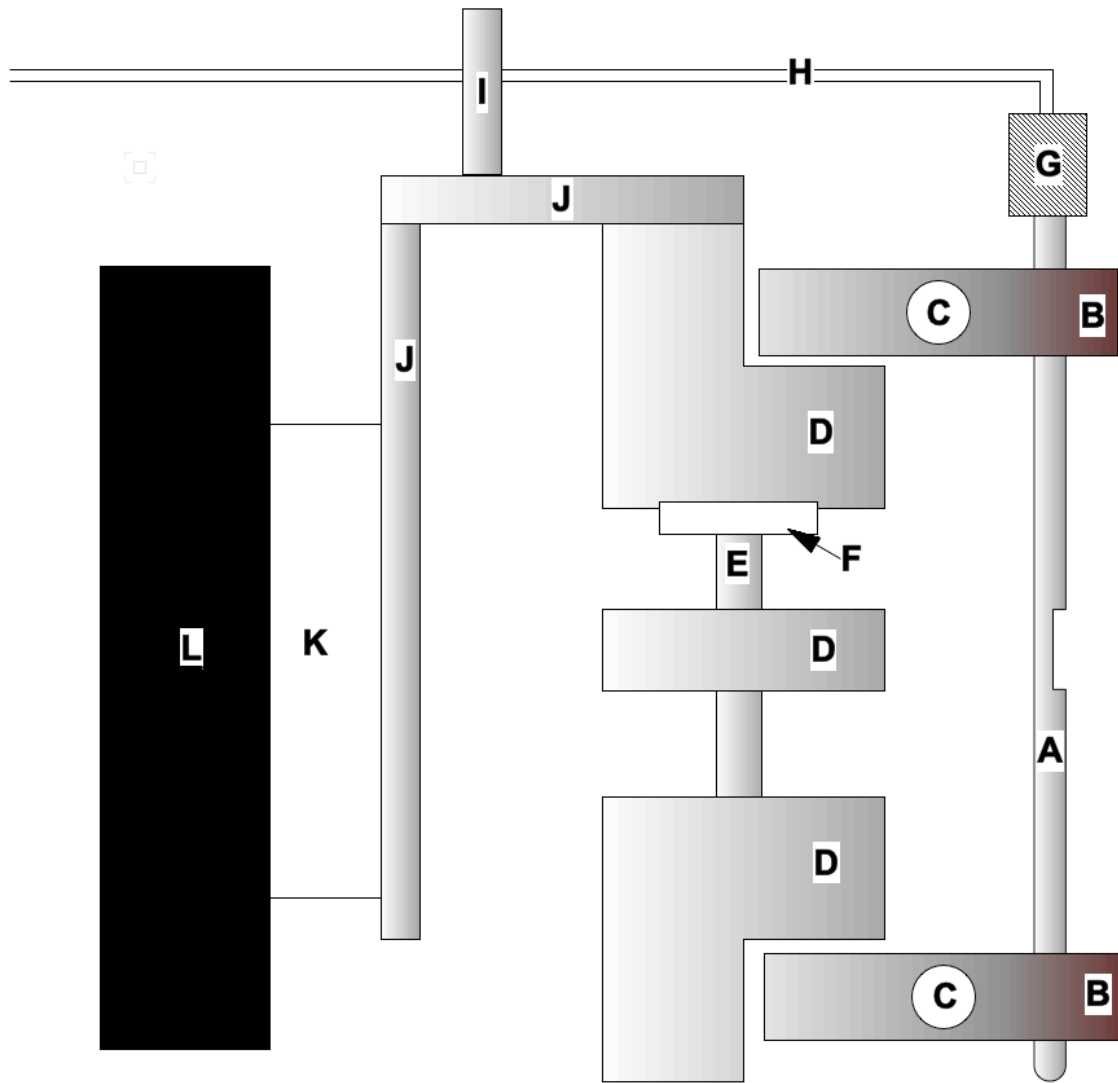


Figure 2.6 – Nozzle assembly. **A** inconel nozzle; **B** copper mounting and cooling blocks; **C** opening for 1/4" copper refrigeration tubing used for heating and cooling; **D** aluminum mounting blocks; **E** stainless steel rods; **F** ceramic bushings; **G** 1/8" compression fitting; **H** stainless gas line; **I** aluminum stabilizer for gas line; **J** aluminum mounting blocks; **K** ceramic spacer for electrical isolation; **L** X-Y stage.

the source,  $1 \times 10^{-6}$  torr for the FDC and SDC, and between  $1 \times 10^{-9}$  and  $1 \times 10^{-8}$  torr for the main chamber.

The nozzle mounting assembly can be seen in Figure 2.6. The nozzle is mounted onto two copper blocks each with a 1/4" copper cooling/heating tube passing through. These blocks are each mounted on a separate aluminum block. The top aluminum block has two 1/4" stainless steel rods press fit into the bottom. The bottom aluminum block has two linear bearings, allowing for movement of the block along the stainless rods to accommodate expansion and contraction of the nozzle while heating and cooling. This aluminum support assembly is mounted to an X-Y stage through a 1/2" ceramic spacer block for electrical isolation. The entire assembly is then mounted on a Z-stage, which controls the nozzle-skimmer distance. All three degrees of freedom are adjustable from outside the chamber via flexible couplings attached to stainless shafts that pass through compression fittings on the rear flange of the source (Figure 2.3).

When the molecular beam is running, it is collimated via the molecular beam skimmer on the source/FDC wall and the sliding beam valve on the SDC/main chamber wall. Alignment of the beam is done initially by ear immediately after installation. Before the beam line is pumped down, the nozzle is pressurized with approximately 40 psi of pure helium. When aligned, the beam passing through the skimmer causes an audible "rushing air" sound. In the past this has been found to be a very good estimate of a properly aligned nozzle. Once this sound is maximized, the beam line is pumped down and the molecular beam is allowed to pass into the main chamber. The QMS signal at  $m/z = 16$  is then maximized by manipulating the nozzle position using the external controls.

### *2.2.3 Ultra-high Vacuum (UHV) Chamber*

Ultra-high vacuum (UHV) chambers typically have base pressures below  $1 \times 10^{-10}$  torr [15, 16]. This is necessary because the experiments are inherently vulnerable to contamination. Very small amounts of carbon (1ML or  $\sim 10^{15}$  atoms/cm<sup>2</sup>) need to be detected on the surface, meaning that any carbon from other sources such as hydrocarbons (grease) and carbon oxides can influence results dramatically. Various techniques are used to achieve pressures this low. All components within the UHV chamber are solvent rinsed before being installed, and are handled with gloved hands only. Only materials with very low vapor pressures are used in the fabrication of all components to avoid long-term outgassing.

The UHV chamber, also known as the main chamber, is pumped by a Varian V250 turbomolecular pump topped with a pneumatic gate valve (NRC). A Varian V70 turbomolecular pump and an Alcatel 2033 back the V250. The second turbo pump backing the V250 was necessary because the compression ratio was too low to achieve UHV pressures when the foreline pressure was in the millitorr range. The cleaning process for the Ir crystal requires leaking in oxygen on a regular basis, and over time this oxygen begins to build up in the chamber by sticking to cold surfaces, especially the coldfinger. To resolve this problem, a titanium sublimation pump (Perkin Elmer Ultek) was added to the cross above the UTI QMS, separated from the rest of the chamber via a manual gate valve (Thermionics PFB-TLG-6.1). The Ti-Sub is flashed approximately once per week to keep the oxygen background pressure low. During flashing, the gate valve is closed most of the way (not sealed) to prevent any Ti from plating

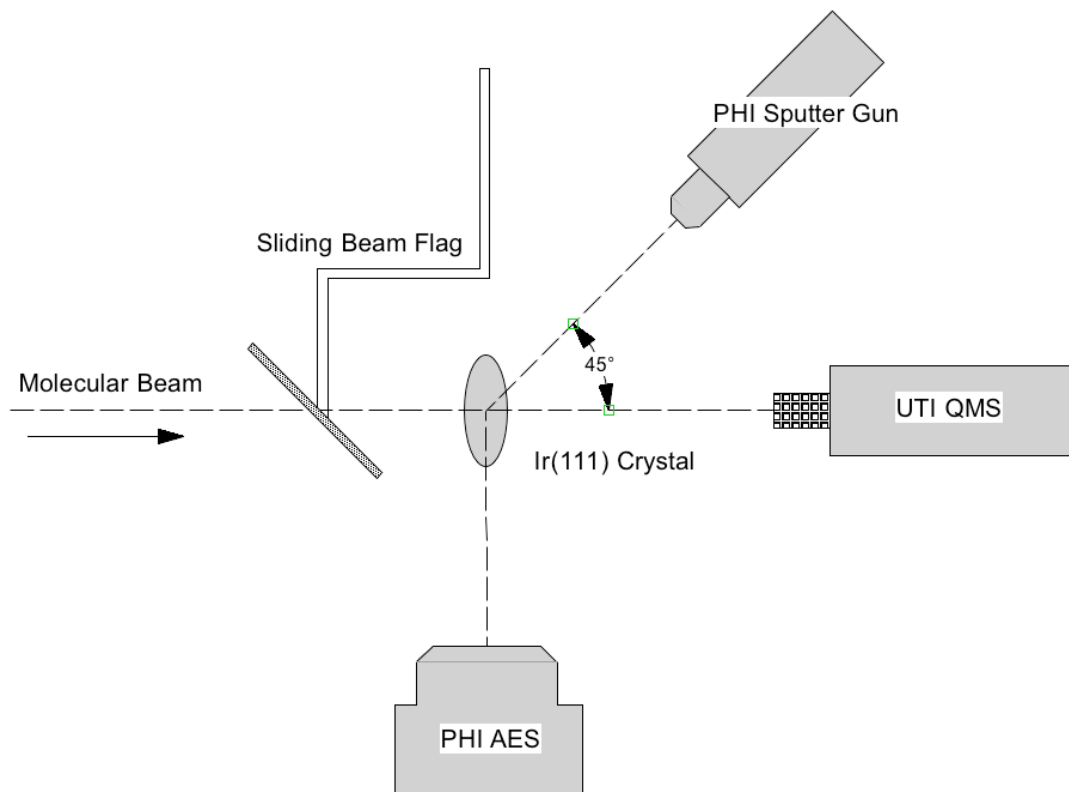


Figure 2.7 – Arrangement of UHV chamber instrumentation and components.

on the QMS. The entire chamber is baked above 140° Celsius via a series of heat tapes and bars attached to the outside of the chamber. This is done to remove excess water and contaminants and allow the base pressure to settle below  $1 \times 10^{-10}$  torr.

The UHV chamber contains a number of instruments essential to performing gas-surface experiments: a quadrupole mass spectrometer (QMS, UTI 100C), an ion sputter gun ( $\Phi$  04-191), and an auger electron spectrometer (AES,  $\Phi$  15-110). A schematic of the arrangement of these instruments can be found in Figure 2.7. The QMS is located in line with the beam, and is used for residual gas analysis (RGA), time-of-flight (TOF), temperature programmed desorption (TPD), and King & Wells (K&W) sticking measurements. The sputter gun is used for cleaning the sample surface (section 2.3.3), and the AES is used for determining surface cleanliness and total carbon coverage after each experiment (section 2.3.3).

There are two leak valves (Balzers UDV135) located on 2.75" conflat flanges in the UHV chamber. These are connected to the gas manifold mounted outside the source chamber. The first is used for leaking in argon for sputtering, and hydrogen for filament conditioning. The second is used for only oxygen during the crystal cleaning process. There is also a linear feedthrough with a stainless steel beam flag for blocking the beam during King & Wells experiments.

The one inch diameter coldfinger is mounted on a differentially pumped rotary stage with a 2.75" conflat port (McAllister DPRF 275), which is in turn mounted on an XYZ manipulator with  $\pm 1''$  of X and Y travel and 4" of Z travel. The rotary stage is mounted on top of the XYZ manipulator via a 4.5" conflat,

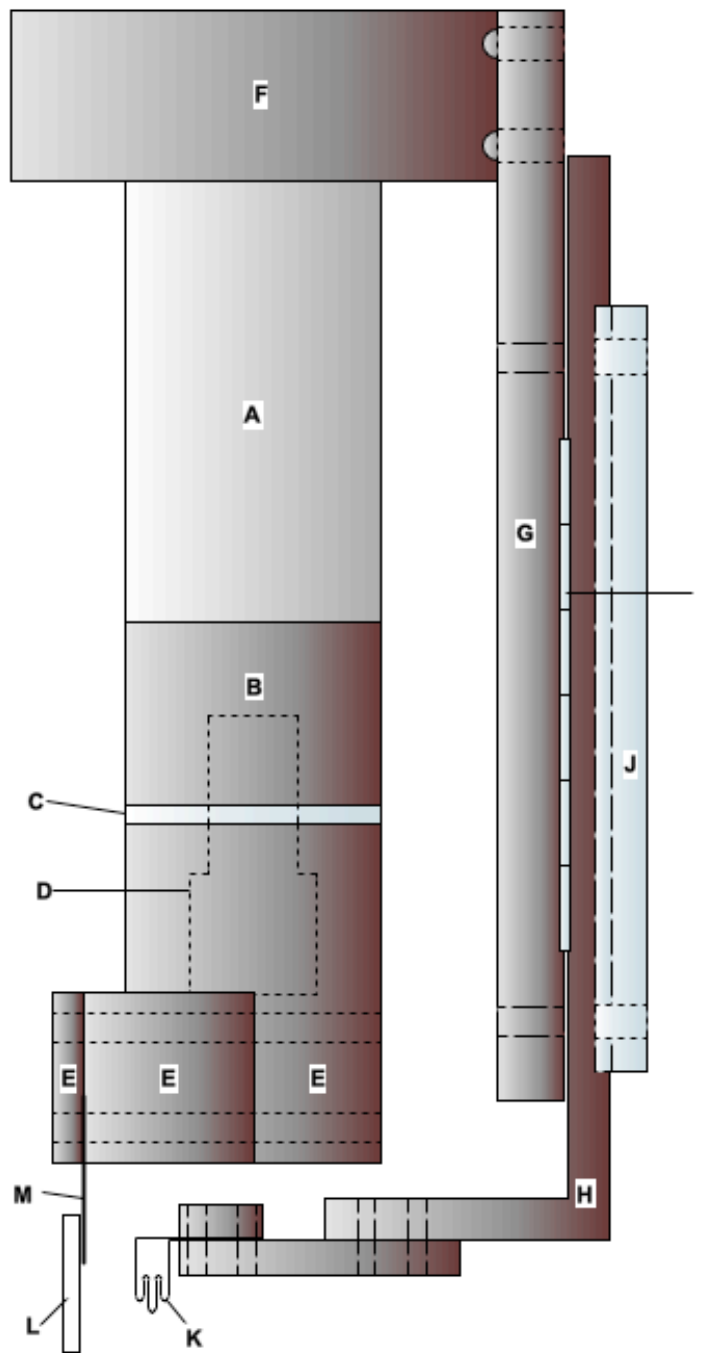


Figure 2.8 – Schematic of the crystal mount. **A** stainless steel coldfinger; **B** copper plug; **C** sapphire washer; **D** ¼"-20 copper screw; **E** copper mounting blocks; **F** copper mounting ring; **G** copper mounting plate for filament leads; **H** copper filament legs; **I** sapphire disks; **J** ceramic plate; **K** thoriated tungsten filament; **L** 1cm Ir(111) crystal; **M** tantalum support legs. An additional sapphire washer is placed between **D** and **E** to provide electrical isolation (not shown).

which is the typical point of removal for doing bench work on the crystal mount.

The stainless steel coldfinger extends 14" into the UHV chamber, so that the crystal rests in the beam line when at the middle of the Z-stroke, leaving plenty of room for fine-tuning. An OFHC plug has been brazed on the bottom of the coldfinger so that the cryogen (liquid nitrogen or dry ice) comes in direct contact with the copper. A ¼"-20 threaded hole is located on the bottom of the OFHC plug for attaching the crystal mount. Also, a 1.5" threaded ring has been brazed about 2" from the bottom of the coldfinger for mounting rear filament leads.

A schematic of the crystal mount can be found in Figure 2.8. The crystal itself has two thin strips of tantalum sheet spot welded horizontally across the back, extending about 2mm out on either side. The excess is then wrapped around and spot welded to 0.020" tantalum support legs that extend vertically from the crystal. These legs are then sandwiched between a copper plate and a 0.5" copper spacer, which are both connected to a copper support block. This support block is mounted to the brazed plug on the bottom of the coldfinger via a vented ¼"-20 screw. This screw is electrically isolated from the plug and the block by ½" and ¼" sapphire washers, respectively.

The rear filament is made of 0.010" thoriated tungsten wire that is electrochemically etched to approximately 0.008". It is attached to two L-shaped copper legs and is mounted about 0.10" behind the crystal. The copper legs are sandwiched between a ceramic plate and a copper plate, and electrically isolated from the copper plate by a series of sapphire disks. The copper plate is then

mounted on a copper block that is threaded on the brazed ring mentioned earlier.

## ***2.3 Chamber Procedures***

### ***2.3.1 Interlock System***

The molecular beam line and UHV chamber are monitored and controlled via a computer based interlock system. The system controls the opening and closing of gate valves and foreline valves, as well as switching the diffusion pump power on and off. A block diagram for the source chamber interlock appears in Figure 2.9. Sense signals from all components of the source chamber (foreline gauge, DP overtemp sensor, and DP water flow meter) output a low (ground) signal for GOOD, and an open signal for BAD (for fault). This signal is then connected to the sense circuit seen below. The switch is needed to select which signal is sent to the computer – the component sense signal or the bypass signal.

When the switch is in bypass position, the computer input is disconnected from the sense signal, and the circuit mimics a low, or GOOD, state. When this occurs, an orange LED is lit to indicate that that particular sense is in bypass mode, so the computer thinks it's GOOD. The LED is powered by the output of the 74HC04 (hex inverter), on which the input is tied to a +5 V pull-up resistor and the signal sent to the computer. When the switch is in bypass position, the input of the 74HC04 is pulled low, causing a "high" TTL output signal (~5 V), and conducting through the left LED on the diagram. When the switch is in sense position and the component is GOOD, current flows to the green LED (right). When the switch is in sense position and the component is BAD, the

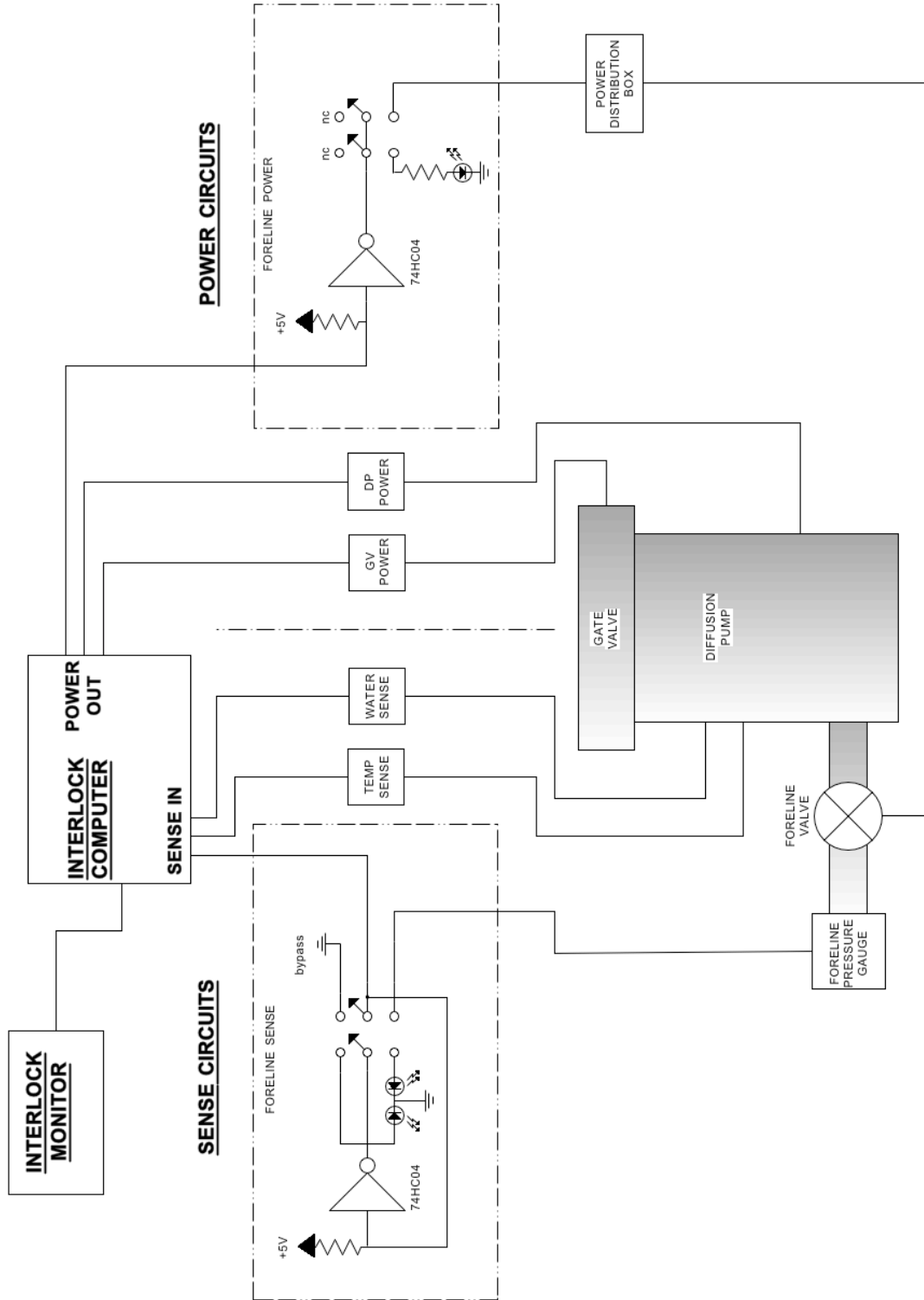


Figure 2.9 - Block diagram of computer controlled interlock (source chamber), including sense and power circuit diagrams.

input of the 74HC04 is pulled high, and no current conducts across either LED. The high TTL signal is also sent to the computer, which is recognized as bad.

The computer program, written in Visual Basic, is designed to read each input as a separate bit and determine whether its GOOD (low input, 0) or BAD (open/high input, 1). The code for the interlock program can be found in Appendix A. Based on the input bits, the program sets the output bits to either allow or disallow power switches to be activated.

The power circuits operate in a similar manner. The computer output to the interlock box is either low or open. When there is a fault (any one of the sense inputs is BAD), the output is open. The input of the 74HC04 is then pulled high through the pull-up resistor, and the output is low. When the switch is turned on, there is no (low) signal output. When the chamber is all GOOD, the input of the 74HC04 is pulled low, and the output is high. When the switch is turned on, a +5 VDC signal is output, and is used to switch relays in the various power distribution boxes – pneumatic gate valves (+12 VDC); foreline valves (+24 VDC); and diffusion pumps (110 V and 220 VAC).

The interlock program is designed to loop through status checks, and only act when something has been BAD for several cycles, thus eliminating any false shut downs due to brief electrical glitches. When there is a problem with the foreline pressure, the program continues to check the status, and will reopen the foreline if it once again reaches the GOOD state. With all other power (gate valves and diffusion pumps) the power remains off even if the chamber returns to the GOOD state. The interlock can on be manually reset by the external momentary pushbutton switch on the interlock box.

### *2.3.2 Sample Heating – PID*

The temperature of the crystal is monitored via a type-R thermocouple (Pt vs. Pt/13% Rh), which is spot welded directly to the back face just below the top. In the past both type-E and type-K thermocouples were used, but the high temperatures and oxygen atmosphere required for cleaning the crystal caused them to fail rather quickly. A wire is also connected to the front face of the crystal mounting block and fed out through a port near the top of the coldfinger that allows for direct electrical connection to the crystal for biasing while heating, and also for monitoring crystal current during sputtering and auger measurements.

The rear filament is used to heat the crystal, and is powered by a 0-6 VDC voltage supply (KEPCO ATE-6-10M). A crystal temperature of about 800 K can be reached by radiative heating alone (no crystal bias). With a 500 V positive bias (KEPCO BHK2000-0.1M) relative to the filament the crystal temperature can exceed 1600 K. For all experiments and cleaning procedures used it is necessary to bias the crystal.

The DC power supply has a 0-10 V programmable input that allows for remote control of the output voltage. This is connected to a proportion-integral-derivative (PID) controller, which has both a manual and automatic setting. The design was based on the design of Beckerle [17] and Smith [18]. When in manual mode, a trim pot is used to vary the PID output voltage from 0-10 V, accessing the full range of outputs from the DC filament supply. When in automatic mode, the PID compares the thermocouple voltage to a setpoint voltage set by an external power supply (HP 6216A), or a computer DAC input. The weighting of

the P, I, and D contributions are adjusted so that the setpoint temperature is reached and the voltage and current to the filament are stable.

### *2.3.3 Cleaning Procedures*

**UHV chamber:** The main chamber is cleaned after every vent. The primary contaminant is water, which can be removed by baking the chamber. Heat tapes and heater bars are arranged around the chamber to evenly heat all flanges and walls. Before starting the bakeout, all instrument cables are disconnected, along with the verniers on the manipulator, and additional silicone insulated heat tape is wrapped around the manipulator bellows. Thermocouples are taped to the chamber at various locations so that the temperature can be monitored during the bakeout. The crystal thermocouple also remains attached. The heat tapes are powered by four variacs that are connected to the chamber interlock. This ensures that the chamber does not continue to bake after a fault occurs and the main chamber gate valve is closed. The temperature is raised so that all thermocouples read above 140° C, and remains on until the pressure drops below  $3 \times 10^{-8}$  torr and levels out. At this point, all four main chamber filaments (rear, AES, sputter gun, QMS) are turned up to normal operating conditions for 1 hour to outgas. They are then treated (still hot) with  $1 \times 10^{-5}$  torr of hydrogen for an additional 45 minutes to remove any surface oxides. The filaments are then turned off, and once the chamber settles back to the pressure before outgassing the bakeout is turned off. The chamber typically requires 18-24 hours to cool down.

**Ir(111) crystal:** The methods for cleaning an Ir(111) surface are well documented [19, 20]. The first step towards an atomically clean surface is

sputtering [21]. A sputter gun is used to ionize argon atoms and accelerate them towards the Ir crystal at a 15 degree angle. The fast-moving, heavy argon atoms have enough energy to knock contaminants and iridium atoms into the gas phase, thus removing them from the surface [21]. Argon is leaked into the chamber at a pressure of  $5 \times 10^{-5}$  torr, with a sputter gun filament emission of approximately 20 mA and 1.5 kV. An initial crystal current of about 3  $\mu$ A is measured via a picoammeter connected to the crystal bias wire, but this current slowly decreases over sputtering time. This process is performed for about 5 minutes at the beginning of each day to remove any subsurface contaminants that migrate to the surface over time, such as carbon, oxygen, and calcium [22, 23]. If the crystal is removed and replaced it is often necessary to initially sputter for longer times.

Once sputtering is complete, the crystal is annealed to 1300 K for 45 minutes. The surface of the crystal is significantly roughened during sputtering, and annealing helps the (111) surface to recover quickly. AES is then used to check for surface cleanliness. Trace amounts of carbon and oxygen are typically the only contaminants remaining. Removal of trace carbon contamination is achieved through oxidation. The crystal is heated to 1100 K in the presence of  $1 \times 10^{-7}$  torr of O<sub>2</sub> for 5-10 minutes (30 – 60 L). Once the oxygen is turned off, the crystal is briefly flashed above 1500 K (~1 minute) to remove any remaining oxygen chemically bound to the surface. When these steps are complete the crystal is checked for cleanliness via AES, and typically shows no contamination.

The product of methane molecular beam experiments is surface-bound carbon which does not dissolve into the bulk of the Ir crystal upon heating [20], so the oxidation/flash steps need to be repeated after each dose.

### 2.3.4 Beam Characterization

**Time-of-flight:** The translational energies of the molecular beams used in these experiments can be calculated directly from the velocity of the molecules. The method used to determine these velocities is called time-of-flight mass spectrometry (TOF). In this method, a chopper wheel is used to chop the molecular beam into well-defined pulses, which are then detected by the in-line quadrupole mass spectrometer connected to a computer. An LED photodiode is used to send a start pulse to tell the computer to start recording the QMS signal. The velocity can be calculated from the time it takes for the pulse to travel from the chopper wheel to the QMS, and the total distance it travels;  $v=d/t$ . The computer records the QMS signal in 2  $\mu\text{s}$  intervals after receiving the start trigger from the LED sensor.

The gating function is used to make a weighted fitting function for the TOF analysis, and can be defined as the time dependent overlap of a rectangle (chopper slot) passing through a circle (beam). Figure 2.10 shows the schematic of the chopper wheel including the chopping/trigger slot. The opening time for the gating function is defined by the time it takes the rectangular chopper slot to fully overlap the circular molecular beam. At a speed of 200 Hz, with a chopper wheel radius of 3.175 cm at the beam center, and a slot width of 0.1524 cm, the opening time for the gating function is 38.2  $\mu\text{s}$ . The functional form of the gating function is defined by Equation 2.2.

$$2 \times \int_0^{2R} \sqrt{(2xR - x^2)} dx \quad \text{Equation 2.2}$$

In this function  $R$  is defined as the radius of the molecular beam, and  $x$  is the position of the rectangular chopping slit with width  $2R$ . The full gating function for the opening and closing of the chopper is shown in Figure 2.11. As mentioned previously, the computer measures QMS counts in  $2 \mu\text{s}$  intervals after the trigger pulse is received. The velocity of the molecules arriving during this time is assumed to have an approximate Maxwell-Boltzmann distribution about the center of the interval. The signal response of the QMS should be in the form of Equation 2.3 [24],

$$g_{density}(t) \sim \frac{g(t)}{v} \sim \left(\frac{L}{t}\right)^4 \times \left[ -\frac{\left(\left(\frac{L}{t}\right) - \left(\frac{L}{t_0}\right)\right)^2}{\alpha} \right], \quad \text{Equation 2.3}$$

where  $v$  is the velocity,  $L$  is the flight path length,  $t$  is the time,  $t_0$  is the stream flight time, and  $\alpha$  is the peak width. Therefore, we can model the recorded pulse as the sum of these distributions as a function of time. This sum will be then weighted using the time dependent gating function defining the relative amplitudes.

There are several delays associated with the time-of-flight measurements that need to be accounted for during the analysis. These delays include a chopper offset delay, an LED sensor offset delay, a pre-trigger delay, and the ion flight time. The chopper offset delay accounts for the trigger/beam line geometry. Figure 2.10 shows the geometry of the beam line and LED sensor with the chopper wheel overlay. When the wheel is spinning clockwise, the slot that triggers the LED also chops the molecular beam. This quarter turn adds 1.25 ms

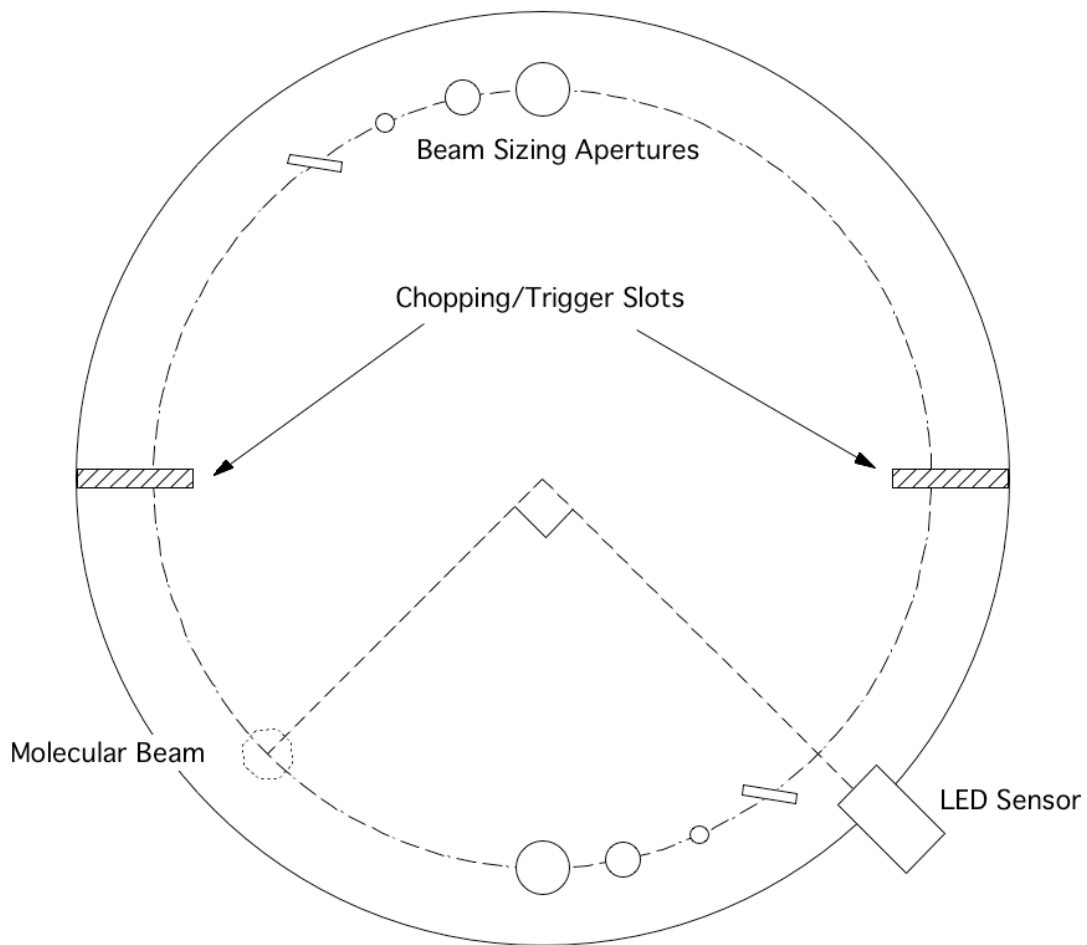


Figure 2.10 - Chopper wheel design indicating positions of the chopping/trigger slots and the beam sizing apertures (actual chamber orientation).

to the peak arrival time at 200 Hz, which must be subtracted from the measured arrival time.

The LED sensor is approximately one quarter of a turn before the beam line, but not exactly. TOFs taken with the chopper wheel spinning in opposite directions are not superimposable, which means the angle between the LED sensor and the beam line is not exactly 90 degrees. Taking half of the offset between the two peaks gives us a correction of about 19  $\mu\text{s}$  to the chopper offset delay discussed above. This correction must be added to the measured arrival times, since the observed offset causes the peaks to arrive earlier than expected when rotating in the clockwise direction.

The peak of the gating function corresponds to the center of the chopper slot. However, the computer is triggered by the leading edge of the slot. Therefore, the counting begins half a slot width too early, called the pre-trigger delay. The slot diameter is 0.030", which corresponds to a time delay of 19.1  $\mu\text{s}$  and needs to be added to the stream flight time.

We are only interested in the neutral flight time of the species of interest when measuring time-of-flights. However, part of the molecule's journey is spent as an ion. This needs to be subtracted out of the arrival time of the molecule, since only the neutral flight time is of interest. In order to determine the ion flight times for different species, it is necessary first to determine the ion flight length in the UTI. This is done by running a room temperature argon expansion. Argon cracks in the ionizer into two major fragments, with mass-to-charge ratios of 40 ( $\text{Ar}^+$ ) and 20 ( $\text{Ar}^{2+}$ ), and relative peak intensities of 100 and 16,

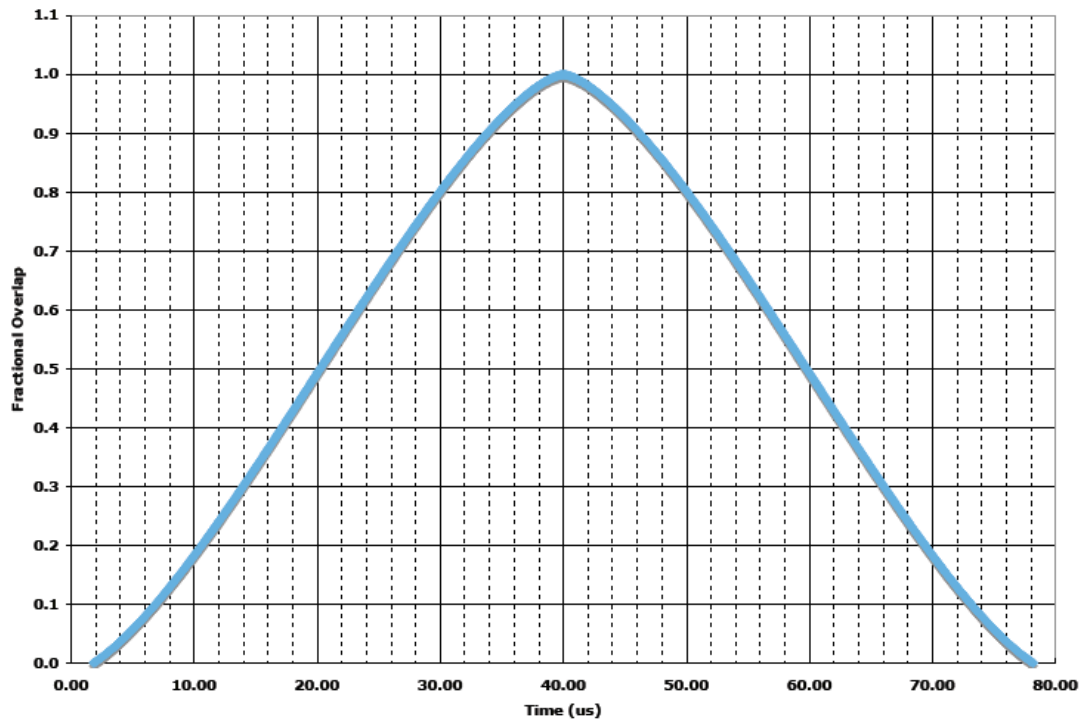


Figure 2.11 - Chopper gating function for TOF analysis. Peak is centered on 40.0  $\mu\text{s}$  and the dashed lines represent the 2  $\mu\text{s}$  intervals used for fitting

respectively. The ion flight time is dependent on the mass of the species, and is given by Equation 2.4,

$$t_{ion} = \frac{L_{ion}}{v_{ion}} = \frac{L_{ion}}{\sqrt{\frac{(2 \times E_{ion})}{m_{ion}}}} \quad \text{Equation 2.4}$$

where  $L_{ion}$  is the flight length for the ion,  $v_{ion}$  is the ion velocity,  $E_{ion}$  is the ion energy, and  $m_{ion}$  is its mass. For the argon beam, the neutral flight time for the two fragments in the UTI are the same. Therefore, the difference in arrival times of the ions is due solely to the difference the ion flight times. Equation 2.4 can then be rearranged.

$$\Delta t_{meas} = \Delta t_{ion} = L_{ion} \times \frac{\sqrt{m_{ion1}} - \sqrt{m_{ion2}}}{\sqrt{2 \times E_{ion}}} \quad \text{Equation 2.5}$$

**Flux measurements:** The flux of methane into the main chamber is defined as the number of methane molecules that impinge on a given area of the crystal per unit time. In order to calculate this, the partial pressure of methane during a dose, the chamber volume, the pumping speed, and the beam spot size must first be determined.

For pure methane beams, the partial pressure of methane is simply the ion gauge pressure, which can be read directly during a dose. For dilute beams, however, the main chamber pressure is the sum of the methane and seed gas partial pressures. To determine the partial pressure of the methane, the QMS is used to measure the signal from  $m/z = 16$  while the beam is running. The shutter is then closed, and pure methane is leaked into the chamber until the QMS signal

returns to the same value as when the beam was running. The QMS filament is then turned off, and the main chamber pressure recorded giving the partial pressure of methane only.

The volume of the chamber can then be determined by adding an additional ballast chamber of a known volume to the UHV valve. A stainless steel tube was added to the chamber, and both chambers were roughed down to below mtorr level. A short length (approximately 3") of copper refrigeration tubing was connected to the added tube chamber and sealed off with one atmosphere of air contained within. A valve between the copper tubing and the added tube is then opened, and the pressure within both chambers is measured using a baratron. Since the initial and final pressures of both chambers are known, and the volume of the copper tubing can be easily determined, the volume of the added tube chamber (including valve and baratron volumes) can be calculated, and was found to be about 1.3 L.

The two added chambers are then vented to atmosphere, and the copper refrigeration tubing is removed. The outer chamber was then sealed, and the UHV valve opened to expand the gas into the main chamber. The final pressure was then recorded. Using ideal gas law, the volume of the UHV chamber was calculated to be approximately 61 L.

Once the chamber volume is known, the pumping speed can be calculated. The QMS is set to measure  $m/z = 16$  while the beam is running, and the signal is recorded as the shutter is closed. It is necessary to do this experiment with the crystal at room temperature and both the coldfinger and cryotrap empty to avoid additional pumping. The signal can then be fit as a single exponential decay, and the pumping speed calculated from the lifetime of

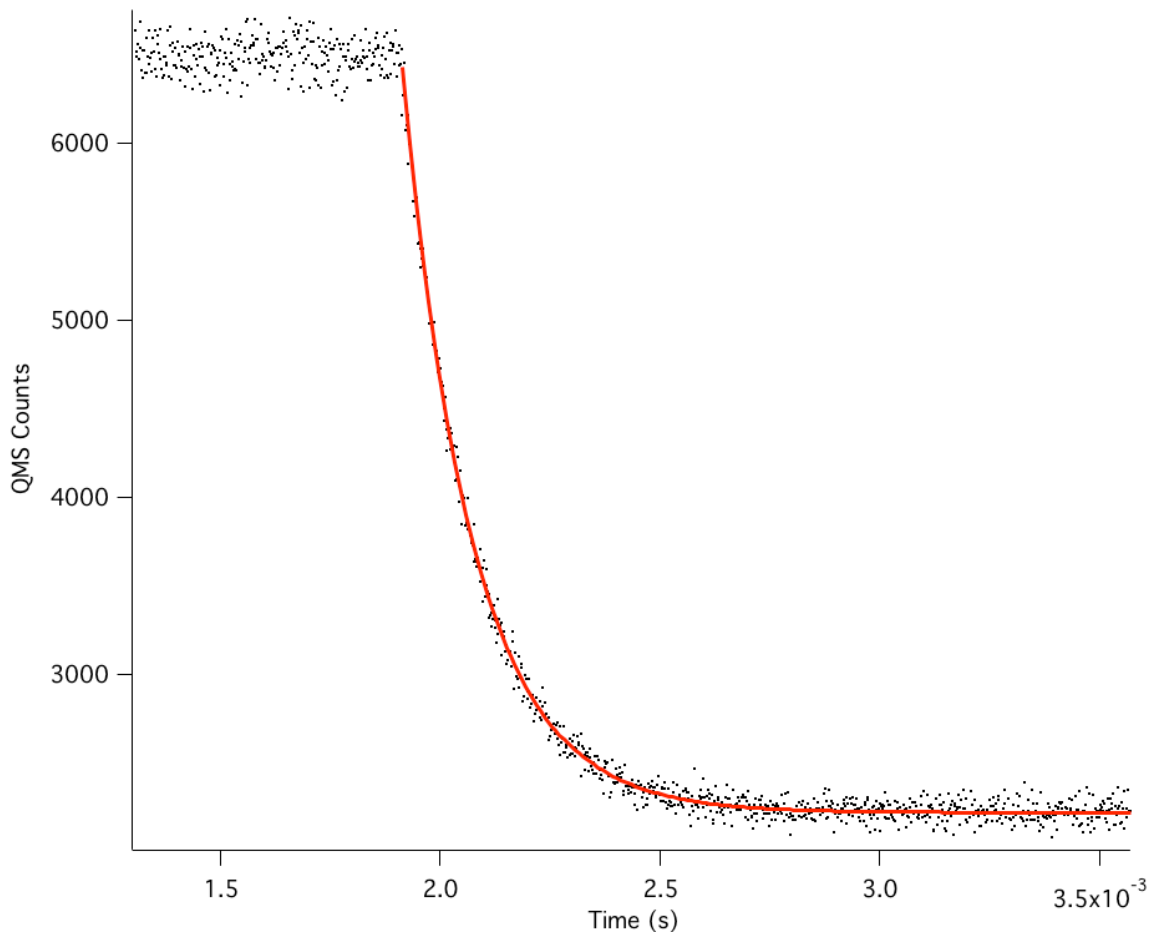


Figure 2.12 – Example of a pumping speed measurement monitoring  $m/z = 16$ . The beam is running until the shutter is closed at  $t = 2$  s.

this decay. A typical methane decay curve can be seen in Figure 2.12. The chamber volume can then be divided by the decay lifetime to give the pumping speed. With a volume of 61 L and a decay lifetime of 157 ms, the pumping speed for methane in this machine is 389 L/s.

To calculate the flux, we need to first multiply the steady state partial pressure of methane by an ion gauge sensitivity factor, which for methane is  $(N_2/CH_4) = 1/1.4$ . This pressure can then be converted to the number of methane molecules via the ideal gas law. The conversion factor is  $3.21 \times 10^{19}$  molecules/torr•L. The result is then multiplied by the pumping speed, which gives the number of molecules being pumped out of the chamber per unit time. During the steady-state conditions of a dose, this is equal to the number of molecules entering the chamber. This is then divided by the spot size on the crystal ( $0.12 \text{ cm}^2$  for the SBVH) to get  $CH_4$  molecules/s• $\text{cm}^2$ . The spot size of the beam on the crystal can be determined by depositing carbon onto the Ir crystal and mapping the carbon using the AES (see section 2.4.2).

#### ***2.4 Data Acquisition and Analysis***

After each dose it is necessary to determine the amount of carbon that reacted on the surface. This is generally done by using one of two methods on this chamber – King and Wells or AES. The flux measurements described above apply only the sticking probabilities determined using AES, as King & Wells measurements have all the necessary information contained within the data from each dose.

### 2.4.1 King & Wells (K&W) Sticking Measurements

The King & Wells (K&W) method is a very efficient way of measuring sticking probabilities higher than about 1 percent [25]. The beam flag and QMS are used to measure the partial pressure in the UHV chamber as a function of time. An example of sticking measurement using this method can be found in Figure 2.13. At  $t=0$ , the beam is blocked by the shutter and the QMS measures only the background at  $m/z=16$ . When the flux of methane is too high, it is sometimes necessary to use a secondary QMS peak representing a methane fragment, typically  $m/z=15$  ( $\text{CH}_3^+$ ). After approximately 10 seconds the shutter is opened and the beam is allowed to enter the chamber, but is blocked from reacting with the crystal by an inert stainless steel beam flag. Since the beam flag is located only an inch or so into the UHV chamber, it is oriented at a  $45^\circ$  angle relative to the beam line to avoid scattering molecules back into the second stage. The change in the signal upon opening the shutter corresponds to  $\Delta_b$  in Figure 2.13. At about  $t=20$  seconds the beam flag is removed via a linear feedthrough, and the methane is allowed to react on the iridium crystal. The change in signal upon moving the beam flag ( $\Delta_r$ ) corresponds to the change in partial pressure of methane due to reaction on the surface. At some time after the beam flag is moved, it is replaced in the beam line and the shutter is closed.

The change in counts of the QMS is directly proportional to the partial pressure of methane, which is in turn directly proportional to the number of methane molecules. Therefore,

$$S_0 = \frac{\# \text{ reactive molecules}}{\# \text{ molecules striking crystal}} = \frac{\Delta_r}{\Delta_b} \quad \text{Equation 2.6}$$

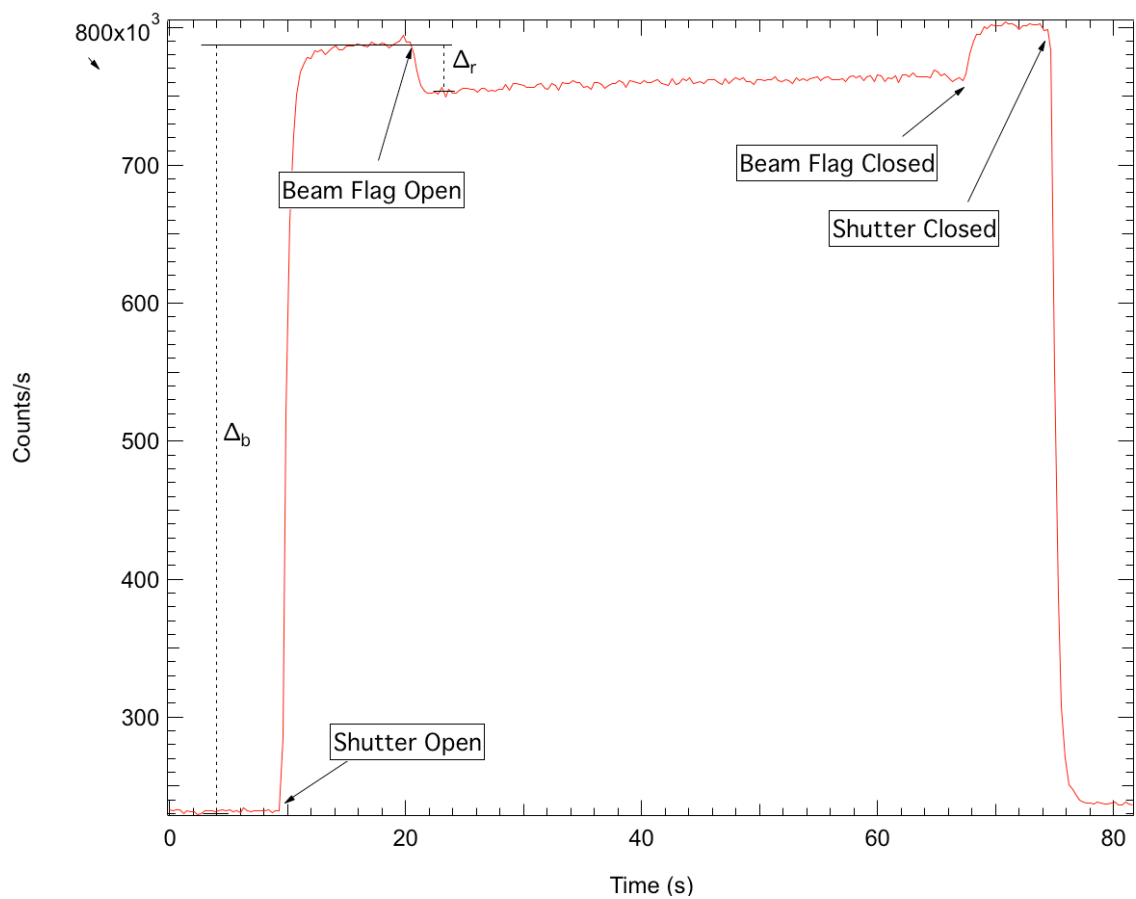


Figure 2.13 – Example of a King & Wells sticking probability measurement.

This method is self-contained and efficient because it gives a direct measurement of the flux of methane and the number of reacting molecules with no calibration necessary. Absolute reactivity measurements with the King & Wells method can be used to calibrate the AES signal as described in section 2.4.2.

There has occasionally been an issue with K&W measurements where the signal would increase with when the beam flag was moved. The actual cause of this has never been determined. One theory is that when the crystal is held at a positive bias (this is necessary when heating to 1000 K), there is some interference with the way the QMS measures the partial pressure. This was resolved by moving the filament slightly closer (0.01") to the crystal, thus moving it further from the QMS ionizer. The problem was considered resolved by running a high kinetic energy beam, guaranteeing reactive molecules, into a cold, inert crystal. The K&W signal was monitored, and no change was observed in the partial pressure of methane when the beam flag was removed.

Another reason for the anomalous K&W measurements could be the "overloading" of the QMS when running dilute beams, as this problem seemed to be worse for the 1% CH<sub>4</sub> in helium beams that were initially being used. The electron energies were lowered on the UTI, thus making the ionization of helium less efficient while minimally affecting the methane ionization. The idea was to minimize the number of ions within the ionizer, and preventing a "coulombic explosion" which could lead to reduced partial pressure measurements because ions are repelled from entering the rod assembly.

### 2.4.2 Auger Electron Spectroscopy (AES) Measurements

Using the AES for measuring sticking probability is slightly more complicated than K&W, but is much more sensitive, allowing for measurement of sticking probabilities well below  $1 \times 10^{-5}$ . A typical AES scan can be seen in Figure 2.14. Since there is a dither on the detector voltage, the data appears as a derivative plot of the signal, and is passed through a lock-in amplifier before being sent to the computer. In order to account for deviations in the absolute auger signal over time, the amount of carbon is determined by calculating the ratio of the carbon signal to the iridium signal. At the low coverages of carbon dosed in these experiments, the iridium signal remains constant.

The C/Ir ratio is determined by dividing the carbon peak at 272 eV by the iridium peak at 229 eV. The peak intensity is measured from peak to peak of the signal, as shown in Figure 2.14. This ratio is proportional to the amount of carbon on the surface. This value is calibrated using King & Wells in conjunction with the AES. A high reactivity dose is run and measured using King & Wells. The exact dose time is recorded, and the flux of methane into the chamber is known. The flux and dose time are used to determine how many methane molecules impinged on the iridium surface, and the King & Wells indicates what fraction of the molecules reacted. The total coverage,  $\theta$ , is calculated from

$$\theta = S_0 \times (\text{flux} \times \text{time}) \quad \text{Equation 2.7}$$

where *time* is the total dose time. This coverage corresponds to the C/Ir ratio calculated from the auger, giving a calibration point. Equation 2.7 can be rearranged to calculate the sticking probability;

$$S_0 = \left( \frac{\theta}{\text{flux} \times \text{time}} \right). \quad \text{Equation 2.8}$$

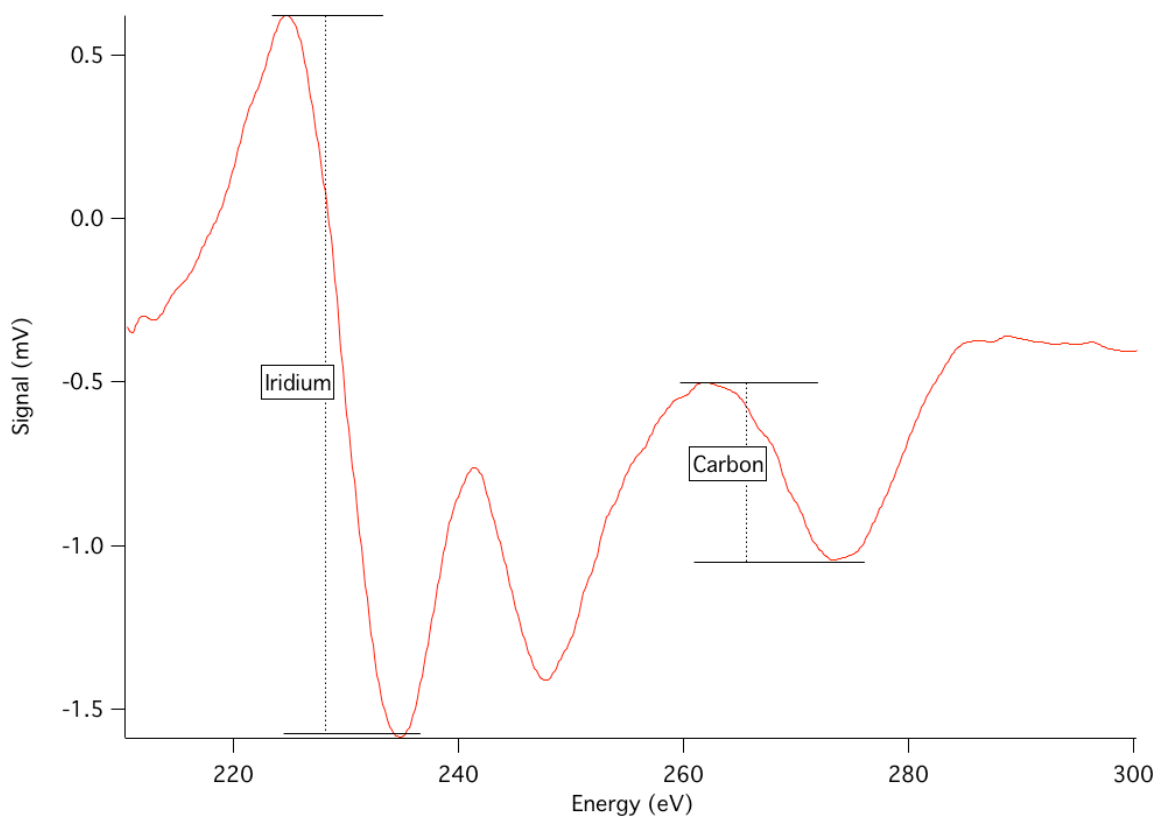


Figure 2.14 – Example of an AES scan after a carbon dose, indicating the Ir and carbon auger peaks used during sticking probability measurements.

## 2.5 References

1. Scoles, G., *Atomic and molecular beam methods: Volume 1*. 1988, New York: Oxford University Press.
2. Kantrowitz, A. and J. Grey, *A High Intensity Source for the Molecular Beam .1. Theoretical*. *Review of Scientific Instruments*, 1951. **22**(5): p. 328-332.
3. Abuaf, N., et al., *Molecular Beams with Energies Above One Electron Volt*. *Science*, 1967. **155**(3765): p. 997-999.
4. Madey, T.E., *Early Applications of Vacuum, from Aristotle to Langmuir*. *Journal of Vacuum Science & Technology a-Vacuum Surfaces and Films*, 1984. **2**(2): p. 110-117.
5. Kleyn, A.W., *Molecular beams and chemical dynamics at surfaces*. *Chemical Society Reviews*, 2003. **32**(2): p. 87-95.
6. Ceyer, S.T., W.J. Siekhaus, and G.A. Somorjai, *Design of a Molecular-Beam Surface Scattering Apparatus for Velocity and Angular-Distribution Measurements*. *Journal of Vacuum Science & Technology*, 1981. **19**(3): p. 726-732.
7. McCabe, P.R., L.B.F. Juurlink, and A.L. Utz, *A molecular beam apparatus for eigenstate-resolved studies of gas-surface reactivity*. *Rev. Sci. Instrum.*, 2000. **71**: p. 42-53.
8. Comsa, G., *Surface Scattering of Thermal-Energy He Beams - from the Proof of the Wave Nature of Atoms to a Versatile and Efficient Surface Probe*. *Surface Science*, 1994. **300**(1-3): p. 77-91.
9. Campargue, R., *Atomic and molecular beams : The state of the art 2000*. 2001, Berlin ; New York: Springer.

10. Juurlink, L.B.F., D.R. Killelea, and A.L. Utz, *State-resolved probes of methane dissociation dynamics*. *Progress in Surface Science*, 2009. **84**(3-4): p. 69-134.
11. Killelea, D.R., *Bond-Selective Control of a Gas-Surface Reaction*, in *Chemistry*. 2007, Tufts University: Medford, MA.
12. Juurlink, L., *Eigenstate-resolved measurements of methane dissociation on Ni(100)*, in *Chemistry*. 2000, Tufts University: Medford, MA.
13. Smith, R.R., *Rovibrational State-Resolved Studies of Methane Dissociation on Ni(111)*, in *Chemistry*. 2003, Tufts University: Medford, MA.
14. Auerbach, D., Rettner, C.T., *High-temperature supersonic molecular-beam source*. *Rev. Sci. Instr.*, 1992. **63**(8): p. 3939.
15. Moore, J.H., C.C. Davis, and M.A. Coplan, *Building Scientific Apparatus*. 1983, London: Addison-Wesley.
16. Yates, J.T., *Experimental innovations in surface science : a guide to practical laboratory methods and instruments*. 1998, New York: AIP Press : Springer.
17. Beckerle, J.D., *Dynamics of Molecular Adsorption*, in *Chemistry*. 1988, MIT: Cambridge, MA.
18. Smith, R.R., *Rovibrational State-Resolved Studies of Methane Dissociation on Ni(111)*, in *Chemistry*. 2003, Tufts University: Medford, MA.
19. Musket, R.G., W. McLeana, C.A. Colmenaresa, D.M. Makowiecki, W.J. Siekhaus, *Preparation of Atomically Clean Surfaces of Selected Elements - A Review*. *Applied Surface Science*, 1982. **10**(2): p. 143-207.
20. Seets, D.C., et al., *Dissociative chemisorption of methane on Ir(111): Evidence for direct and trapping-mediated mechanisms*. *J. Chem. Phys.*, 1997. **107**(23): p. 10229-10241.

21. Woodruff, D.P. and T.A. Delchar, *Modern techniques of surface science*. 2nd ed. Cambridge solid state science series. 1994, Cambridge ; New York: Cambridge University Press.
22. Chan, C.M., E.D. Williams, and W.H. Weinberg, *Debye Temperatures of the (110) and (111) Surfaces of Iridium by LEED*. *Surface Science*, 1979. **82**(2): p. L577-L581.
23. Nieuwenhuys, B.E. and G.A. Somorjai, *Adsorption of Carbon Monoxide, Oxygen, Hydrogen, Nitrogen, Ethylene, and Benzene on an Ir(110) Surface - Correlation with Other Iridium Crystal Faces*. *Surface Science*, 1978. **72**(1): p. 8-32.
24. Scoles, G., *Atomic and Molecular Beam Methods*. Vol. 2. 1992, New York: Oxford University Press.
25. King, D.A. and M.G. Wells, *Reaction mechanism in chemisorption kinetics. Nitrogen on the {100} plane of tungsten*. *Proc. Roy. Soc. London, Ser. A*, 1974. **339**(1617): p. 245-69.

## Chapter 3 Contributions of Vibrationally Excited States to the Thermally Averaged Reactivity

### 3.1 Introduction

#### 3.1.1 Steam Reformers and Thermal Excitation

The rate-limiting step in the chief industrial pathway for hydrogen gas production, the steam-reforming reaction, is the cleavage of a C-H bond in methane [1, 2]. In this process methane from natural gas reacts with steam over a nickel catalyst to produce “syngas” - a 3:1 mixture of hydrogen and carbon monoxide. It is an inefficient reaction that takes place at high temperatures and pressures, usually above 1000 K and 20 atm in order to obtain favorable reaction kinetics. One key to improving this process is determining what is happening in the initial C-H bond cleavage step. A greater understanding of this step could point the way to cheaper and more efficient ways to produce hydrogen gas, which can in turn be used in fuel cells [3, 4]. Also, methane activation is a good model for more complex gas-surface reactions.

Molecular beam experiments show how translational energy in the methane reagent, which can be tuned by changing the gas mix and temperature, can activate the reaction [5]. Conventional experiments prepare an ensemble of reactants with well defined translational energy but a spread of vibrational energies. Measurements of methane reactivity on nickel single crystal surfaces show strong translational activation. However, the activation of the reaction via translational energy has been shown to depend only on the component of translational energy that is normal to the crystal surface [5, 6].

Low translational energy molecules produced by using a low nozzle temperature have little vibrational energy. Raising the temperature of the gas to achieve higher translational energies has the additional effect of thermally exciting vibrations within the methane, creating a translationally and vibrationally hot reactant. In a reactor, the high temperature conditions result in methane molecules with significant vibrational energy content. However, since the incident angles of the reactants will be evenly distributed among all angles, the majority of reactants will be vibrationally hot but have little normal incident energy. These vibrations may provide the activation for reaction in these reformers. Further investigation into which vibrations are more effective will provide insight into how the C-H bond is broken.

### *3.1.2 Eigenstate-resolved Measurements*

Molecular beam experiments show that increasing gas temperature increases the sticking probability at a given translational energy [7]. Laser excitation has also been used to excite specific vibrational and rotational states of the methane, giving insight into the relative efficiencies of individual eigenstates at promoting reactivity [8-12]. These laser experiments have shown that the reaction probability is not statistical at the single molecule level, meaning that the ability of a methane to dissociate on the surface depends on what type of vibrational energy it contains. Certain vibrational modes are more effective than translation at facilitating reactivity, and some are less. If the system behaved in a statistical manner, only the total energy would matter, meaning translational, rotational, and vibrational energy would all be equally effective. Under thermal conditions, vibrational state populations are defined by a Boltzmann distribution. The

thermally averaged reaction probability will be a population-weighted sum of reaction probabilities from each vibrational state.

State-resolved reactivity measurements are obtained from reaction probabilities of ensembles with and without the laser. For example, for a methane experiment with laser excitation of  $\nu_3$ , the sticking probability,  $S_0^{laser\ on}$ , is defined as [7]

$$S_0^{laser\ on} = (f_{\nu=0} - f_{exc})S_0^{\nu=0} + (1 - f_{\nu=0})S_0^{\nu>0} + f_{exc}S_0^{\nu_3}, \quad \text{Equation 3.1}$$

where  $f_{\nu=0}$  and  $f_{exc}$  are the fraction of methane in the ground vibrational state and the excited state ( $\nu_3$ ), respectively,  $S_0^{\nu=0}$  and  $S_0^{\nu_3}$  are the sticking probabilities from the ground vibrational state and  $\nu_3$ , and  $S_0^{\nu>0}$  is the average reactivity of all thermally populated excited vibrational states. The observed sticking probability with the laser is the sum of the probabilities for the methane remaining in the ground state after excitation, the thermally excited methane due to the nozzle temperature, and the methane excited into  $\nu_3$ . It is important to note that laser excitation from  $\nu=0$  to  $\nu_3$  only affects the population of  $\nu=0$  and  $\nu_3$ , not the thermally excited molecules. Therefore, by measuring reactivity of the ensemble without laser excitation under the same conditions, the contribution from the  $\nu>0$  fraction of the beam can be cancelled via subtraction from the laser on dose. The sticking probability for  $\nu_3$  can then be directly calculated from [7]:

$$S_0^{\nu_3} = \frac{S_0^{laser\ on} - S_0^{laser\ off}}{f_{exc}^{\nu_3}} + S_0^{\nu=0} \quad \text{Equation 3.2}$$

While the contribution to sticking from  $v=0$  methane is often negligible, it is in general not possible to measure  $S_0^{v=0}$  directly. Therefore, to obtain the best estimate of the ability of individual vibrational states to promote the reaction, the reactivity of the ground vibrational state of methane must be determined.

This chapter describes a model that combines thermal and eigenstate-resolved data to assess the relative contributions of each individual vibrational state to the overall reactivity at a given gas temperature. The laser off data at low gas temperatures place a tight upper limit on the reaction probability curve for the vibrational ground state. Reactivity curves for all excited vibrational states are then derived from the  $v=0$  curve. A model data set is created to show general trends in sticking probabilities, including insight into which vibrational states dominate reactivity at different translational energies. The model provides insight into the identity of species most responsible for reactivity under thermal reactor conditions.

Harrison and coworkers adapted microcanonical unimolecular rate theory to model gas-surface reactions, including methane on nickel [7, 13, 14]. The model assumes rapid intramolecular vibrational redistribution (IVR) prior to reacting on the surface, resulting in all possible energetic states being statistically populated at the transition state. While they were modestly successful at modeling experimental results with fewer variables than the model presented here, it is likely due to the statistical distribution of energetic states within the ensemble of reacting molecules in the experiments. Their results are the ensemble averaged reaction probabilities. In contrast, the model presented in this chapter provides insight into the contributions of individual vibrational

states and how they sum to give the total ensemble reaction probability in a thermal gas.

## 3.2 *Molecular Beams – Methane on Nickel*

### 3.2.1 *Functional Form of Sticking Curves*

The reaction of methane on a nickel single crystal has been shown to be an activated process by either translational [15] or, in some cases, vibrational [9, 16, 17] energy. It is considered an activated process because there is some non-zero energetic barrier to reactivity, and reaction probability increases with translational energy. The functional form of the reaction probability curves for methane is similar to that of molecular beam experiments on other single crystalline transition metals [6, 18]. A sticking curve for the reaction of methane on Ni(111) can be seen in Figure 3.1 [16]. This figure presents the data for both laser off and state-resolved ( $\nu_3$ ) experiments. The exponential increase of sticking probability with energy reflects the barrier to reactivity. The shapes of these curves can be fit very well with an error function [19], defined as

$$S_0(E_i) = \frac{A}{2} \left[ 1 + \operatorname{erf} \left( \frac{E_i - E_0}{W} \right) \right], \quad \text{Equation 3.3}$$

where  $A$  is the asymptote,  $E_i$  is the incident translational energy,  $E_0$  is the center of the curve, and  $W$  is the width. If there were a single 1-D barrier along the translational coordinate, the sticking curve would simply be a step function. However, the error function shape suggests that there is actually an effective multi-dimensional distribution of barriers projected along the one dimensional

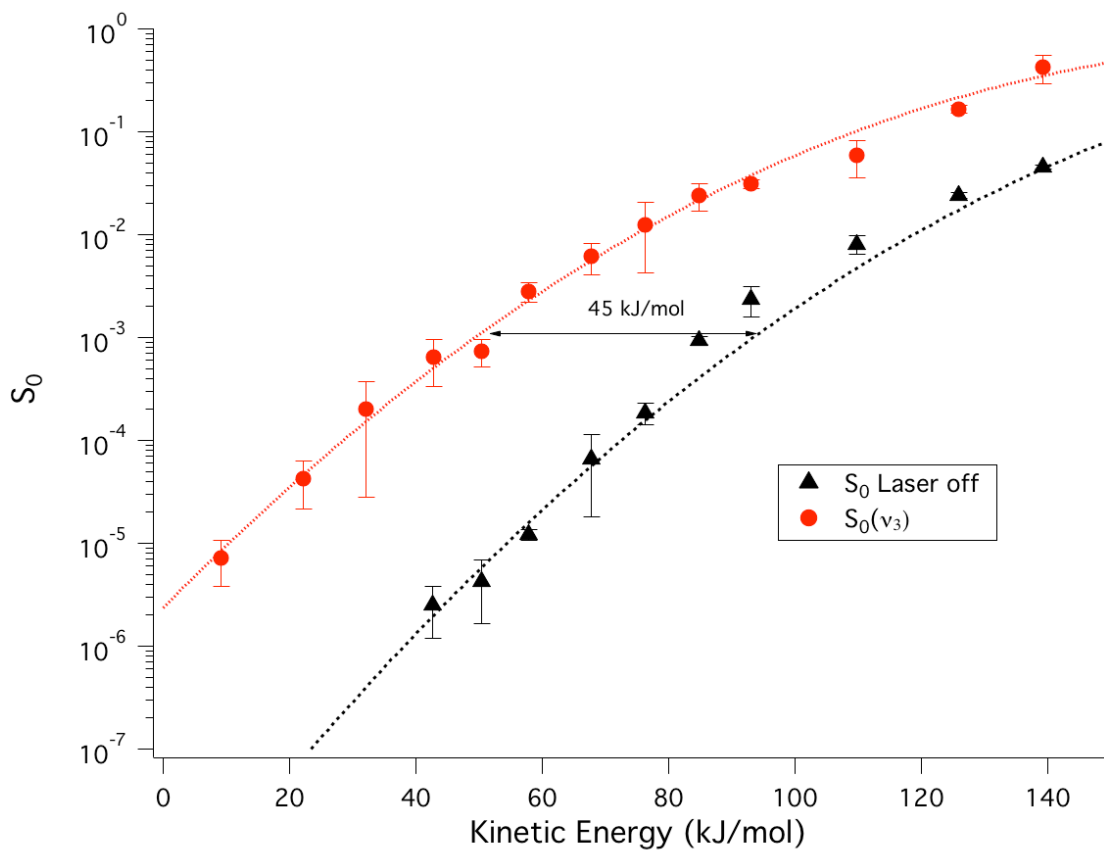


Figure 3.1 - Sticking curves for  $\text{CH}_4$  on  $\text{Ni}(111)$ , state-resolved ( $v_3$ ) [16] and laser off.

translational coordinate [20]. This distribution could be due to geometric factors related to the reaction geometry. Rotations, vibrations, and surface atom displacement that deviate from the ideal transition state geometry, for example, can all lead to an increase in the barrier to dissociation.

Finally, it should be noted that both the laser off and state-resolved sticking curves maintain the same error function shape and asymptote. This implies that each vibrational state can be defined by a unique error function. We extend this feature to other vibrational states to simplify the modeling of individual sticking curves.

### 3.2.2 Reaction Curve as a Sum of States

Before moving on to treat methane reactivity, a discussion of how state-resolved thermally averaged data describe  $D_2$  reactivity is helpful. Error functions were first used to fit gas-surface reaction data by Michelsen, et al. [21], in an attempt to model the reactivity of  $H_2$  and  $D_2$  on copper single crystal surfaces [18, 22-25]. They expanded on this model by defining the total sticking probability as a sum of error functions for the individual vibrational states of  $H_2$ ;

$$S_0(v, E) = \sum_v P(v) \left\{ \frac{A(v)}{2} \left[ 1 + \operatorname{erf} \left( \frac{E_i - E_0(v)}{W(v)} \right) \right] \right\} \quad \text{Equation 3.4}$$

where the additional term,  $P(v)$ , is the Boltzmann probability for state  $v$ . Again, this assumes that each vibrational state has its own sticking curve, as shown in the eigenstate-resolved data in Figure 3.1. This worked well for the data, since the vibrational structure is relatively simple. Hydrogen and deuterium have a single vibrational mode, and populations of excited vibrational states are

relatively small. They found that vibrationally excited molecules dominated reactivity at lower translational energies, while ground state hydrogen and deuterium had the largest reactivity contributions at high translational energy. In fact, they were able to see discrete steps in the overall sticking curve that indicated how each individual curve was shifted in relation to the ground state.

This can be explained by the effect that vibrational energy has on its individual sticking curve. Figure 3.2 shows an example of how the entire sticking curve is shifted to lower energy, meaning that because of the presence of vibrational energy, less translational energy is needed to react. In order to quantify just how effective that particular vibration is in promoting reactivity compared to translational energy, the quantity efficacy,  $\eta_{vib}$ , is used:

$$\eta_{vib} = \frac{\Delta E_{trans}}{E_{vib}}. \quad \text{Equation 3.5}$$

Here,  $\Delta E_{trans}$  is the shift in the sticking curve along the translational energy axis, and  $E_{vib}$  is the vibrational energy. Therefore, an efficacy of zero would mean the vibration does not promote reactivity, and an efficacy of 1 would mean that the vibrational and translational energy are equally effective in promoting reactivity.

As seen in Equation 3.4, the reaction probability curve averaged over vibrational states is a sum of the sticking curves for each vibrational state, weighted according to the population of that particular state as a function of gas temperature. In a more general form,

$$S_0(v, E_i, T_n) = \sum_v f(v, T_n) S_0(v, E_i), \quad \text{Equation 3.6}$$

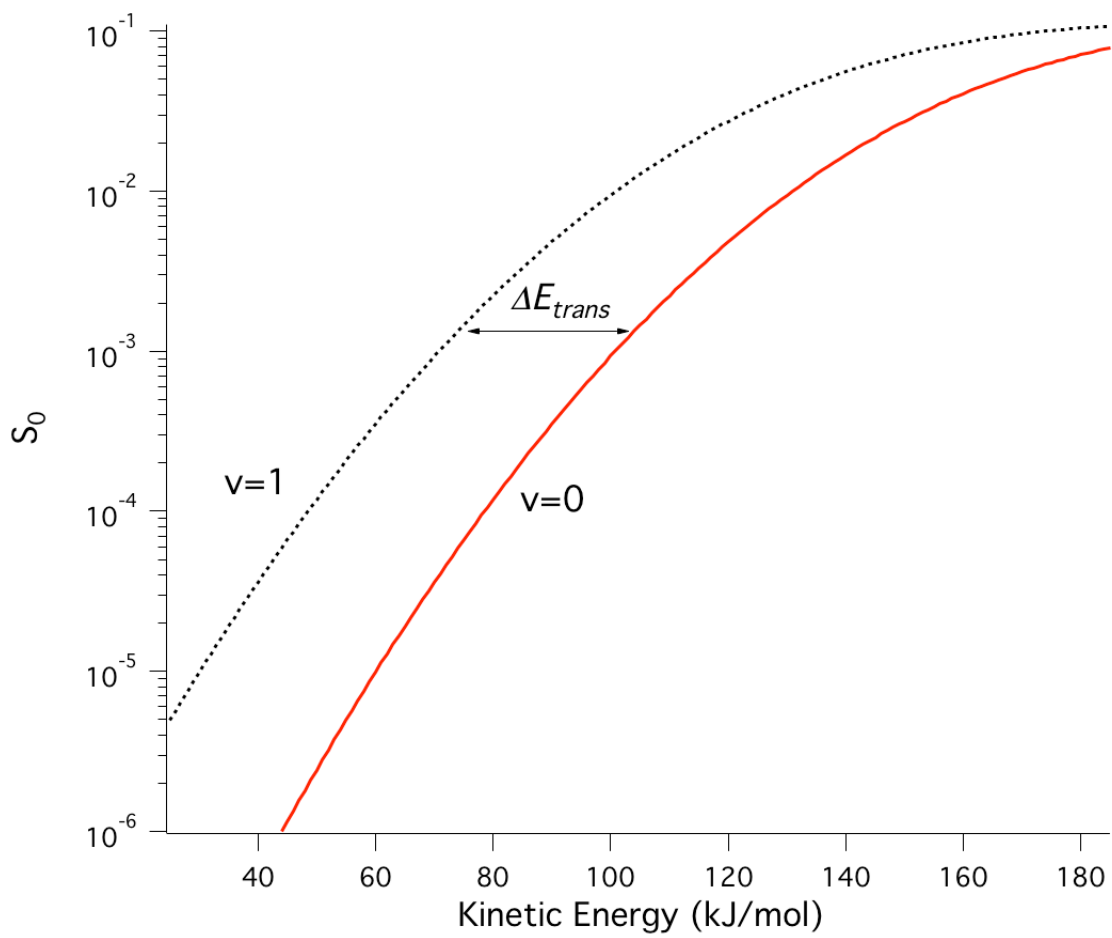


Figure 3.2 - Effect of vibrational energy on the position of the  $v>0$  sticking curve.

where  $f(v, T_n)$  is the fraction of molecules in vibrational state  $v$  at a particular nozzle temperature,  $T_n$ , and  $S_0(v, E_i)$  is the sticking probability curve for vibrational state  $v$  as a function of incident energy,  $E_i$ .

Figure 3.3 plots the error functions for the first three quanta of the single vibrational mode of  $D_2$  as reported by Michelsen, et al. Figure 3.3a shows the state-resolved curves, and Figure 3.3b population weights these curves and then adds them together. With  $D_2$  there are discrete steps to the total error function. These steps result from the relatively large size of a  $D_2$  vibrational quantum and the extremely sparse vibrational structure of this diatomic molecule.

This shifting of error functions should apply to methane dissociation also, but the explicit determination of individual curves is not as simple experimentally as it is with  $H_2$  and  $D_2$ . At lower gas temperatures (at or below RT) most of the methane molecules are in the ground vibrational state,  $v=0$ . Unlike diatomics such as  $H_2$ , polyatomic methane has a number of highly degenerate lower energy vibrational states [26], so as the gas is heated, these states begin to become significantly populated at a lower temperature than is the case for  $H_2$  and  $D_2$ . This leads to a significant number of molecules with vibrational energy content even at modest nozzle temperatures. Figure 3.4 shows the relative populations of vibrational states as a function of several different nozzle temperatures. Details of the calculations can be found in section 3.4.1. At 300 K, over 99% of methane molecules are in the ground vibrational state, with the bulk of the remaining in the  $\nu_2$  and  $\nu_4$  bending modes, which are doubly and triply degenerate, respectively. When the nozzle temperature is raised to 550 K, about 13% of the molecules are vibrationally excited, and the

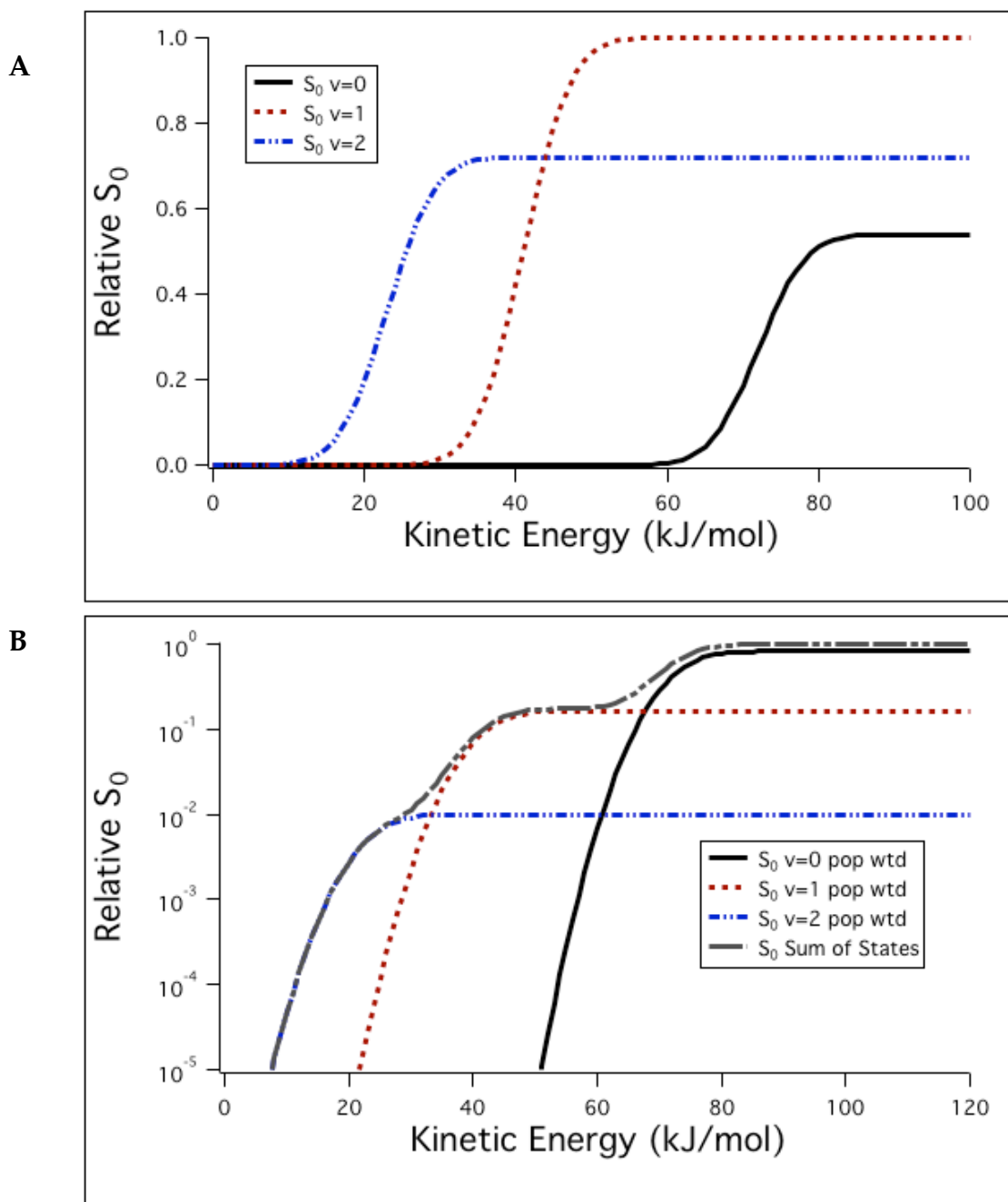


Figure 3.3 – **A** - individual s-curves for  $v=0, 1,$  and  $2$  of  $H_2$ ; **B** - population weighted curves and sum over all states [27].

higher energy stretches start to pick up population. Finally, with a nozzle temperature of 1050 K, the ground state population drops to only about 41%. The higher energy modes ( $> 35$  kJ/mol) now make up about 15% of the molecules.

Since methane has many more states populated at the same given temperature, there are a large number of error functions that contribute to the overall sticking curve. Unlike the case of diatomics, this makes it essentially impossible to determine individual vibrational state curves experimentally from ensemble averaged data.

### *3.2.3 Rotational and Vibrational Cooling in a Supersonic Expansion*

As can be seen in Figure 3.4, methane vibrational states tend to fall into groupings of similar energy. These groupings are called polyads, and each polyad is named according to the number of available states within that grouping: dyad, pentad, octad, etc. In the initial expansion of the methane from the nozzle, rotations are effectively cooled [28], while vibrations are not [29-31].

The rotational constant for methane is only about  $5\text{ cm}^{-1}$  [32]. The spacing between rotational energy levels is therefore smaller than or comparable to collision energies in the nozzle. Rotational energy exchange with translational degrees of freedom is relatively efficient, so rotations can be effectively cooled, or quenched, by collisions upon expansion. This results in a rotational temperature that is much lower than the nozzle temperature [33]. On the other hand, the smallest vibrational quantum is  $1311\text{ cm}^{-1}$  ( $\nu_4$ ). The quenching of this much energy in a single collision within a supersonic expansion has a very low probability, resulting in poor cooling of vibrations within the beam. However,

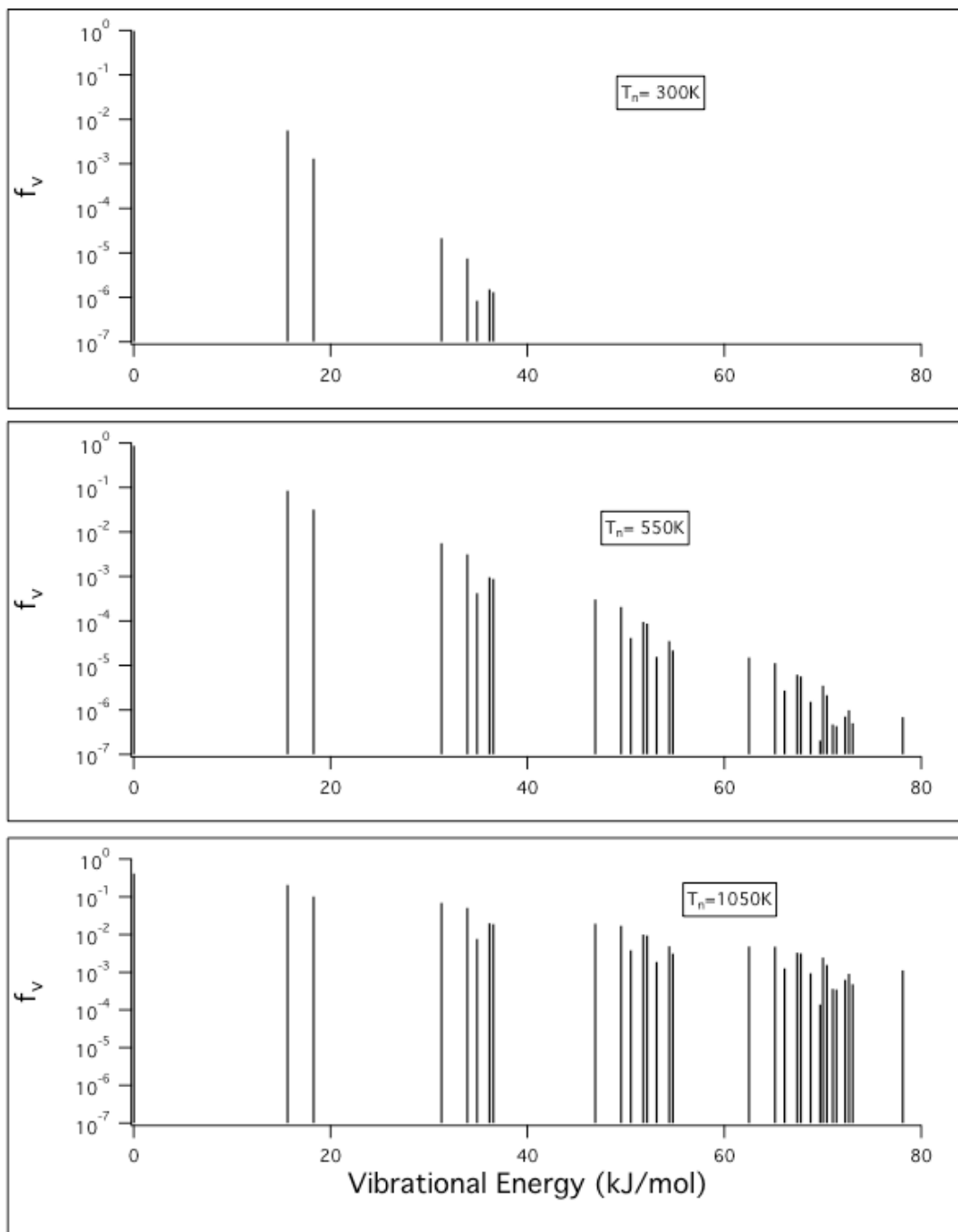


Figure 3.4 – Relative vibrational state populations in methane as a function of nozzle temperature.

within each polyad grouping the spacing between states is relatively small. This leads to effective cooling of the vibrational temperature within each polyad, but very little population transfer between polyads [31]. The resulting population of vibrational states in the beam is therefore thermal, with the integrated population of each polyad remaining approximately constant, but with cooling within each polyad.

### ***3.3 Obtaining an Estimate of $S_0^{v=0}$***

#### ***3.3.1 Methodology and Results***

The first step in developing the model is to determine the reaction probability of the ground vibrational state of methane from experimental data. This ground-state, or  $v=0$  reaction probability curve, will be the basis for modeling the vibrationally excited states. This curve will be obtained by fitting low and high nozzle temperature data with error functions. While not ideal, this curve will give a fairly good estimate of the ground state since a vast majority of the molecules (>98%) will have no vibrational energy at low nozzle temperature. A more rigorous calculation of the ground state can be done with an expanded data set. This method is detailed in section 3.5.

Figure 3.5 shows plots of the reaction probability for methane on Ni(111) at low nozzle temperatures [9] (below 450 K) and at  $T_n=1050$  K as a function of normal incident kinetic energy. The reaction probability increases exponentially with translational energy, and also increases with nozzle temperature. The data

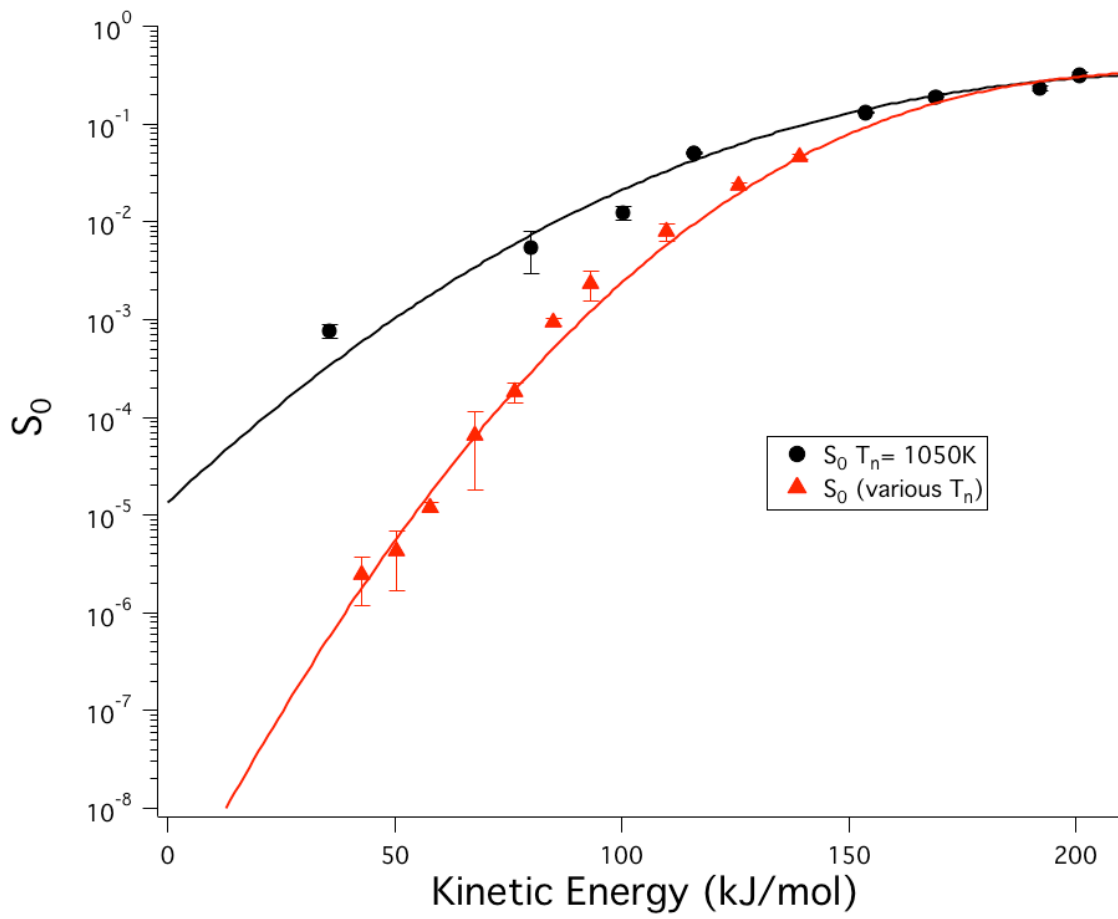


Figure 3.5 – Experimental data for  $T_n < 450\text{ K}$  [9] and  $T_n = 1050\text{ K}$  on Ni(111) with best fit error functions.

show that both the vibrationally cold and thermally excited molecules seem to be approaching the same reaction asymptote. This implies that once the molecules have enough energy in the translational coordinate to react, the presence of vibrational energy has minimal effect. Therefore the asymptote of each individual vibrational state is likely to be equal. On Ni(111) and Ni(100), this asymptote seems to occur at a sticking probability of about 35%. The transition state of methane is largely defined by geometric factors [34]. It is possible that two-thirds of the incoming methane molecules arrive at the surface in particularly unfavorable reaction geometries, while the remaining third can access the transition state over the experimentally measured range of translational energies. It is possible that at some much higher translational energy, a new channel to reactivity will open up and the reaction probability may increase further, possibly even reaching unity. However, with current beam techniques it is impossible to prepare molecules with translational energy much higher than 200 kJ/mol, so there has been no experimental evidence of any further increase in reactivity.

The first step in determining the  $v=0$  curve is to fit the 1050 K nozzle data with an error function, since this data goes to higher translational energies and will give a better estimate of the asymptote. The fit can be found on Figure 3.5. The asymptote was determined to be about 37%. This value is consistent with the state-resolved asymptotic reactivity measured for a range of excited vibrational states of methane on Ni(111) [7, 9, 10, 16, 17]. Once this is known, an error function is fit to the low nozzle temperature data and is forced to reach the same asymptote. The open triangle symbols about 75 kJ/mol in the  $v=0$  data were not used to find the error function. These data were only included for

completion of the data set. These points were taken using higher nozzle temperatures, and show an increased sticking probability due to thermal excitation of vibrations. The only higher nozzle temperature point used was at 135 kJ/mol to give more definition to the error curve. At this energy, the sticking probability is close to the asymptote, meaning the thermally excited states have much less of an effect on the overall sticking. This  $v=0$  curve is the basis for modeling the sticking curves for the rest of the vibrational states.

### ***3.4 Thermal Averaging over Vibrational States***

#### ***3.4.1 Methodology***

In this part of the model, a sticking curve is calculated for each vibrational state, and then weighted by the fractional population of that state. All of the curves are then added up to give the overall sticking curve for that particular nozzle temperature. The synthetic curves are all based on the  $v=0$  error function calculated in section 3.3, on the assumption that all of the individual vibrational states have error function of the same shape. Also, each curve will be forced to reach the same asymptote as the  $v=0$  curve. These asymptotes are consistent with state-resolved measurements on Ni(111).

As shown in section 3.2, the addition of vibrational energy causes a shift in the error function to lower energy. This challenge in modeling the data is in knowing how much to shift the curve for each state. Therefore, three limiting approaches are taken to assess which best models experimental data. The first will shift all vibrational states by the energy of that state, meaning every

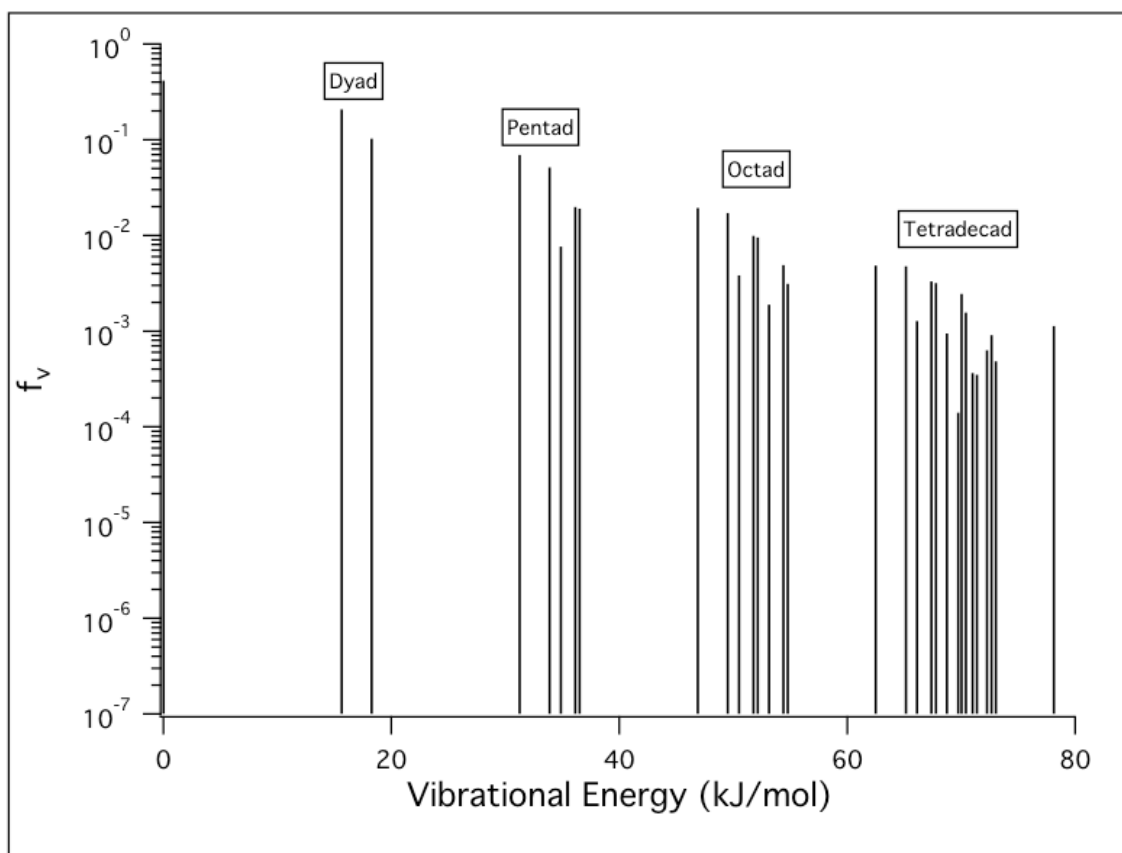


Figure 3.6 – Normalized vibrational energy populations for a 1050K nozzle with polyads labeled.

vibration is assumed to have an efficacy of 1. For  $\nu_3$ , for example, the curve will shift by 36 kJ/mol for  $v=1$ , 72 kJ/mol for  $v=2$ , and so on. The second approach will shift each state according to experimentally determined efficacies determined from state-resolved measurements. For those not available, an efficacy will be inferred based on similar vibrational modes. Therefore,  $\nu_1$  and  $\nu_3$  will have efficacies of 1.25, and  $\nu_2$  and  $\nu_4$  of 0.75 [17]. Finally, the third approach will shift the first quantum of vibration according to the second approach, but will scale the efficacy of additional excitation in a single mode by the square root of the total number of vibrational quanta. This leads to a diminished efficacy for overtone states, as was seen in the  $D_2/Cu$  data presented in section 3.2.2.

The population weighting for each state is determined by the fraction of molecules in that state. The fraction of molecules in each vibrational state,  $f_{exc}$  is found by calculating the Boltzmann factor for each state and dividing by the partition function:

$$\frac{n_i}{N} = \frac{g_i e^{-\frac{\epsilon_i}{k_B T_n}}}{q} ; \quad \text{Equation 3.7}$$

where  $\epsilon_i$  is the energy of vibrational state  $i$ ,  $g_i$  is the degeneracy of that state, and

$$q = \sum_i g_i e^{-\frac{\epsilon_i}{k_B T_n}} . \quad \text{Equation 3.8}$$

The normalized populations have been plotted in Figure 3.4 for the 1050 K nozzle temperature, with the polyads labeled. Thermal populations are assumed here, but variations could be introduced to model intra-polyad cooling.

### *3.4.1 Results and Discussion*

Plots of the model sticking curves at a fixed nozzle temperature appear in Figure 3.7. The models are compared with measured reactivity at  $T_n = 1050$  K. All three models seem to do a respectable job of modeling this set of experimental data, with the first and second approaches appearing to do a slightly better job. The third model, with diminishing returns on additional quanta of energy, seems to underestimate the reactivity over much of the range of data. This is likely due to the fact that the square root kills off the shifting of the error functions too quickly. Alternatively, the efficacy of the  $\nu_1$  and  $\nu_2$  modes could be greater than estimated. Overall, this model does a very good job of predicting thermal sticking probabilities, though a more complete data set spanning more nozzle temperatures would provide a more stringent test of the models.

Eigenstate-resolved data has clearly shown that the efficacies of the different vibrational modes are not equal. The data splits the difference between the first two models, which implies that while there may be some level of preference for one vibration over another, in a thermal beam, where many, many states are populated, individual differences tend to average out. Also, in eigenstate-resolved experiments, the population of the excited state is large compared to all other vibrational states, and even the ground state. In a thermal beam, the population weighting has a larger effect on what vibrations contribute at a given energy than the relative efficacies of those vibrations. Now that it has been shown that the model is adequate for predicting thermal data, the major contributors to sticking as a function of temperature can be explored.

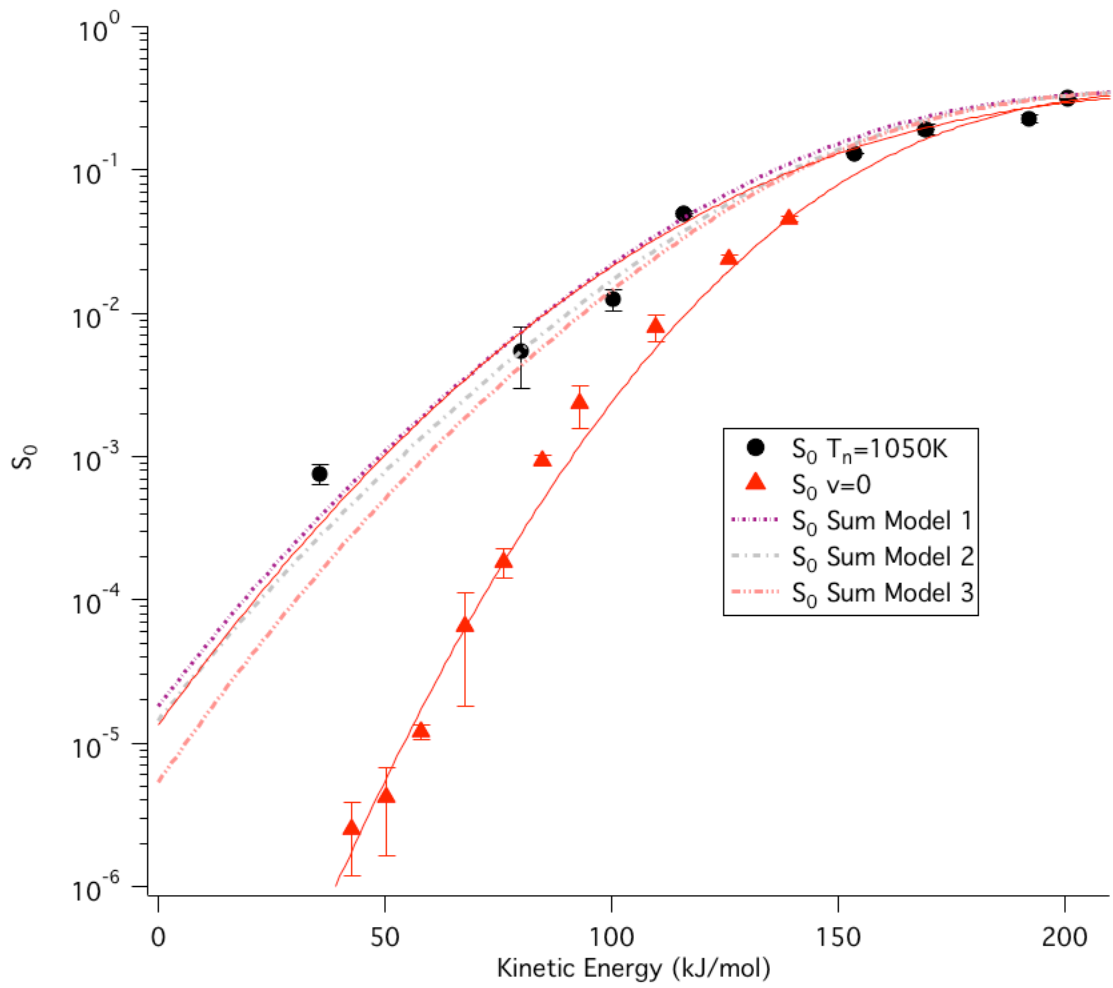


Figure 3.7 – Plots of the 1050 K curves for the three different version of the model, along with experimental 1050 K data.

The reactivity of states in a particular polyad is pooled to simplify analysis. Figure 3.8 shows the contributions for the first four polyads as a function of translational energy. The first four polyads include the sticking curves for all vibrations up to 75 kJ/mol, and account for nearly 99% of the molecules at a temperature of 1050K.

The first region of interest is the sticking probability in the high translational energy regime, greater than 175 kJ/mol. Here, the  $v=0$  sticking curve dominates. In terms of the model, this was expected because at the higher energies, all of the individual curves have reach their asymptote, so the dominant curve is going to be the one with the highest population, which at 1050K is still the ground vibrational state. This simplified picture applies to experiment, too. It was mentioned previously as the translational energy increases towards the reactive asymptote, the vibrations matter less and less, so the state with the highest population dominates. There is enough kinetic energy in the methane to surmount the reaction barrier without significant additional contributions from vibrations.

As translational energy decreases, the  $v=0$  curve begins to drop off first, followed in order by the dyad, pentad, octad, and tetradecad. In the region of 100-175 kJ/mol, there is a mixed contribution, with all states contributing significant amounts. Here, the intermediate vibrational energy states – dyad, pentad, octad – have slightly more impact on the reaction probability, as the  $v=0$  curve is dropping off quickly, and the tetradecad states are still low in population relative to other states.

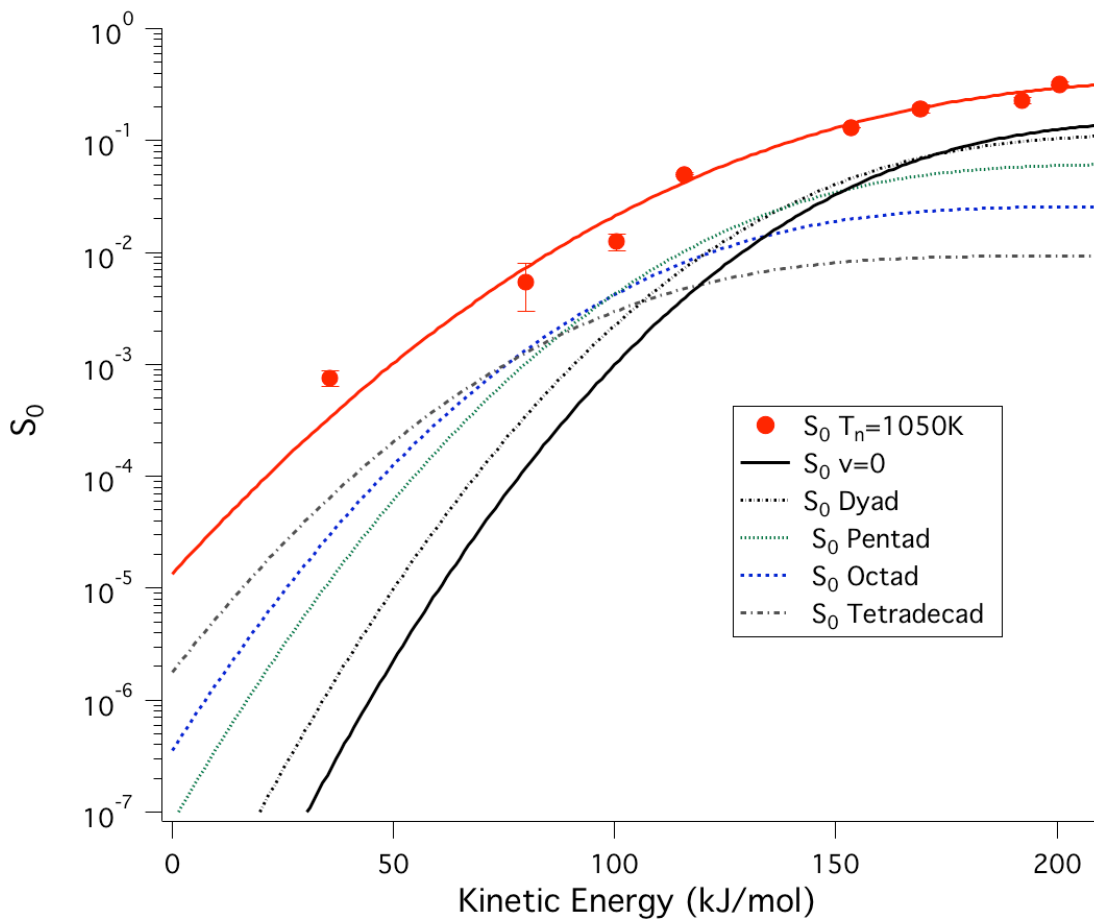


Figure 3.8 – Model sticking probabilities for the ground state and first four polyads as a function of kinetic energy for the second model.

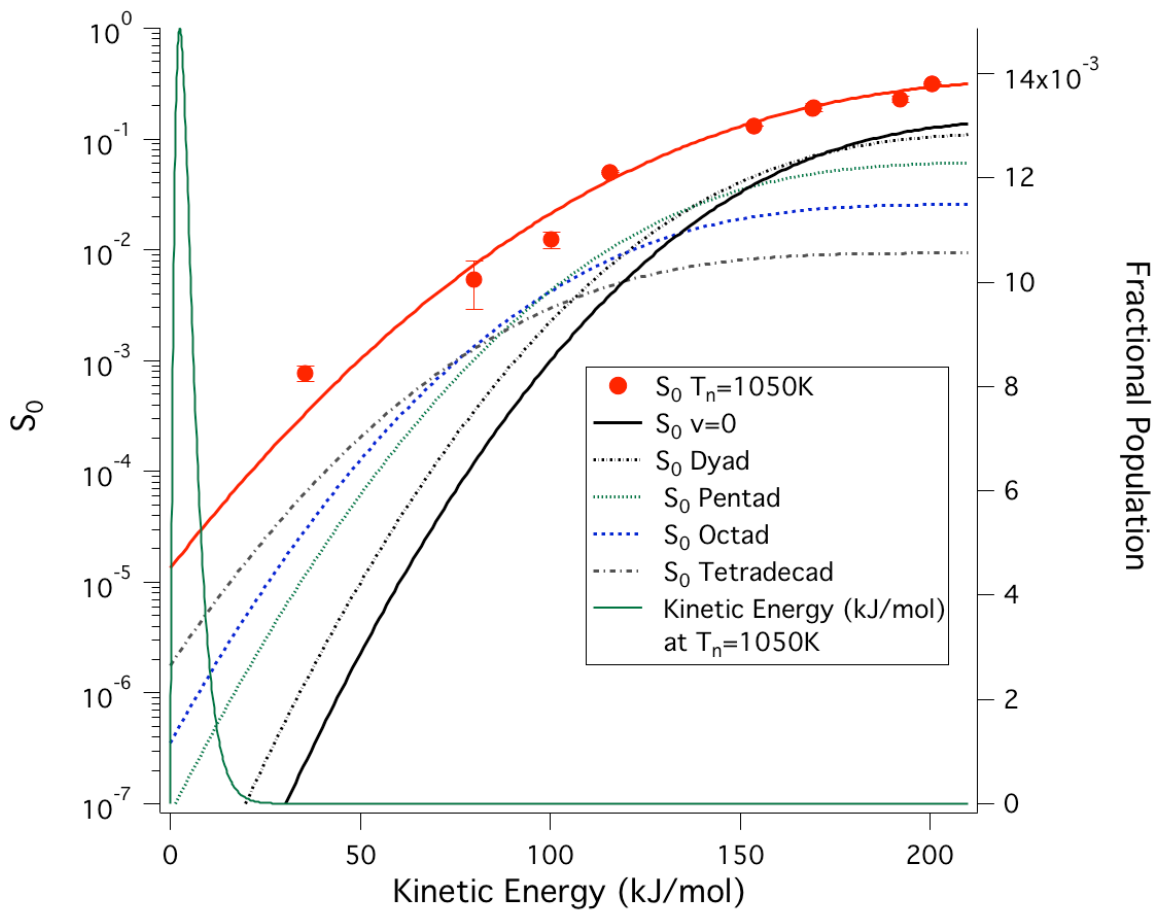


Figure 3.9 – Overlay of the 1-D kinetic energy distribution of methane at  $T_n=1050$  K and sticking curves. The most probable energy of the methane is about 8.7 kJ/mol, while the most probable *normal* energy is 2.9 kJ/mol.

Finally, at the lowest translational energies, the tetradecad states begin to dominate. This grouping contains the highest number of curves, but still has very low total population. Below 75 kJ/mol, the sticking probability is dominated by these states. This means that the reactivity is largely governed by methane molecules in the beam that are in the tetradecad and higher states. This is also the region of the sticking curve that is most like the molecules in a steam reforming reactor. Figure 3.9 shows the kinetic energy distribution of methane molecules at 1050K, overlaid with the 1050 K nozzle temperature data. A large number of the molecules have less than 40 kJ/mol, where the model indicates that the vibrations play a significant role. Here, the ground state molecules are two orders of magnitude less likely to react.

### **3.5 *Conclusions and Future Applications of the Model***

This simple model reproduces the reactivity of beam-surface scattering studies of methane beams on Ni(111). The quality of the fits seem to indicate that the efficacies of individual vibrations lay somewhere between the experimentally determined values and unity. This cursory study suggests that the efficacy of additional quanta does not seem to diminish, as that version of the model underestimated the sticking probability, especially at low translational energies. Further studies over a greater number of nozzle temperatures will be required to confirm this observation.

Future goals to further improve the model include obtaining a more complete data set for different nozzle temperatures. The model is able to predict two extremes – high and low temperature. The ability to model intermediate

nozzle temperature data will allow for better fine tuning of the relative contributions of each vibrational state. It would also be helpful in obtaining a more accurate estimate of the ground state sticking curve. While using low nozzle temperature data may seem sufficient, the varying nozzle temperature data allows for direct extrapolation of the reactivity of the ground state molecules. Under conditions where vibrationally excited molecules share the same asymptotic reactivity, Equation 3.1 can be simplified to

$$S_0^{(T)} = (1 - f_{exc})S_0^{v=0} + f_{exc}S_0^{v>0}. \quad \text{Equation 3.9}$$

With a set of sticking data at several different nozzle temperatures, vertical slices of the error functions can be taken at constant kinetic energy. Plotting the sticking probability at a given nozzle temperature,  $S_0^{(T)}$ , versus the fraction of molecules excited,  $f_{exc}$ , should give a straight line with a y-intercept of  $(1 - f_{exc})S_0^{v=0}$ , or simply  $S_0^{v=0}$ . The sticking can then be replotted as a function of kinetic energy, revealing a v=0 curve.

### 3.6 References

1. Kolasinski, K.W., *Surface Science : Foundations of Catalysis and Nanoscience*. 2nd ed. 2008, Chichester, England ; Hoboken, NJ: Wiley.
2. Somorjai, G.A., *Introduction to Surface Chemistry and Catalysis*. 1994, New York: Wiley.
3. Utz, A.L., *Mode selective chemistry at surfaces*. *Current Opinion in Solid State & Materials Science*, 2009. **13**(1-2): p. 4-12.
4. Juurlink, L.B.F., D.R. Killelea, and A.L. Utz, *State-resolved probes of methane dissociation dynamics*. *Progress in Surface Science*, 2009. **84**(3-4): p. 69-134.
5. Holmblad, P.M., J. Wambach, and I. Chorkendorff, *Molecular-Beam Study of Dissociative Sticking of Methane on Ni(100)*. *Journal of Chemical Physics*, 1995. **102**(20): p. 8255-8263.
6. Rettner, C.T., et al., *Chemical dynamics at the gas-surface interface*. *Journal of Physical Chemistry*, 1996. **100**(31): p. 13021-13033.
7. Juurlink, L.B.F., et al., *Eigenstate-resolved studies of gas-surface reactivity: CH<sub>4</sub> ( $\nu_3$ ) dissociation on Ni(100)*. *Physical Review Letters*, 1999. **83**(4): p. 868-871.
8. Juurlink, L.B.F., R.R. Smith, and A.L. Utz, *Controlling surface chemistry with light: Spatially resolved deposition of rovibrational-state-selected molecules*. *Journal of Physical Chemistry B*, 2000. **104**(14): p. 3327-3336.
9. Smith, R.R., et al., *Preference for vibrational over translational energy in a gas-surface reaction*. *Science*, 2004. **304**(5673): p. 992-995.
10. Bisson, R., et al., *State-resolved reactivity of CH<sub>4</sub> ( $2\nu_3$ ) on Pt(111) and Ni(111): Effects of barrier height and transition state location*. *Journal of Physical Chemistry A*, 2007. **111**(49): p. 12679-12683.

11. Bisson, R., et al., *Vibrational activation in direct and precursor-mediated chemisorption of SiH<sub>4</sub> on Si(100)*. Journal of Chemical Physics, 2008. **129**(8): p. 081103.
12. Killelea, D.R., et al., *Bond-selective control of a heterogeneously catalyzed reaction*. Science, 2008. **319**(5864): p. 790-793.
13. H.L. Abbot, A.B., I. Harrison, *Microcanonical unimolecular rate theory at surface. II. Vibrational state resolved dissociative chemisorption of methane on Ni(100)*. Journal of Chemical Physics, 2004. **121**(8): p. 3792-3810.
14. H.L. Abbot, I.H., *Dissociate Chemisorption and Energy Transfer for Methane on Ir(111)*. Journal of Physical Chemistry B, 2005. **109**: p. 10371-10380.
15. Ceyer, S.T., et al., *Effect of Translational and Vibrational-Energy on Adsorption - the Dynamics of Molecular and Dissociative Chemisorption*. Journal of Vacuum Science & Technology a-Vacuum Surfaces and Films, 1987. **5**(4): p. 501-507.
16. Juurlink, L.B.F., et al., *Eigenstate-Resolved Studies of Gas-Surface Reactivity: CH<sub>4</sub> (n<sub>3</sub>) Dissociation on Ni(100)*. Phys. Rev. Lett., 1999. **83**(4): p. 868-871.
17. Beck, R.D., et al., *Vibrational mode-specific reaction of methane on a nickel surface*. Science, 2003. **302**(5642): p. 98-100.
18. Michelsen, H.A. and D.J. Auerbach, *A Critical-Examination of Data on the Dissociative Adsorption and Associative Desorption of Hydrogen at Copper Surfaces*. Journal of Chemical Physics, 1991. **94**(11): p. 7502-7520.
19. Luntz, A.C., *A simple model for associative desorption and dissociative chemisorption*. J. Chem. Phys., 2000. **113**(16): p. 6901-6905.

20. Luntz, A.C. and J. Harris, *C-H Bond Activation On Metals - A Quantum Dynamics Model of Direct and Precursor-Mediated Dissociation*. J. Vac. Sci. Technol. A-Vac. Surf. Films, 1992. **10**(4): p. 2292-2298.
21. Michelsen, H.A., et al., *Effect of Rotation on the Translational and Vibrational-Energy Dependence of the Dissociative Adsorption of D<sub>2</sub> on Cu(111)*. Journal of Chemical Physics, 1993. **98**(10): p. 8294-8307.
22. Michelsen, H.A. and D.J. Auerbach, *Contributions of H<sub>2</sub> (V=0) and H<sub>2</sub> (V=1) to the Dissociative Adsorption of Hydrogen on Cu(110)*. Physical Review Letters, 1990. **65**(22): p. 2833-2833.
23. Michelsen, H.A., C.T. Rettner, and D.J. Auerbach, *State-Specific Dynamics of D<sub>2</sub> Desorption from Cu(111) - the Role of Molecular Rotational Motion in Activated Adsorption-Desorption Dynamics*. Physical Review Letters, 1992. **69**(18): p. 2678-2681.
24. Rettner, C.T., D.J. Auerbach, and H.A. Michelsen, *Dynamic Studies of the Interaction of D<sub>2</sub> with a Cu(111) Surface*. Journal of Vacuum Science & Technology a-Vacuum Surfaces and Films, 1992. **10**(4): p. 2282-2286.
25. Rettner, C.T., H.A. Michelsen, and D.J. Auerbach, *Dynamics of the Desorption of D<sub>2</sub> and H<sub>2</sub> from Cu(111)*. Journal of Vacuum Science & Technology a-Vacuum Surfaces and Films, 1993. **11**(4): p. 1901-1906.
26. Herzberg, G., *Molecular Spectra and Molecular Structure II. Infrared and Raman Spectra of Polyatomic Molecules*. 1945, New York: Van Nostrand Reinhold.
27. Auerbach, D.J., C.T. Rettner, and H.A. Michelsen, *Interaction Dynamics of Hydrogen at a Cu(111) Surface*. Surface Science, 1993. **283**(1-3): p. 1-8.

28. Repetski, J.J. and R.E. Mates, *Rotational Temperature in an Underexpanded Jet*. *Physics of Fluids*, 1971. **14**(12): p. 2605-2619.
29. Sharma, P.K., et al., *Freezing of Vibrational Degrees of Freedom in Free-Jet Flows with Application to Jets Containing CO<sub>2</sub>*. *Journal of Chemical Physics*, 1975. **62**(2): p. 341-349.
30. Schoofs, G.R., et al., *Dissociative Chemisorption of Methane on Pt(111)*. *Surface Science*, 1989. **215**(1-2): p. 1-28.
31. Bronnikov, D.K., et al., *A diode laser spectrometer for state-resolved experiments on the methane-surface system*. *Chemical Physics Letters*, 1996. **249**(5-6): p. 423-432.
32. Tarrago, G., et al., *Ground-State of Methane <sup>12</sup>CH<sub>4</sub> through Forbidden Lines of V3 Band*. *Journal of Molecular Spectroscopy*, 1975. **57**(2): p. 246-263.
33. Killelea, D.R., *Bond-Selective Control of a Gas-Surface Reaction*, in *Chemistry*. 2007, Tufts University: Medford, MA.
34. Henkelman, G. and H. Jonsson, *Theoretical calculations of dissociative adsorption of CH<sub>4</sub> on an Ir(111) surface*. *Physical Review Letters*, 2001. **86**(4): p. 664-667.

## Chapter 4 Vibrational Enhancement of Reactivity in Precursor-Mediated Surface Reactions – Methane on Ir(111)

### 4.1 Introduction

At high translational energies, methane dissociation on metal surfaces is generally dominated by a direct mechanism in which methane either dissociatively chemisorbs or scatters non-reactively during a single-collision gas-surface encounter. The majority of methane molecules in a steam-reforming reactor have little translational energy, but the vibrational energy content of some is significant relative to the barrier to dissociation. Figure 4.1 shows the fractional populations of vibrational states and the 1-D translational energy distribution for a methane gas at 1050 K. The mean translational energy of methane at this temperature is about 9 kJ/mol. Most reactions at transition metal surfaces have a normal incident energy dependence [1], so only the component of translational energy perpendicular to the surface activates reaction. The component of energy parallel to the surface does not affect the overall sticking probability. Under these conditions, the 1-D energy distribution is more relevant, giving a mean translational energy of about 3 kJ/mol. Few molecules have enough translational energy to react directly, especially on nickel, which has activation barriers for methane near 100 kJ/mol [2-6].

Another factor plays an important role in the direct mechanism. Calculated transition state geometries show a tight transition state with barrier heights rising sharply as the molecular orientation, impact site, and bond deformations differ from the minimum energy path [7-11]. Since the timescale for molecular

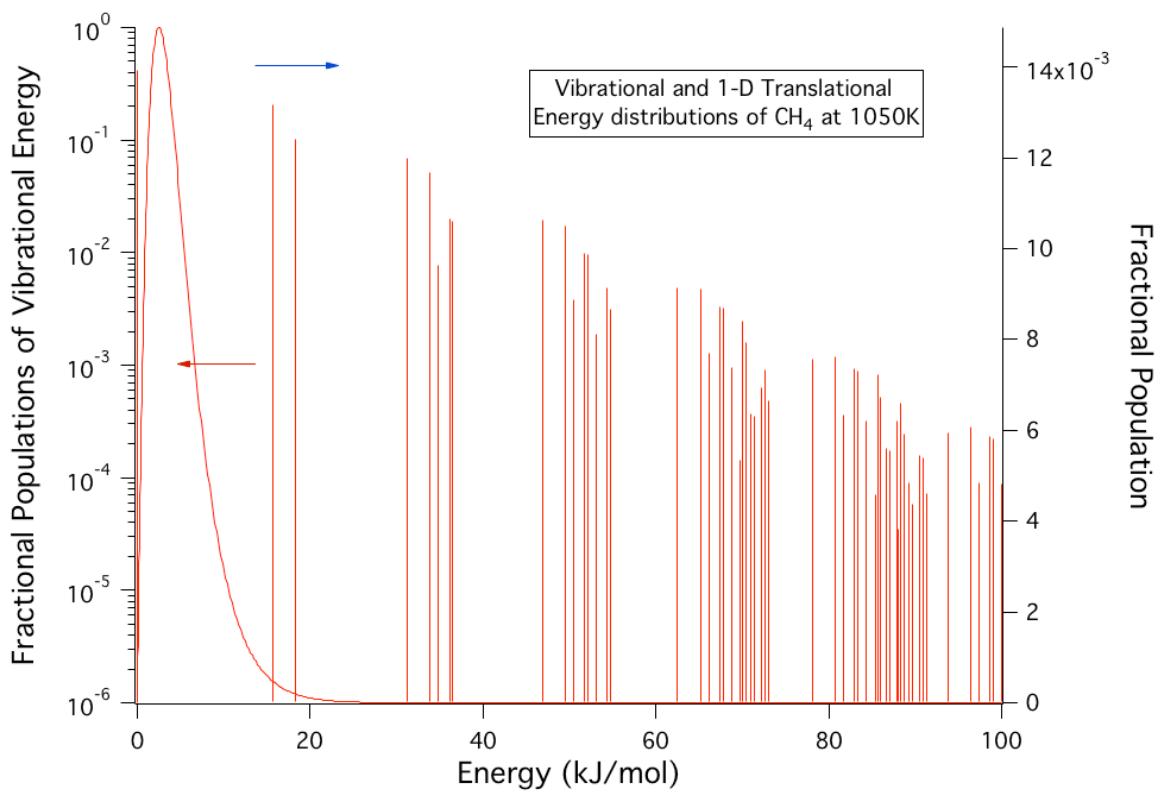


Figure 4.1 – Vibrational and 1-D translational energy distributions of methane at a gas temperature of 1050 K.

reorientation can be slow, many incident molecules may not be able to access low energy pathways to products during a single collision.

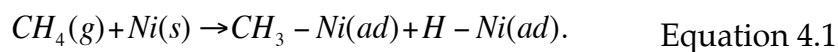
This chapter explores the possibility that a precursor mechanism involving vibrationally excited molecules trapped on the surface may be an important contributor to methane activation on metals at the high temperatures characteristic of industrial steam reforming reactors. Specifically, we will be looking at the enhancement in reactivity of thermally excited methane on an Ir(111) metal surface. Iridium was chosen due to existing experimental evidence of a precursor-mediated pathway [12], and due to its relatively low activation barrier, which is about 30-40 kJ/mol.

Vibrations have already been shown to enhance reactivity through the direct channel with state-dependent efficacies, evident through a shift in the methane sticking curve to lower energies upon excitation of specific vibrational modes [13]. Here we explore the reactivity of vibrationally excited molecules in a precursor-mediated mechanism, sometimes referred to as a trapping-mediated pathway. In order to show the effect of vibrations on the reactivity of trapped molecules, molecular beam reactivity data has been taken for two different nozzle temperatures: 300 K (room temperature) and 750 K. The 300 K molecular beams contain predominantly ground state molecules (>99%). About thirty-two percent of the 750 K beams are thermally excited into higher vibrational states that include fundamentals, overtones, and combination bands. Direct comparison of these two sticking curves reveals details about the relative efficacy of vibrations in the promotion of reactivity in the two mechanisms.

## 4.2 Reaction Mechanisms and Past Experiments

### 4.2.1 Direct vs. Trapping-Mediated Mechanisms

At high translational energy, methane surmounts the barrier to reaction and reacts via a direct mechanism on metals;



This mechanism is illustrated schematically in Figure 4.2a. In this case the incoming molecule contains enough internal energy to surmount the barrier on the first encounter and the methane dissociates. Molecules with energy below the barrier scatter off the surface non-reactively and return to the gas phase. The transition state of the reaction is generally governed by geometric factors. The lowest energy pathway to reaction requires the atoms of the molecule and the surface to approach in specific relative positions. The time scale of this reaction is short enough that only a small fraction of all possible geometries can be sampled. This means that the molecule gets one shot to get over the effective barrier determined by the positions of all of the atoms at the time of the first and only encounter. If the configuration of the methane and the surface atoms do not map onto the transition state geometry well, the effective barrier along the translational energy coordinate is higher, and the molecule scatters. If the molecule follows a more favorable pathway towards the barrier and transition state geometry, the molecule has a higher probability of reacting.

A second way that molecules can react is via a trapping-mediated pathway, shown in Figure 4.2b. In this reaction the methane does not initially have enough energy to react directly. Instead, its normal translational energy

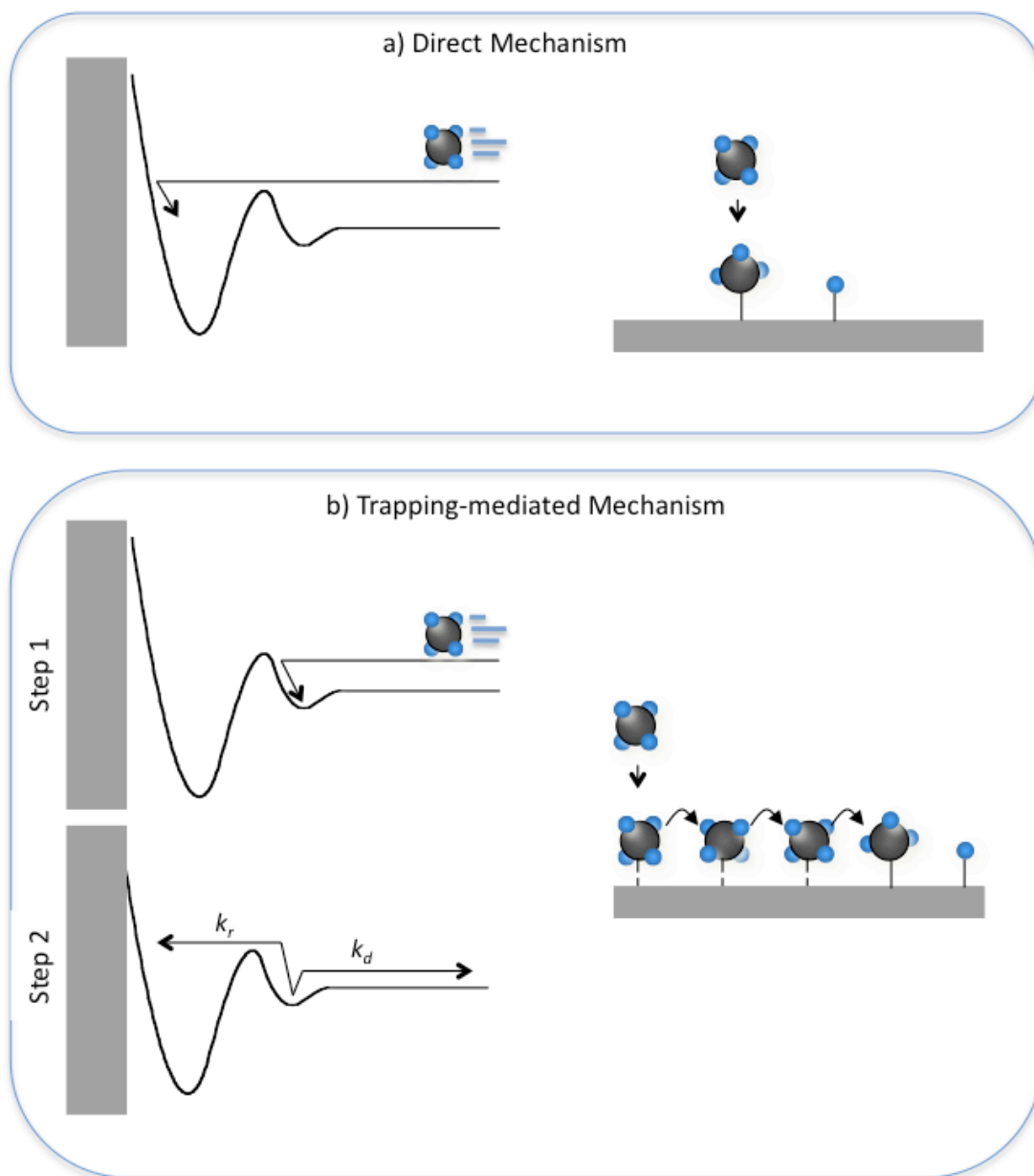
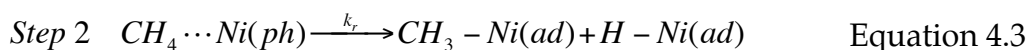
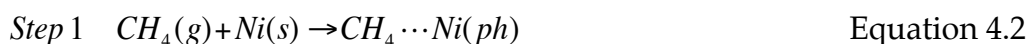
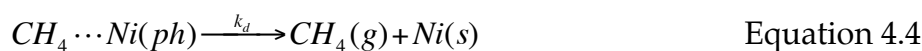


Figure 4.2 – Reaction pathways for a) direct mechanism and b) trapping-mediated mechanism.

accommodates with the surface and the methane becomes trapped in a physisorption well, staying intact as CH<sub>4</sub> bound to the surface in a Van der Waals-type interaction. The requirement for normal translational energy dissipation during a single collision means that the probability of trapping typically decreases with incident translational energy. The physisorption well is very shallow, usually only around 5 kJ/mol, and trapping is a non-activated process. From this physisorbed state, the methane can either react or desorb.



*or*



The overall probability of dissociative chemisorption will be proportional to the ratio of the rate constants of the two possible exit channels from the physisorption well,  $\frac{k_r}{k_r + k_d}$ . If the physisorption lifetime is sufficiently long, the physisorbed molecule and surface can exchange energy and approach full thermalization. When the methane is trapped on the surface, the barrier to reaction is typically high compared to the barrier to desorption, meaning the reacting fraction will typically be very small or vanishing. In the case of methane on nickel, the barrier to reaction is on the order of 100 kJ/mol [4], while the physisorption well depth is only about 5 kJ/mol [7].

Once the molecule is trapped, it is no longer bound to the same surface interaction time and orientation restrictions placed on the direct mechanism described previously. It has time to diffuse and tumble around the surface and sample geometries that provide more favorable barriers. It can do this because it

can now potentially find the ideal surface site and orientation to reaction. The surface temperature can have a large effect on the reaction probability, as a hotter surface can supply more energy to the molecule to help it get over the high activation barrier.

#### *4.2.2 Evidence for the Trapping-Mediated Reaction Pathway*

Most transition metal surfaces studied have not shown evidence of a trapping-mediated reaction pathway for methane [14]. This could be due to either a high activation barrier, resulting in sticking probabilities too low to measure, or low trapping probabilities. The first evidence of the precursor mechanism came about on the Pt(111){1x2} [15, 16] and the Ir(110) and (111) surfaces [12, 17, 18]. On the Ir(110) and Ir(111) surfaces, Seets, et al. showed that the reaction probability decreases with translational energy up until about 7 and 12 kJ/mol, respectively, and then begins increasing with energy. The initial decrease in reactivity with increasing translational energy is not consistent with a direct reaction mechanism since the molecules have very little internal energy relative to the activation barrier. Instead the authors claim that a precursor-mediated reaction pathway, where the methane would trap on the surface and then react is most consistent with the data. They showed that the reaction probability at low translational energies had the same functional form as the trapping probability at a given surface temperature. The trapping probability curve multiplied by a constant reaction probability for the physisorbed molecules yields the reactivity for the trapping-mediated channel. At higher translational energy, the direct channel starts to dominate and the reaction probability increases with translational energy.

On the Pt(110) reconstructed surface, Walker, et al. showed that up until about 10 kJ/mol normal incident energy, the reaction probability decreased with translational energy. It then increased with translational energy above 10 kJ/mol. The authors claimed that this decrease with energy was evidence of a non-activated direct process via a non-thermalized physisorbed molecule. This is essentially a trapped methane that has lost its translational energy to the surface, but has retained some vibrational energy. Experiments at elevated nozzle temperatures did, in fact, show an enhancement in the reactivity of these molecules, indicating that the vibrational energy was retained by the methane physisorbed on the surface.

#### *4.2.3 Relevant Lifetimes*

The ability of a vibrationally hot precursor to use its internal energy to react depends on the relative rates of reaction and vibrational quenching. We now consider whether the vibrational energy is quenched once the molecule physisorbs on the surface. It is necessary to take a look at relative lifetimes for the methane while it's trapped on the surface to see if the experiment is even feasible. Sitz and Mullins have calculated that the lifetime of trapped methane on the Ir(111) surface at 1000 K is on the order of 8-10 ps [19]. The physisorption lifetime increase to about 500 ps at 300 K. The lowest energy vibration for methane occurs at  $1311\text{ cm}^{-1}$ , which is the  $\nu_4$  stretching mode. This has a frequency of around  $4 \times 10^{13}\text{ s}^{-1}$ , and allows for about  $10^3$  vibrations in the physisorbed lifetime on a 1000 K surface. Higher energy vibrations will have shorter vibrational periods. Even at the highest surface temperatures there is

plenty of time to sample the full range of vibrational phases during a physisorption lifetime.

Vibrational lifetimes on metals are limited by electronic processes that form excited electron-hole pairs [20]. Beckerle, et al. measured the vibrational lifetime of CO chemisorbed on a Pt(111) surface to be about 1 ps [21]. Krishna and Tully used density functional theory to calculate the vibrational lifetime of CO on Ni(111), and found it to be about 2 ps [20]. CO lifetimes are likely a lower limit for electronically-mediated vibrational quenching due to the unusually strong metal-CO bond. Lifetimes of more weakly bound surface species range from a few to a few tens of picoseconds. All of these times are longer than a vibrational period and much longer than the duration of a direct gas-surface encounter.

### *4.3 Experimental Details*

Experiments used the new molecular beam-surface scattering chamber described in Chapter 2. An Ir(111) sample polished to within  $\sim 0.1^\circ$  of the (111) face was obtained from SPL. The sample was heated using a 500 V electron beam, and cooled using a dry ice cryostat. The temperature was measured using a type-R thermocouple spot-welded to the back of the crystal. Typical cleaning techniques were used [22]: Ar<sup>+</sup> sputtering and annealing, and oxidation. After each experiment, the sample was annealed in  $1 \times 10^{-7}$  torr of oxygen to remove carbon, and then briefly heated above 1500 K to remove any remaining oxygen. Surface cleanliness was verified via Auger measurements in the carbon and oxygen regions. The kinetic energies of the molecular beam were tuned by

varying the nozzle temperature and seeding the beam. The methane was seeded with helium for higher energy beams, and with argon and krypton for the lower energy (<10 kJ/mol) measurements. Beam energies were measured using time-of-flight techniques [23]. For these experiments the nozzle temperature was held at either 300 K or 750 K.

Both molecular beam reflectivity (King & Wells) [24] and Auger electron spectroscopy (AES) methods were used to measure the initial sticking probabilities of methane. King and Wells was generally used for beams above 60 kJ/mol, where the reaction probability is greater than 3-5%. For smaller reaction probabilities, the AES method was used. The ratio of the C/Ir peaks at 272 and 229 eV, respectively, were converted to coverages and calibrated with a King & Wells measurement on a dose in which the C/Ir ratio was measured. The incident flux of methane and the dose duration define the number of molecules that strike the surface, and AES measures the carbon coverage on the surface after the dose. Typically, the doses were run long enough to obtain a C/Ir ratio of about 0.20, which corresponds to a coverage of about 0.1 ML. In order to rule out carbon contamination of the crystal from background gases, the beam was run into a beam flag in front of the crystal, blocking it from directly impinging on the Ir sample for over 5 hours. An auger scan taken after this exposure indicated an atomically clean surface.

#### ***4.4 Results and Discussion***

The reaction probability of methane on Ir(111) from 3-80 kJ/mol appears in Figure 4.3. As translational energy increases, the sticking probability initially

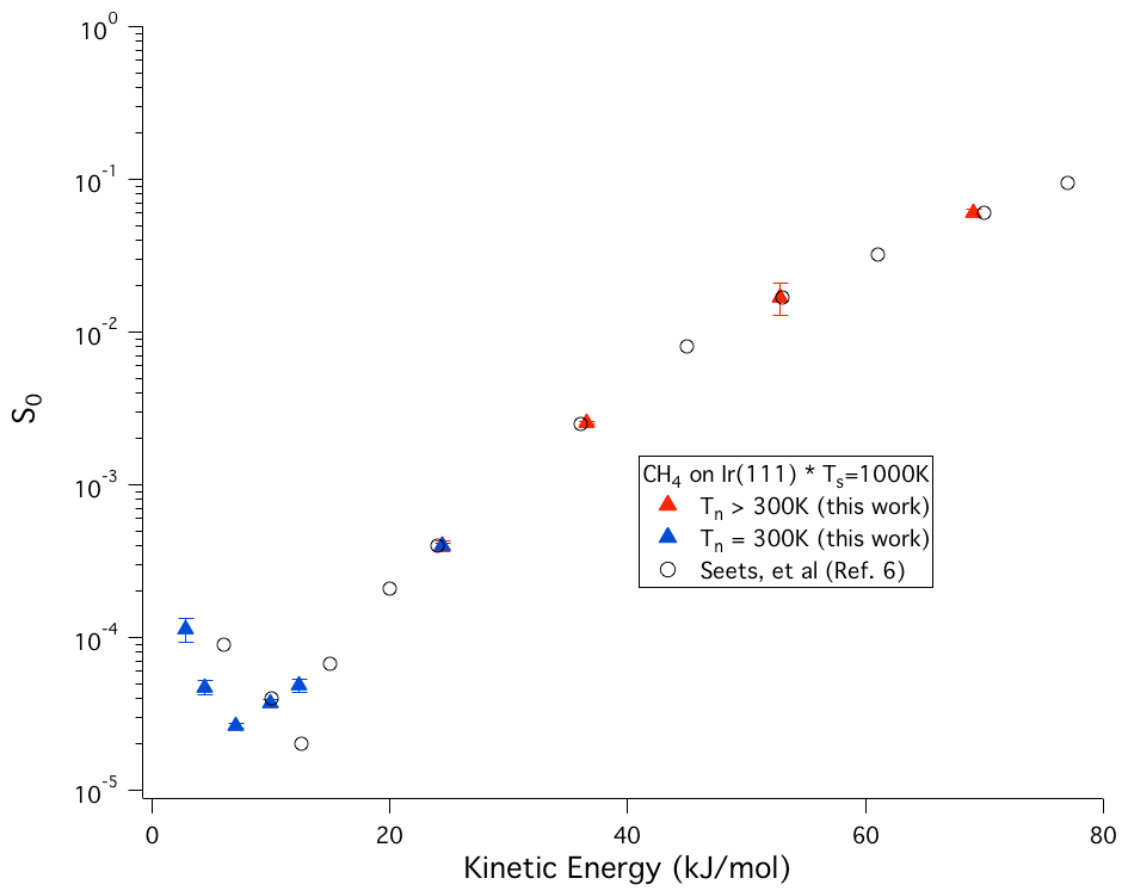


Figure 4.3 – Reaction probability of methane on Ir(111). Data in open circles taken from reference 6. T<sub>s</sub>=1000 K.

decreases. At about 7 kJ/mol, the sticking probability reaches a minimum and begins to increase again. The data from Seets, et al, are shown in the open circles for comparison [12]. At translational energies above 20 kJ/mol the data agree very well. However, the minimum in the sticking probability of our data occurs 5 kJ/mol lower in energy than Seets observed. The cause of this has yet to be determined. One factor that may affect the location of the minimum is that the data presented here were obtained using a crystal with a smaller miscut, potentially leading to lower step density. The step sites may enhance reactivity preferentially in the precursor-mediated channel, causing the shift of the minimum to higher energy. Nonetheless, our data clearly show both the precursor-mediated and direct reaction pathways in agreement with Seets, et al.

The next step is to raise the temperature of the methane to 750 K, and explore how vibrationally hot molecules affect reactivity below 30 kJ/mol of translational energy. Raising the nozzle temperature to 750 K excites about 32% of the methane gas into vibrationally excited states. A comparison of the hot nozzle and room temperature results appear in Figure 4.4. The initial reaction probability for vibrationally hot methane increases in both the direct and precursor-mediated reaction channels. At higher translational energy, the enhancement in the direct channel appears to diminish. At these higher energies, the translational energy is comparable to the activation energy, so the vibrations become less important. As translational energy decreases along the direct channel, the enhancement becomes more prominent.

The data in Figure 4.4 suggest that the precursor-mediated pathway is enhanced more than the direct, causing the translational energy at the reaction probability minimum to shift to a higher energy, about 10 kJ/mol for the higher

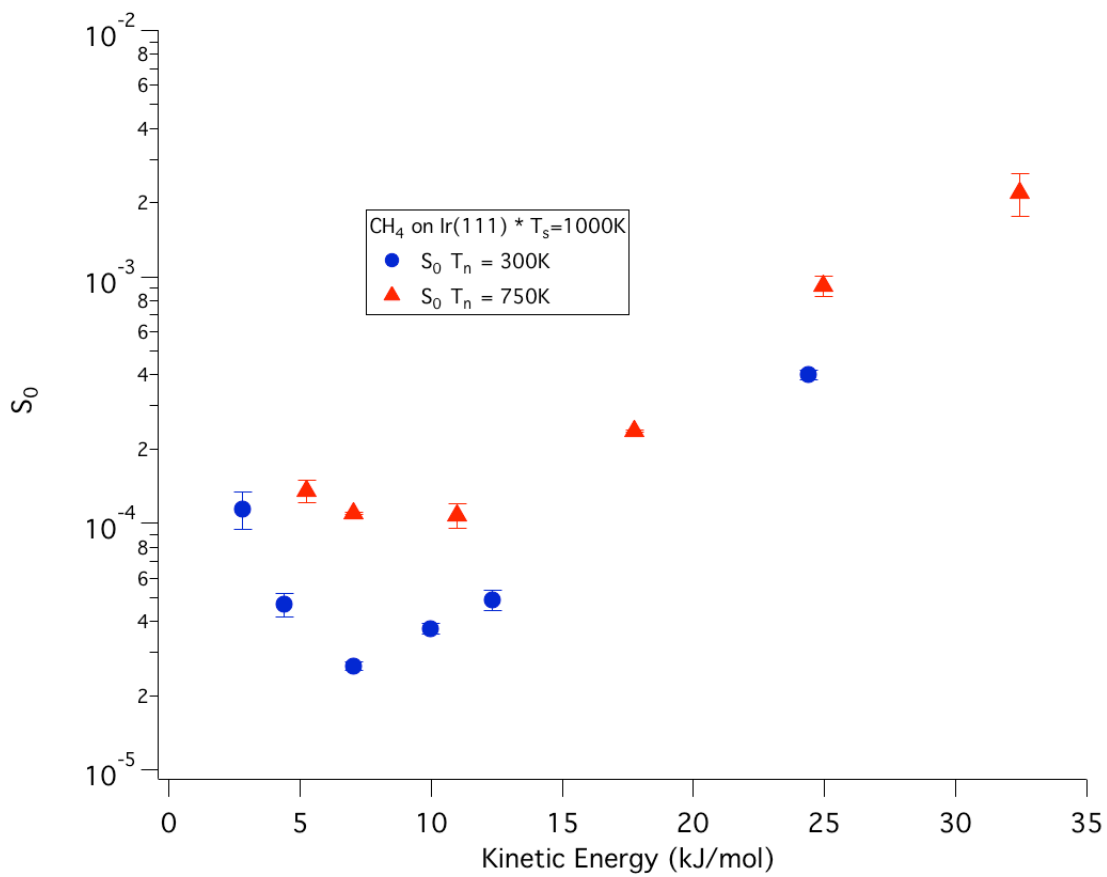


Figure 4.4 – Reaction probabilities for room temperature and 750K nozzle experiments. T<sub>s</sub>=1000 K.

nozzle temperature data. This indicates that vibrational excitation does enhance the reactivity of physisorbed methane molecules, possibly even more than observed in the direct channel. More importantly, it indicates that the vibrations are not necessarily immediately thermalized with the surface upon physisorption. If that were the case, there should be no difference in the trapping-mediated channel for the vibrationally hot and cold methane. This would present as having the same sticking probability regardless of gas temperature.

If the methane vibration is quenched by the surface phonon modes, it could create a local hot spot where the surface has gained excess energy in the atoms near the physisorption site. If this translates into a larger deviation of the atoms from the surface, they could more easily approach the transition state geometry and possibly present a lower energy pathway to reaction, enhancing the reactivity. However, it's been shown that electron-hole pair excitation dominates vibrational quenching on metals [20, 25, 26]. Due to the relatively large amount of energy of the vibration compared to phonons, the transfer of energy isn't very efficient since many quanta of surface vibrations would have to be excited at once. Either way, the presence of the vibrational energy is causing an enhancement in reactivity through this trapping channel.

#### ***4.5 Conclusions and Future Goals***

The results show that vibrational energy within the reactant methane gas enhances reactivity in both the direct and trapping-mediated reaction channels. The vibrational energy is clearly not immediately transferred to the surface upon

physisorption of the gas. More importantly, it appears, albeit from a limited data set, that the vibrations have a larger effect on the reactivity within the precursor mediated pathway. This is likely due to the ability of the methane to access more possible pathways to reaction, as well as access a lower energy transition state not otherwise available.

Future experiments will include eigenstate-resolved measurements of the sticking of methane on both Ir(111) and Ir(110), as well as on Pt(111). Use of laser excitation will prepare much greater numbers of CH<sub>4</sub> molecules with chemically significant amounts of vibrational energy. The relative efficacies of different modes of vibration can be measured in both reaction pathways. It would also be interesting to see if there is any effect on the reactivity that depends on specific rotational states within the vibrational manifold.

One possible complication with laser-prepared states is that they may enhance the direct channel so much that they obscure precursor channels. This may be the case for recent studies on Pt(100){2x1} [27]. As discussed in Chapter 3, addition of vibrational energy shifts the sticking probability curve by the product of the vibrational energy and its efficacy. For the case of  $\nu_3$ , if it has an efficacy of around unity on iridium, the shift of the direct curve will completely drown out the trapping-mediated channel. It seems it would be more interesting to see the effects of the lower energy bends rather than higher energy stretches.

## 4.6 References

1. Kolasinski, K.W., *Surface Science : Foundations of Catalysis and Nanoscience*. 2nd ed. 2008, Chichester, England ; Hoboken, NJ: Wiley.
2. Ceyer, S.T., et al., *Effect of Translational and Vibrational-Energy on Adsorption - the Dynamics of Molecular and Dissociative Chemisorption*. *Journal of Vacuum Science & Technology a-Vacuum Surfaces and Films*, 1987. **5**(4): p. 501-507.
3. Chorkendorff, I. and J.W. Niemantsverdriet, *Concepts of modern catalysis and kinetics*. 2nd ed. 2007, Weinheim: Wiley-VCH.
4. Holmblad, P.M., J. Wambach, and I. Chorkendorff, *Molecular-Beam Study of Dissociative Sticking of Methane on Ni(100)*. *Journal of Chemical Physics*, 1995. **102**(20): p. 8255-8263.
5. Nielsen, B.O., et al., *Activated Dissociative Chemisorption of Methane on Ni(100) - A Direct Mechanism under Thermal Conditions*. *Catalysis Letters*, 1995. **32**(1-2): p. 15-30.
6. Lee, M.B., Q.Y. Yang, and S.T. Ceyer, *Dynamics of the Activated Dissociative Chemisorption of CH<sub>4</sub> and Implication for the Pressure Gap in Catalysis - A Molecular-Beam High-Resolution Electron-Energy Loss Study*. *Journal of Chemical Physics*, 1987. **87**(5): p. 2724-2741.
7. Henkelman, G., A. Arnaldsson, and H. Jonsson, *Theoretical calculations of CH<sub>4</sub> and H<sub>2</sub> associative desorption from Ni(111): Could subsurface hydrogen play an important role?* *Journal of Chemical Physics*, 2006. **124**(4): p. 044706.

8. Henkelman, G. and H. Jonsson, *Theoretical calculations of dissociative adsorption of CH<sub>4</sub> on an Ir(111) surface*. Physical Review Letters, 2001. **86**(4): p. 664-667.
9. Nave, S. and B. Jackson, *Methane dissociation on Ni(111): The effects of lattice motion and relaxation on reactivity*. Journal of Chemical Physics, 2007. **127**(22): p. 173003.
10. Nave, S. and B. Jackson, *Methane dissociation on Ni(111) and Pt(111): Energetic and dynamical studies*. Journal of Chemical Physics, 2009. **130**(5): p. 054701.
11. Nave, S., A.K. Tiwari, and B. Jackson, *Methane dissociation and adsorption on Ni(111), Pt(111), Ni(100), Pt(100), and Pt(110)-(1x2): Energetic study*. Journal of Chemical Physics, 2010. **132**(5): p. 134702.
12. Seets, D.C., et al., *Dissociative chemisorption of methane on Ir(111): Evidence for direct and trapping-mediated mechanisms*. J. Chem. Phys., 1997. **107**(23): p. 10229-10241.
13. Utz, A.L., *Mode selective chemistry at surfaces*. Current Opinion in Solid State & Materials Science, 2009. **13**(1-2): p. 4-12.
14. Rettner, C.T., et al., *Chemical dynamics at the gas-surface interface*. Journal of Physical Chemistry, 1996. **100**(31): p. 13021-13033.
15. Walker, A.V. and D.A. King, *Dynamics of the dissociative adsorption of methane on Pt{110}(1 x 2)*. Physical Review Letters, 1999. **82**(25): p. 5156-5159.
16. Walker, A.V. and D.A. King, *Dynamics of dissociative methane adsorption on metals: CH<sub>4</sub> on Pt{110}(1x2)*. Journal of Chemical Physics, 2000. **112**(10): p. 4739-4748.

17. Seets, D.C., M.C. Wheeler, and C.B. Mullins, *Mechanism of the dissociative chemisorption of methane over Ir(110): Trapping-mediated or direct?* Chem. Phys. Lett., 1997. **266**(5-6): p. 431-436.
18. Seets, D.C., M.C. Wheeler, and C.B. Mullins, *Trapping-mediated and direct dissociative chemisorption of methane on Ir(110): A comparison of molecular beam and bulb experiments.* J. Chem. Phys., 1997. **107**(10): p. 3986-3998.
19. Sitz, G.O. and C.B. Mullins, *Molecular dynamics simulations of the influence of surface temperature on the trapping of methane on iridium single-crystalline surfaces.* Journal of Physical Chemistry B, 2002. **106**(33): p. 8349-8353.
20. Krishna, V. and J.C. Tully, *Vibrational lifetimes of molecular adsorbates on metal surfaces.* Journal of Chemical Physics, 2006. **125**(5): p. 054706.
21. Beckerle, J.D., et al., *Ultrafast Infrared Response of Adsorbates on Metal-Surfaces - Vibrational Lifetime of CO/Pt(111).* Physical Review Letters, 1990. **64**(17): p. 2090-2093.
22. Musket, R.G., W. McLeana, C.A. Colmenaresa, D.M. Makowiecki, W.J. Siekhaus, *Preparation of Atomically Clean Surfaces of Selected Elements - A Review.* Applied Surface Science, 1982. **10**(2): p. 143-207.
23. Scoles, G., *Atomic and molecular beam methods: Volume 1.* 1988, New York: Oxford University Press.
24. King, D.A. and M.G. Wells, *Molecular-Beam Investigation of Adsorption Kinetics on Bulk Metal Targets - Nitrogen on Tungsten.* Surface Science, 1972. **29**(2): p. 454-482.
25. Persson, B.N.J., *Vibrational-Energy and Phase Relaxation at Surfaces.* Journal of Physics C-Solid State Physics, 1984. **17**(26): p. 4741-4750.

26. Tully, J.C., *Dynamics At Surfaces*. J. Electron Spectrosc. Relat. Phenom., 1990. **54**: p. 1-4.
27. Bisson, R., et al., *State-resolved reactivity of CH<sub>4</sub> (2ν<sub>3</sub>) on Pt(111) and Ni(111): Effects of barrier height and transition state location*. Journal of Physical Chemistry A, 2007. **111**(49): p. 12679-12683.